Dissertation

Interaction of slow electrons with matter for nanoscale characterisation of solids

Ausgeführt am

**Institut für Angewandte Physik
der Technischen Universität Wien**

unter der Anleitung von

Ao. Univ. Prof. Dr. techn. Wolfgang S. M. Werner

durch

Olga Ridzel

Skolkovskaya Straße 3B-208, 143005 Odinzowo,
Region Moskau, Russland

————————————— —————————————
Datum   Unterschrift

Abstract

Electron spectroscopy techniques based on the interaction of electrons with matter are one of the most popular tools for surface analysis. Methods of electron spectroscopy imply the irradiation of a solid surface with e.g. an electron beam with the subsequent detection of the outgoing electron signal acquired in the form of the energy and angular distribution of emitted electrons or the energy spectrum. The interpretation of such electron spectra requires the knowledge on the interaction processes of electrons with matter.

This thesis is dedicated to the investigation of electron transport in solids by means of two different approaches: the invariant imbedding method and the Monte Carlo simulation. The former approach is employed in problems of the interpretation and analysis of energy spectra of complicated multi-component materials such as graphene oxide. The possibility of the detection of light elements, including hydrogen and its isotopes, in different targets by means of elastic peak electron spectroscopy (EPES) is demonstrated.

The latter approach is employed for the investigation of the secondary electron emission phenomenon. Unfortunately, electron emission is still far from being quantitatively understood which is partly due to the experimental difficulty associated with the investigation of very low energy electrons. From the theoretical point of view, secondary electron emission modeling at a few eV is complicated by the absence of reliable data on the electron-solid interaction at such low energies such as the inelastic mean free path (IMFP). It turns out that secondary electron yield (SEY) values at any incident energy depend sensitively on the IMFP values, in particular below 100 eV, which makes it possible to get a realistic estimate for the IMFP values at low energies by comparing calculated SEY values with experimental data during variation of the IMFPs. In this work, a Monte Carlo model has been developed to describe the process of secondary electron emission from solids and calculate the SEY. The determination of IMFPs at low energies (below 100 eV) from analysis of SEYs at high energies was successfully performed for several metals and the results indicate that the IMFP values based on the Mermin dielectric function are more realistic. All the knowledge gained from this study points to the possibility of building a reliable theoretical model on the phenomenon of secondary electron emission. Experimental investigation of the IMFP at low energies by means of EPES was also carried out and results on the IMFP determination for a polycrystalline gold are presented.

Аннотация

Электронная спектроскопия, основанная на взаимодействии частиц и излучений с поверхностью твёрдого тела, является одним из самых популярных методов для анализа поверхности. Данная методика подразумевает облучение поверхности исследуемого образца, например, электронным пучком с последущим детектированием выходящего с поверхности сигнала, фиксируемого в виде энергетического и углового распределения вылетающих электронов или электронного спектра. Интерпретция таких электронных спектров требует наличия знаний о законах взаимодействия электронов с веществом.

Эта диссертация посвящена исследованию процессов переноса электронов в твёрдом теле с использоанием двух подходов: метода инвариантого погружения и статистического моделирования Монте Карло. Первый подход был использован в задачах интерпретации электронных спектров от сложных многокомпонентных мишеней на примере анализа оксида графена. Также в данной работе продемонстрирована возможность детектирования водорода и его изотопов в различных мишенях используя спектроскопию пиков упруго отражённых электронов (СПУЭ).

Второй подход использовался для исследования явления вторичной электронной эмиссии твёрдых тел. К сожалению, вторичная электронная эмиссия всё ещё далека от количественного понимания, что отчасти связано с экспериментальными сложностями проведения каких-либо исследований, задействующих электроны с очень низкой энергией. С теоретической точки зрения, моделирование вторичной электронной эмиссии при нескольких эВ усложняется отсутствием надёжных данных о характеристиках взаимодействия электронов с твёрдым телом при таких низких энергиях. Одной из важнейших характеристик в данном случае является длина свободного пробега между двумя последовательными неупругими соударениями налеющего электрона с электронами мишени. В данной работе показано, что коэффициент вторичной электронной эмиссии, измеренный при любых энергиях падающего электронного пучка, зависит в основном именно от этой величины на низких энергиях. Другими словами, число эмитируемых вторичных электронов наибольшим образом зависит от длины неупругого пробега электронов с низкой энергией, независимо от энергии падающего пучка. Таким образом, данный факт позволяет получить реалистичную оценку значений длины неупругого пробега электронов с низкой энергией путём сравнения экспериментально измеренных значений коэффициента вторичной электронной эмиссии с результатами расчёта этой величины, полученных при подстановке теоретических значений неупругой длины, варьируемых между двумя границами, найденными в литературе. Для этого была разработана модель Монте Карло, позволяющая описать процесс вторичной электронной эмиссии и рассчитать значения коэффициента вторичной электронной эмиссии. Определение неупругой длины электронов с низкой энергией (ниже 100 эВ) из анализа этого коэффициента, измеренного при высоких начальных энергиях, было успешно выполнено для нескольких металлов. Результаты данного исследования показали, что величины неупругого

пробега, рассчитанные на основе диэлектрической функции Мёрмина, являются наиболее реалистичными. Все знания, полученные в этом исследовании, указывают на возможность построения надёжной теоретической модели для описания и понимания явления вторичной электронной эмиссии. Также была проведена попытка экспериментального определения неупруго пробега электронов с низкой энергией с помощью метода СПУЭ. Данное исследование не показало значимых результатов, подтверждая сказанное выше об экспериментальных трудностях измерения каких-либо величин при низких электронных энергиях.

Kurzfassung

Eine der beliebtesten Methoden zur Oberflächenanalyse ist die Elektronenspektroskopie, welche auf der Wechselwirkung von Teilchen und Strahlung mit der Oberfläche eines Festkörpers beruht. Diese Technik basiert auf der Bestrahlung einer zu untersuchenden Probe, z. B. mit Hilfe eines Elektronenstrahls, und der anschließenden Detektion eines von der Oberfläche ausgehenden Signals. Welches in Form einer Energieverteilung der austretenden Elektronen oder des elektronischen Spektrums aufgezeichnet wird. Die Interpretation solcher elektronischer Spektren erfordert die Kenntnis der Wechselwirkungsgesetze von Elektronen mit Materie.

Diese Dissertation widmet sich der Untersuchung des Elektronentransports in einem Festkörper unter Verwendung zweier Ansätzen: der invarianten Immersionsmethode und der statistischen Monte Carlo Simulation. Der erste Ansatz wurde bei der Interpretation Elektronenspektren von komplexen Mehrkomponententargets am Beispiel der Graphenoxidanalyse verwendet. Weiters wurde in dieser Arbeit die Möglichkeit des Nachweises leichter Elemente, wie Wasserstoff und seiner Isotope, in verschiedenen Targets anhand der elastischen Peak Elektronen Spektroskopie demonstriert.

Der zweite Ansatz wurde verwendet, um das Phänomen der Sekundärelektronenemission von Festkörpern zu untersuchen. Bedauerlicherweise ist die Sekundärelektronenemission immer noch weit von einem quantitativen Verständnis entfernt, was teilweise auf die experimentellen Schwierigkeiten bei der Durchführung von Untersuchungen mit Elektronen mit sehr geringen Energien zurückzuführen ist. Aus theoretischer Sicht wird die Modellierung der Sekundärelektronenemission bei mehreren eV durch das Fehlen zuverlässiger Daten über die Eigenschaften der Wechselwirkung von Elektronen mit einem Festkörper bei derart niedrigen Energien erschwert. Im Bereich solch niedriger Energien ist eine der wichtigsten Eigenschaften die unelastische mittlere freie Weglänge von Elektronen, welche die Distanz zwischen zwei aufeinanderfolgenden unelastischen Kollisionen angibt. Diese Arbeit zeigt, dass der Sekundärelektronenemissionskoeffizient bei beliebigen Energie des einfallenden Elektronenstrahls hauptsächlich von der unelastischen mittleren freien Weglänge bei niedrigen Energien abhängt. Mit anderen Worten, die Anzahl der emittierten Sekundärelektronen hängt am stärksten von der Länge des unelastischen Weges der niederenergetischen Elektronen ab, unabhängig von der Energie des einfallenden Strahls. Diese Tatsache ermöglicht es eine realistische Schätzung des unelastischen mittleren freien Weges für niederenergetische Elektronen zu erhalten. Hierfür werden experimentell gemessenen Werte des Sekundärelektronenemissionskoeffizienten mit berechneten Werten dieser Größe verglichen. Diese berechneten Sekundärelektronenemissionskoeffizienten werden durch Ersetzen der theoretischen unelastischen Längenwerte zwischen den beiden in der Literatur gefundenen Grenzen erhalten. Für diesen Zweck wurde ein Monte Carlo Modell entwickelt, welches den Prozess der Sekundärelektronenemission beschriebt und die Werte des Sekundärelektronenemissionskoeffizienten berechnet. Die Bestimmung der unelastischen Länge von niederenergetischen Elektronen (unter 100 eV) aus einer Analyse dieses Koeffizienten, gemessen bei hohen Anfangsenergien, wurde für mehrere Metalle

erfolgreich durchgeführt und wies gute Übereinstimmung mit Werten auf Grunde dielektrischen Function nach Mermin auf. Alle in dieser Studie gewonnenen Erkenntnisse weisen auf die Möglichkeit hin, ein zuverlässiges theoretisches Modell zur Beschreibung und zum Verständnis des Phänomens der Sekundärelektronenemission zu erstellen. Zusätzlich wurde versucht die inelastische freie Weglänge der niederenergetischen Elektronen unter Verwendung der elastischen Peak Elektronen Spektroskopie experimentell zu bestimmen. Diese Studie zeigte keine signifikanten Ergebnisse und bestätigte die obigen Ausführungen zu den experimentellen Schwierigkeiten bei Messungen niederenergetischer Elektronen.

Acknowledgements

Contents

Chapter 1

Introduction and Motivation

The electron was discovered more than a century ago. However there are still fundamental, yet unresolved questions concerning the interaction of electrons (in particular low energy electrons) with a solid surface. Nowadays, many scientific and technological fields employ electron beam techniques to analyze and modify surfaces. For example, electron spectroscopy techniques such as the Electron Energy Loss Spectroscopy (EELS) and the X-ray Photoelectron Spectroscopy (XPS) are based on the interaction of electron and photon beams with matter for surface analysis [1]. The use of electrons makes these techniques highly surface sensitive due to the fact that the information depth in such an analysis employing medium energy electrons as probing particles is about several nanometers. This value is determined by the so-called Inelastic Mean Free Path (IMFP) defined as the average distance between two successive inelastic collisions measured along the electron trajectory. It is governed by the intense interaction of a probing electron with the solid state electrons.

While for surface analysis usually medium energy (200 - 5000 eV) electrons are used, one particular area of current interest in science concerns electrons with low kinetic energies (below 50 eV). Generation of Low Energy Electrons (LEE) occurs upon the inelastic interaction of charged particles with a solid medium. In an inelastic collision a part of the energy of an impinging electron is transferred to a solid state electron or to the ensemble of solid state electrons. As a consequence of such a collision, a Secondary Electron (SE) can be generated. The motivation of studying the interaction of low energy electrons $(0 - 100$ eV$)$ with matter comes from many scientific and technological applications. One of them is accelerator physics. Here low energy SEs critically affect the operation of

particle accelerators, since they can lead to electron cloud formation through multipacking [2, 3], e.g. in the Large Hadron Collider at CERN. An incoming proton ionizes the residual gas in the beam pipe, and as a result electrons are generated. However, it also produces synchrotron radiation, and generated photons in turn also create photoelectrons. These electrons collide with the vacuum chamber walls, resulting in emission of SEs which are boosted by the proton beam coming by in the next bunch. In this way, SEs are multiplied leading to electron stimulated desorption and thermal load. The mitigation of the electron cloud becomes particularly important when the high-luminosity mode will be taken into operation [4, 5, 6]. Another phenomenon where Secondary Electron Emission (SEE) plays a crucial role is mitigation of charging of spacecrafts [7]. Detailed understanding of the mechanisms of the emission of secondary electrons is also essential when investigating the plasma-wall interaction in a fusion reactor [8]. Here the cloud of low energy electrons emitted from the internal surface of the reactor, where the plasma is maintained, influences its stability to an important degree.

SEs also play a crucial role in the visualization of nanostructured materials in the Secondary Electron Microscope (SEM) [9, 10, 11]. In scientific apparatus, employing electron spectroscopies, SEE is undesirable in electron optics, whereas at the same time it is exploited in the same instrument for amplifying the electron signal coming from the sample for its detection [12]. There is also an important class of applications where the creation of secondary electrons in the form of hot electrons (below the vacuum level) causes either desired or undesired effects [3]. These applications include nanopatterning of surfaces employing electron beam lithography [13] and deals with the proximity effect of diffusing hot electrons thus limiting the attainable lateral resolution. In the case of biological tissue, LEEs cause damage in the form of bond breaking of DNA which may lead to tumor formation, but at the same time the application of low energy electrons for therapeutic purposes is also being investigated [14]. Finally, hot electrons are employed in microelectronics and photovoltaics, underpinning the importance to learn about fundamentals of their generation mechanism.

For all scientific cases and technological applications mentioned above, it is desirable to control SEE to some extent which represents a highly demanding scientific goal.
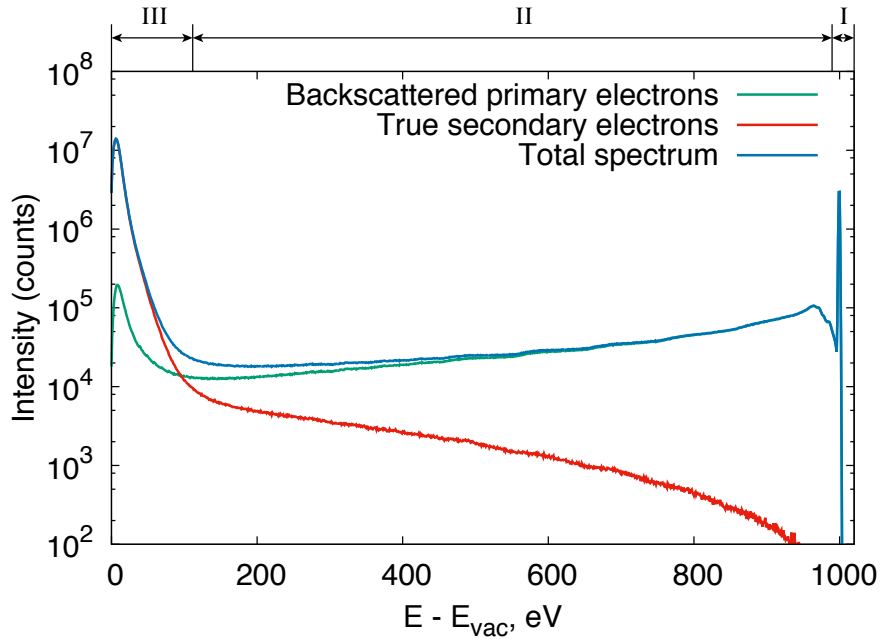
Figure 1.1: Monte Carlo simulation of secondary electrons emitted from a Au target, for a primary electron energy of $E_0 = 1000$ eV for normal electron incidence and emission into the entire hemisphere above the sample. The total energy distribution (blue curve) is made up of backscattered primary electrons (green curve) and secondary electrons (red curve).

1.1 Basic knowledge about the electron-induced energy spectrum

Generally, the bombardment of a solid surface by charged particles yields the backscattering of the probing particles (primaries) and the emission of secondary electrons. As a result, a characteristic energy distribution of emitted electrons is acquired known as electron spectrum. Fig. 1.1 shows results of a Monte Carlo (MC) calculation of a typical energy distribution of electrons emitted from a gold surface. The electrons detected in such a spectrum can be subdivided into three groups namely: (1) elastically reflected primary electrons; (2) inelastically backscattered primary electrons; (3) emitted secondary electrons [15].

1. Elastically reflected primary electrons are those which escape from the solid without suffering energy loss processes. As a consequence, they make up a peak in the spectrum at the energy of the primaries referred to as the elastic or zero-loss peak and marked as "I" in Fig. 1.1. Elastic scattering occurs by means of the interaction

13

between the electron and a nucleus involving a deflection of the electron wave by the (screened) Coulomb field of the nucleus. Such a collision is accompanied by a large momentum transfer and by a small recoil energy loss. Due to the large mass difference between electron and nucleus, this energy loss is usually negligible compared to any energy loss experienced in inelastic collisions. Therefore the electron gets deflected but its energy is considered to remain unchanged.

2. Inelastically backscattered primary electrons are those which escape from the solid after having transferred part of their energy and momentum to a solid state electron or to the ensemble of solid state electrons. After suffering single or multiple energy losses during the inelastic scattering electrons contribute to the lower kinetic energy side next to the elastic peak in the spectrum known as the inelastic background (marked as "II" in Fig. 1.1). Since both probing electrons and solid state electrons have the same mass the energy transferred to the electronic subsystem of the solid is accompanied by a small momentum transfer. Therefore deflections during inelastic scattering can be neglected implying rectilinear motion for impinging electrons.

3. True secondary electrons are defined as those emitted from the solid as a consequence of the inelastic interaction between the probing electrons and the solid state electrons. Some of these SEs can escape over the surface potential barrier after the generation if their kinetic energy is sufficient to overcome the surface potential barrier. However, after being created the SE can also undergo additional scatterings (elastic and inelastic) along its path towards the surface. Therefore this SE can in turn produce other SEs as a result of multiple inelastic collisions. Such a cascade process yields an essentially featureless peak of a high intensity positioned at low energies in the spectrum and referred to as the secondary electron peak (marked as "III" in Fig. 1.1). As can be seen in the red curve in Fig. 1.1 a certain fraction of SEs escapes from the solid with energies comparable with the primary energy, although the majority is released with energies below ~ 50 eV. On the other hand, the green curve in Fig. 1.1 shows that the contribution of backscattered primaries to the total spectrum is more than an order of magnitude smaller than the contribution of secondaries, which is the reason why, by convention, electrons with energies below ~ 50 eV are designated as secondary electrons.

The energy distribution of all these electrons is characteristic for a certain investigated material since it is related to its electronic structure and chemical composition. For example, measurement of the intensity of the elastic peak in the energy spectra allows the

experimental determination of the value of the IMFP for the investigated target [16, 17, 18]. The IMFP is the quantity of paramount importance in all electron spectroscopy techniques since it determines the surface sensitivity. For medium energy electrons (200 - 5000 eV) this value is of the order of several nanometers which makes it very difficult to measure. One of the commonly accepted approaches for doing that for homogeneous materials is Elastic Peak Electron Spectroscopy (EPES) consisting in measurements of the intensity of the elastic peak in absolute units [19]. The corresponding value of the IMFP is then obtained after fitting the calculated intensity to the measured intensity. The proportionality between the IMFP and the elastic peak intensity can be explained as follows: the larger average distance between inelastic collisions, the more electrons are elastically scattered because the probability that an inelastic process occurs on the way into the target and out of the target is reduced. Therefore the elastic reflection coefficient depends sensitively on the IMFP. The question remains as to whether the EPES technique for the determination of the IMFP can be employed for electron beams of low incident energies (below 100 eV).

The second application of EPES when measuring elastic peaks with a high energy resolution (of the order of 0.01 eV) is quantitative identification of elements in the sample. This is attributable to the fact that during an elastic event not only momentum is transferred but depending on the energy of the impinging electron and the scattering geometry there is also a measurable recoil energy loss. For higher incident energies and lower atomic number Z, this value becomes significant implying that in the energy spectrum the elastic peak will be shifted by this value from the position corresponding to the incident energy. Therefore the elastic peaks, formed by electrons elastically backreflected from different elements in the sample, split up into separate components. Due to this fact, EPES can be utilized to quantify relative concentrations of different elements in the target in particular light elements such as hydrogen [20, 21, 22, 23, 24, 25]. This constitutes a great advantage since by means of other electron spectroscopy techniques, such as XPS, hydrogen cannot be detected. The problem remains as to elastic peaks positioned at higher recoil energy losses are superimposed on the inelastic background. It is then essential for a quantitative interpretation of the elastic peaks to subtract the inelastic background in a meaningful way. In order to do this, knowledge on the Differential Inverse Inelastic Mean Free Path (DIIMFP) is required which is an important quantity describing inelastic scattering.

The DIIMFP is defined as the distribution of energy losses in an individual inelastic scattering process. When the DIIMFP is known it can be used to retrieve optical

constants of the solid [26]. On the other hand, using optical measurements and linear response theory represents an attractive way to obtain the DIIMFP [27, 28]. However, measuring the optical response in terms of the refractive index and the extinction coefficient in a wide wavelength range is known to be not straightforward [28, 26]. This requires the use of monochromated synchrotron radiation or different sources and monochromators for a different range of wavelengths [26]. In the case of transmission measurements, samples with different thicknesses are required. All this points out to the use of considerable experimental resources. The EELS technique represents an alternative method to experimentally determine the DIIMFP. When using electrons instead of photons, a wide range of energy losses is accessible in the same experiment which poses no significant challenge [29]. The retrieval of the DIIMFP from electron energy loss spectra is performed using deconvolution and fitting algorithms. Note that the determination of the DIIMFP from an energy loss measurement is complicated on one hand by the fact that multiple scattering occurs so that contributions of $n-$fold scattered electrons overlap. On the other hand, due to the presence of the vacuum-surface interface, the energy loss law in the near surface region differs from those deep inside the bulk of the solid [30]. Commonly the DIIMFP refers to bulk excitations and the so-called Differential Surface Excitation Probability (DSEP), defined as the distribution of energy losses in a single surface crossing, refers to surface excitations. The deconvolution method proposed by Werner et al. [26] implies two EELS spectra acquired in bulk and surface sensitive modes. The authors have demonstrated that results of this approach yields reasonable agreement with predictions of Density Functional Theory (DFT) and generally satisfactorily agree with literature data from optical experiments [27, 28] while significant differences were found in some cases [29]. Furthermore, when a composite material is involved the use of the deconvolution procedure becomes questionable. In this case fitting algorithms can be used to retrieve the DIIMFP. Such an extracting procedure requires multiple calculations of the energy spectrum in order to fit experimental data which makes it significant to have an accurate and non-time-consuming computational method. Recently, the approach first introduced by Ambartsumian [31, 32] for radiative transfer namely the Invariant Imbedding Method (IIM) was demonstrated to be a powerful tool for an accurate prediction of electron energy loss spectra [33, 34, 35, 36, 37]. The numerical solution of the system of Ambartsumian-Chandrasekhar linear equations received within the IIM was shown to be very efficient with respect to performance [35]. However, the IIM does not account for the energy dependence of interaction characteristics such as the DIIMFP and IMFP implying the so-called Quasi-Elastic (QE) approximation. This means that all scattering properties are determined for the incident energy and remain

fixed during the slowing down of electrons in the solid. The mean energy loss is indeed known to exhibit a weak energy dependence for medium and higher energies (above 500 eV) whereas for electrons at lower energies (below 100-200 eV) it becomes significant [17]. In particular it is important for the prediction of the SE peak positioned at energies below 50 eV in the spectrum. Thus employing the QE approximation is only valid when the mean energy loss is much less than the electron energy.

Due to the formation of the SE cascade, the SE peak represents the most prominent contribution to the energy spectrum although it remains essentially featureless since the details of interaction processes are smeared out [3]. This is one of the reasons why SE emission is still far from being quantitatively understood. Usually, the quantity of interest is the number of secondary electrons emitted per one primary electron which is known as the so-called Secondary Electron Yield (SEY). The SEY measurements found in the literature are usually performed for incident energies ranging from several eV to several keV [38]. Many authors investigated the SEY developing approaches to describe and predict this value, however, some of them are semi-empirical allowing only qualitative but not quantitative understanding of the SEY. A commonly employed semi-empirical formula to predict the SEY as a function of the incident energy was introduced by Lin and Joy [39]. The authors performed a thorough examination of collected experimental data for 44 elements by means of Monte Carlo calculations in order to derive a universal formula to predict the SEY. However, since there is a spread in experimental data themselves it is difficult to provide a reliable quantification from these data. This yields only a qualitative description of the SEY even though the Lin and Joy approach remains one of the most commonly used.

Another widely used approach to describe the SEE process employs a statistical Monte Carlo simulation [40, 41]. The MC algorithm employs the so-called three-step model implying (1) transport of a primary electron in a solid, (2) generation of a secondary electron, and (3) transport and escape over the surface potential barrier of the produced SE. Already the first step includes some assumptions concerning mechanisms of the emission of SEs. Commonly it is assumed that in each inelastic event a SE is produced with energy $E_{SE} = E_F + \omega$, where ω is the energy transferred from the impinging electron. However, the question remains as to whether each such an event generates a single secondary electron or a swarm of secondaries, instead. Another concern is related to the assumption that SEs are mainly ejected from the Fermi level whereas it is important to consider electron emission from anywhere within the valence band.
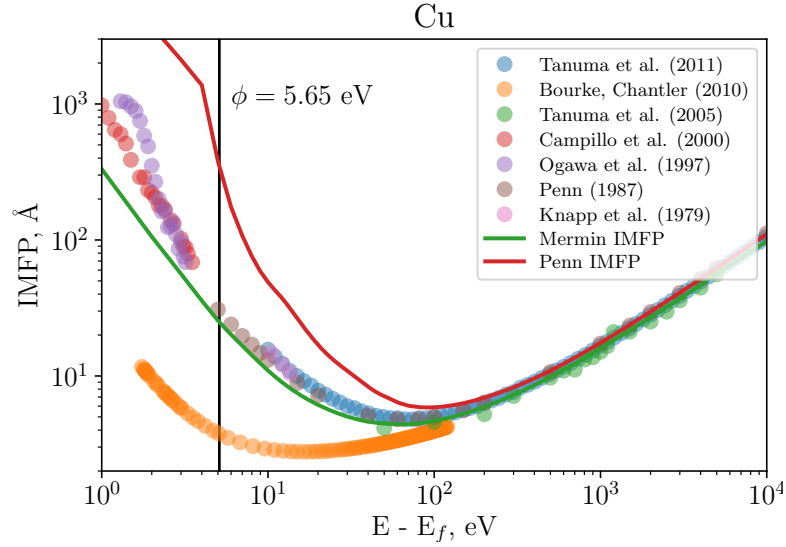
Figure 1.2: Comparison of the IMFP data for Cu calculated using the Mermin dielectric function (solid green curve) [38] and the Penn algorithm (solid red curve) [42]. Data points represent the collection of literature data [43, 42, 44, 18, 45, 46, 47, 48].

The second step describing the transport of SEs requires a quantitative knowledge of electron scattering processes at energies below 100 eV. In particular, quantitative knowledge of IMFP values at low energies is needed. Fig. 1.2 shows the inelastic mean free path in angstroms against the energy above the Fermi level in eV for copper. Note that the vacuum level is located at the energy of 5.65 eV indicated by the vertical bar marked ϕ being the work function. The solid curves show the energy dependence of the IMFP calculated on the basis of Penn's algorithm (red curve) [42] and the Mermin dielectric function (green curve) [49] which represent two different ways to approximate the dielectric function within linear response theory as will be explained in Section 2.2. Data points show experimentally measured and theoretically calculated values found in the literature [43, 42, 44, 18, 45, 46, 47, 48]. As can be clearly seen from Fig. 1.2 at high electron energies (above 100 eV) the IMFP values measured experimentally or calculated using different theoretical approaches are found to be in a good agreement to each other. Whereas at low energies (below 100 eV) there is a huge spread in these data as depicted in Fig. 1.2. Below 100 eV it is complicated in principle to conceive any experimental method to verify theoretical calculations. As mentioned above, the EPES technique is usually employed for the experimental determination of the IMFP. There is also a number of other experimental techniques but all of them require measurements at low energies, which is essentially a big challenge [38]. The experimental difficulties arising to measure

any physical quantity at low energies include: strictly controlled vacuum conditions, a rigorous sample preparation, and control of stray electromagnetic fields.

Besides the IMFP at low energies the knowledge on the mean inner potential U_i is also lacking or there is a spread between these values in the literature [50]. The value of the inner potential U_i is usually defined as the sum of the Fermi energy E_F and the work function ϕ. For medium energy electrons when $E \gg U_i$ the inner potential does not play a crucial role, whereas for low energy electrons when $E \simeq U_i$ this value becomes essential since it determines the possibility to escape over the surface potential barrier (the last step in the three-step model).

Even though the three-step model represents a simplistic approach it seems to work quite reasonably for many applications such as calculations of energy loss spectra and secondary electron yields and is frequently employed by many authors. Nevertheless, a quantitative prediction of most of the important characteristics of the SEE phenomenon still awaits for a complete description and understanding of this process.

1.2   Outline of the thesis

This thesis is split into two parts dedicated to the investigation of electron transport at both medium and low energies. First, in Chapter 2 the key aspects of electron transport in solids are presented. Chapter 3 describes two computational methods employed in this work for finding a solution to the Boltzmann-type transport equation: the invariant imbedding method and the Monte Carlo simulation. The IIM is employed within the Partial Intensity Approach (PIA) implying the quasi-elastic energy regime. The multi-layered model for the description of REELS and XPS spectra with the inclusion of surface excitations is discussed. The Monte Carlo simulation is based on the direct simulation algorithm and is used in the Slowing Down (SD) energy regime to describe the SEE in solids within the three-step model. Comparisons between the two presented approaches are demonstrated.

In Chapter 4 applications of both approaches (IIM and MC) are shown. In this work, the IIM approach is employed to retrieve the DIIMFP using a direct fitting algorithm for the investigation of the structural evolution at the thermal reduction of graphene oxide. Furthermore the possibility to use the IIM for the interpretation of hydrogen peaks in EPES spectra is described. This has been pursued employing several electron spectroscopy techniques for an accurate subtraction of the inelastic background from the

EPES spectra of Be-D samples. The application and tests of the MC simulation model are demonstrated using as an example the calculation of the backreflection coefficient as a function of the incident energy for several materials. The implementation of surface excitations is made on the basis of the position-dependent DIIMFP for electrons crossing solid surfaces for different crossing angles and electron distances relative to the crossing point at the surface [51]. The results of MC calculations of the angular distribution of the average number of surface excitations taken from Ref. [52] were used in order to test the MC code developed in this work.

The possibility to extract the information on low energy (below 100 eV) IMFP values from measurements of the SEY at high energies is demonstrated in Chapter 5. The SEY is typically measured over the incident energy range from several eV to several keV and represents the number of the emitted secondary electrons divided by the number of the incident electrons. It is demonstrated in this work that the SEY for arbitrary energies depends sensitively on the IMFP values at low energies (below 100 eV) providing a useful tool to estimate this quantity. The estimation of IMFP values at low energies using analysis of SEYs is performed on the basis of the Monte Carlo simulation of SEE process in solids. For most investigated materials optimum IMFP values are found to be close to those based on the Mermin dielectric function. Therefore the presented approach allows reverse engineering the IMFP at low energies.

An attempt of measuring the IMFP at low energies (1-100 eV) by means of EPES is also discussed in this work. A good agreement of the extracted IMFP values with literature data is obtained at energies above 500 eV whereas at lower energies results are unsatisfactory. First of all, this is due to the fact that below 100 eV it is complicated to perform any measurements at low energies [38]. From the other side, the reliability of obtained IMFPs strongly depends on the theoretical method used for their derivation from measurements. The method used in the present work is well established at medium energies (above 500 eV) whereas at lower energies its reliability can be questionable.

Chapter 2

Electron transport in solids

A quantitative understanding of any electron spectroscopy technique based on the analysis of reflected, transmitted, or photo-emitted electrons from solid surfaces requires an accurate description of the interaction of the probing particles with the target. Many different physical processes play a role in the generation of the outgoing electron signal after such an interaction with the sample which is measured experimentally and then has to be interpreted. In materials with out long-range order the electron transport in a solid can be conveniently described by means of non-coherent scattering of particles [3]. If spin disregarded, the description of the electron transport in the solid requires quantitative knowledge of the processes that cause changes in the electron state given in terms of its direction of motion and the speed [17]. These processes responsible for the change of the direction of motion and the energy of an electron are called elastic and inelastic scattering which will be described further in the text. Before the probing electron is emitted its transport in the solid involves multiple scattering including both elastic and inelastic processes, which makes the resulting signal a complex combination of these effects.

2.1   Elastic scattering in solids

The elastic interaction between an electron and a solid surface involves a deflection of the electron by the (screened) Coulomb field of the nucleus over scattering angle ψ, accompanied by a small recoil energy loss. Due to the large mass difference between electron and atomic nuclei this energy loss is negligible compared to an energy loss

experienced in inelastic collisions. The description of elastic scattering requires data for the Elastic Mean Free Path (EMFP), the total and the Differential Elastic Cross Section (DECS). The latter quantity represents the distribution of polar scattering angle in an individual collision. The azimuthal scattering angles are assumed to be isotropically distributed for spherically symmetric scattering potential. The EMFP is defined as the average path length an electron travels in between two successive elastic collisions. The total elastic scattering cross section σ_{el} is obtained by integrating the DECS $W_{el}\left(\vec{\Omega}, E_0\right) = \dfrac{d\sigma_{el}}{d\Omega}$ over the solid angle Ω:

$$\sigma_{el} = \int\limits_{4\pi} W_{el}\left(\psi\right) d\Omega = 2\pi \int\limits_{0}^{\pi} W_{el}\left(\psi\right) \sin\theta d\theta \qquad (2.1)$$

The EMFP λ_{el} is then given by:

$$\lambda_{el} = \frac{1}{n\sigma_{el}} \qquad (2.2)$$

where n is the atomic density. Different codes are available for the calculation of these data. One of the most reliable and frequently used approaches is the code system ELSEPA [53] which performs relativistic (Dirac) partial-wave calculations for scattering by a local central interaction potential. For atoms and ions, the static-field approximation is adopted, with the potential set equal to the electrostatic interaction energy between the particle and the target, plus an approximate local exchange interaction when the projectile is an electron [53]. Fig. 2.1 shows the DECS in units of a_0^2 per steradian (where $a_0 = 0.529$ Å is the first Bohr radius) for a light (Si) and a heavy element (Au) at various incident energies E_0 calculated using the ELSEPA software. It is seen that the pronounced forward scattering peak can be observed always, irrespective of the energy, for both Si and Au. However, in the case of Au the forward scattering peak is also accompanied by peaks corresponding to larger angle deflections. For Au such oscillations in the angular dependence are observed to be most pronounced at the energy of 500 eV (red curve in Fig. 2.1b). These features, which are sometimes referred to as generalized Ramsauer–Townsend oscillations, are due to interference of the incident with the scattered wave [17]. For light elements, such as Si, the elastic scattering is generally dominated by forwarding deflections over small angles.

When an electron with an incident energy E_0 interacts with the Coulomb field of a nucleus it will be deflected over the scattering angle ψ from its initial direction transferring a small amount of energy to the solid. The energy transfer ΔE between the impinging electron and target atoms depends on the electron energy, the mass of the scattering atom
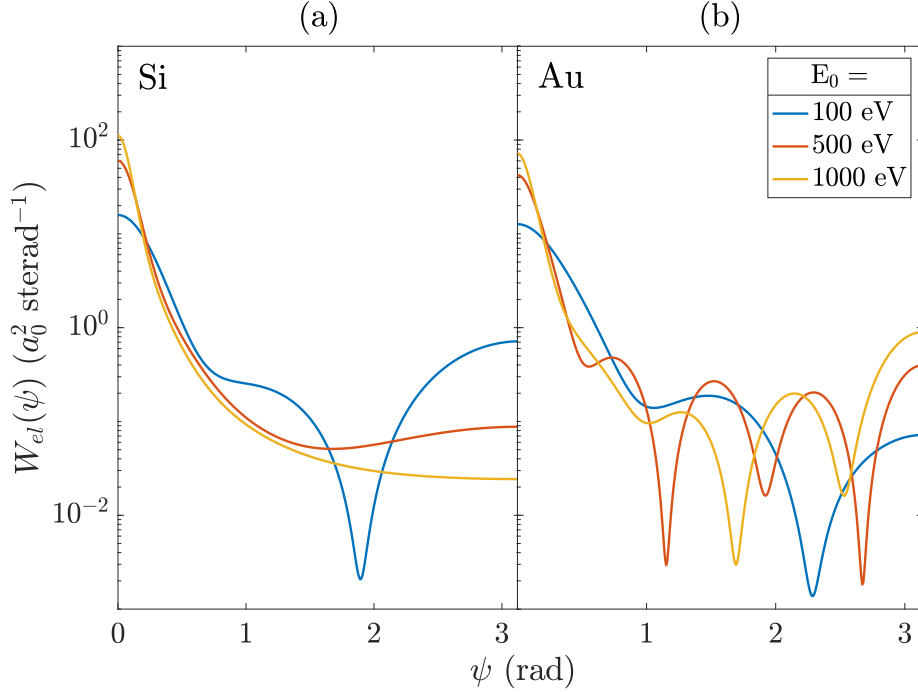
Figure 2.1: Differential cross-section for elastic scattering $W_{el}(\psi)$ of electrons by: (a) Si; and (b) Au atoms at several incident energies: $E_0 = 100$, 500, and 1000 eV.

M, and the scattering angle ψ and is described by the energy/momentum conservation law as follows:

$$\Delta E \approx \frac{2m_e}{M}\left(1 - \cos\psi\right)E_0 \tag{2.3}$$

where m_e is the electron rest mass and the polar scattering angle ψ is given by:

$$\psi = 180° - \arccos\left(\mu_0\mu + \sqrt{1-\mu_0^2}\cdot\sqrt{1-\mu^2}\cdot\cos\varphi\right)$$

where $\mu_0 = \cos\theta_0$ is the cosine of the incident polar angle and $\mu = \cos\theta$ is the cosine of the emission polar angle. φ is the azimuthal angle between the plane of incidence and the plane of emission. Note that the polar scattering angle is given between the initial and final directions after the deflection as depicted in Fig. 2.2 which schematically illustrates the deflection during an elastic scattering event. In this example the situation with the azimuthal angle $\varphi = 0°$ is considered.

Consider the elastic scattering of an electron on a gold atom. The value of ΔE in Eq. 2.3 is then equal to 0.0138 eV assuming a scattering angle $\psi = 180°$ (backscattering) and an incident energy $E_0 = 500$ eV. For higher incident energies the value of ΔE is getting
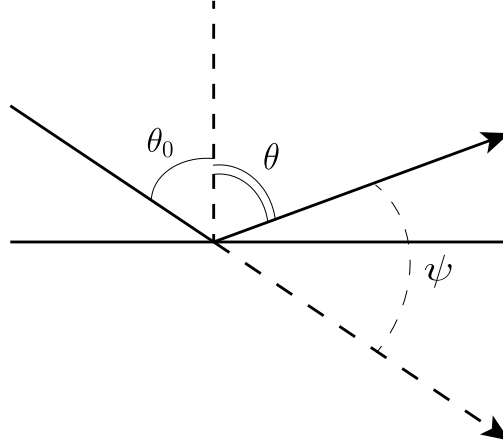
Figure 2.2: Schematic illustration of the deflection in an elastic process. θ_0 is the incident polar angle, θ is the emission polar angle, and ψ is the scattering polar angle. The azimuthal angle $\varphi = 0°$.

larger but it is still much less than those in an inelastic event, an average value of which is $\sim e^2/a_0 = 27.2$ eV as will be shown in Section 2.2. Therefore the recoil energy loss during an elastic event is usually neglected, in particular for heavy elements. What is more relevant is the transferred momentum. It is useful to introduce the so-called Transport Mean Free Path (TrMFP) that measures the momentum transfer along the initial direction [17]:

$$\lambda_{tr}^{-1} = n \int_{4\pi} (1 - \cos \psi) \, W_{el}(\psi) \, d\Omega \qquad (2.4)$$

Since the momentum transfer along the original direction is proportional to $(1 - \cos \psi)$ it becomes comparable to the initial momentum only for large scattering angles $\psi > \dfrac{\pi}{2}$. In other words, only those deflections, for which the transferred momentum is of the order of the original momentum of the impinging particle, mainly contribute to the TrMFP. Therefore the transport mean free path is the typical distance that a particle travels before it 'forgets' its original direction or, in other words, its scattering becomes isotropic owing to large-angle deflections. For materials with high atomic number Z the value of TrMFP is much smaller than those for light elements. For example, for electrons with energy 1000 eV propagating in Au the TrMFP is equal 24.5 Å whereas in the case of Al this value is equal 137.7 Å. It means that the isotropisation process in gold occurs much faster than in aluminum.

2.2 Inelastic scattering in solids

Inelastic scattering involves the interaction of an electron with solid state electrons, accompanied by a small momentum transfer and a large energy loss compared to the recoil energy loss in elastic collisions. The response of the electronic subsystem of the solid to the energy deposition depending on the incident energy of electrons proceeds via different excitation channels including collective plasma oscillations, inner-shell ionization, intrinsic and inter- or intra-band transitions. When intrinsic losses mainly involve a direct energy transfer from probing electrons to electrons in the valence band, the inter- and intra-band transitions consist in the promotion of electrons either from the valence to the conduction band (interband) or within the same band (intraband) [15].

Knowledge of the inelastic scattering properties, such as the Inelastic Mean Free Path (IMFP), the total inelastic cross section and the Differential Inverse Inelastic Mean Free Path (DIIMFP), is important for quantitative understanding of the energy loss process. The DIIMFP $W_{in}(\omega, E_0)$ is defined as the energy-loss probability in an individual inelastic collision and for an electron with energy E_0 is related to the dielectric function $\epsilon(\omega, q)$ as follows:

$$W_{in}(\omega, E_0) = \frac{1}{\pi E_0} \int_{q_-}^{q_+} \text{Im}\left[\frac{-1}{\epsilon(\omega, q)}\right] \frac{dq}{q} \tag{2.5}$$

In expression 2.5 and below, atomic units are used ($\hbar = e = m_e = 1$). The dimensionless quantity $\text{Im}\left[\dfrac{-1}{\epsilon(\omega, q)}\right]$ in Eq. 2.5 represents the so-called Energy Loss Function (ELF) and will be described further in the text. The limits of integration which depend both on the incident energy E_0 and the energy loss ω are a consequence of conservation of energy and momentum, as explained in Fig. 2.3 and are given by:

$$q_{\pm} = \sqrt{2E_0} \pm \sqrt{2(E_0 - \omega)} \tag{2.6}$$

The IMFP is obtained by integrating the DIIMFP over the energy losses:

$$\lambda_{in}^{-1}(E_0) = \int_0^{E_0 - E_F} W_{in}(\omega, E_0)\, d\omega \tag{2.7}$$

The inelastic interaction of charged particles with matter can be described in terms of the dielectric response theory. The dielectric description of inelastic scattering was first introduced by Fermi when he investigated the influence of the polarization of the medium
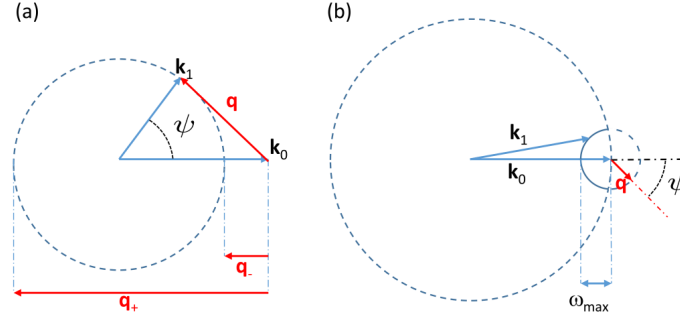
Figure 2.3: Schematic illustration of the kinematics in an inelastic process. (a) The kinematics at constant energy loss ω. The transferred momentum q is the difference in momentum $|k_0| = \sqrt{2m_e E_0}$ before and $|k_1| = \sqrt{2m_e(E_0 - \omega)}$ after the energy loss event and varies from $q_- = |k_0| - |k_1|$ for $\psi = 0°$ to $q_+ = |k_0| + |k_1|$ for $\psi = 180°$; (b) The kinematics at constant magnitude of q. The largest energy loss is $\omega_{max} = k_0^2/2m_e - (k_0 - q)^2/2m_e \simeq qv_0$ for $\psi = 180°$. The dashed part of the small circle corresponds to energy gain, and can not be accessed [54]. Adapted from Ref. [54].

having dielectric properties on the electric field of a charged particle moving through it [55]. The dielectric function $\epsilon(\omega, q)$ is a complex-valued dielectric constant:

$$\epsilon(\omega, q) = \epsilon_1(\omega, q) + i\epsilon_2(\omega, q)$$

where $\epsilon_1(\omega, q)$ and $\epsilon_2(\omega, q)$ are the real (dispersive) and the imaginary (absorptive) part of the dielectric function, respectively. The dielectric function $\epsilon(\omega, q)$ is generally unknown because experimental tools for measuring $\epsilon(\omega, q)$ in the entire domain of changing of the energy transfer ω and the momentum transfer q don't exist. $\epsilon(\omega, q \approx 0)$ in the optical limit can be extracted from optical measurements of the refractive index and the extinction coefficient [27, 28]. If this data are not available one can calculate $\epsilon(\omega, q)$ using model dielectric functions which describe a set of bound electrons as oscillators with weighting amplitudes C_i, binding energies ω_i, and damping parameters Γ_i. The imaginary part of the reciprocal dielectric function or the ELF $\text{Im}\left[\dfrac{-1}{\epsilon(\omega, q)}\right]$ in Eq. 2.5 can be expressed from the modelled dielectric function in terms of ϵ_1 and ϵ_2 as follows:

$$\text{Im}\left[\frac{-1}{\epsilon(\omega, q)}\right] = \frac{\epsilon_2(\omega, q)}{\epsilon_1(\omega, q)^2 + \epsilon_2(\omega, q)^2} \tag{2.8}$$

One of the widely used approaches to describe $\epsilon(\omega, q)$ is the electron gas statistical model which is usually referred to as the Drude-Lindhard model which directly operates with

the reciprocal dielectric function $\epsilon (\omega, q)^{-1}$ [54]:

$$\text{Im} \left[\frac{-1}{\epsilon (\omega, q)} \right] = \sum_i C_i \frac{\omega \Gamma_i \omega_i (q = 0)^2}{\left(\omega^2 - \omega_i (q)^2 \right)^2 + \omega^2 \Gamma_i^2} \tag{2.9}$$

where ω_i is the binding energy which may depend on q, Γ_i corresponds to the damping of the excitation. This width has an important physical interpretation as it is inversely related to the lifetime τ of the excitation [56]. Therefore a small value of Γ_i implies a long-lived excitation lifetime. The sum of the weighting coefficients C_i is related to the free electron density of the solid. A simple dispersion relation is often used to describe the momentum dependence of the resonance frequencies $\omega_i (q)$ given by:

$$\omega_i (q) = \omega_i (q = 0) + \alpha q^2 / 2 m_e \tag{2.10}$$

where α is a constant between 1 (for free electrons in metals) and 0 (for deeper levels and insulators).

A quantum approach of calculating the dielectric function was introduced for a free-electron gas by Lindhard [57]. To express the Lindhard dielectric function $\epsilon_L (\omega, q)$ for an electron gas with density n it is convenient to use a few designations: $z = \dfrac{q}{2 v_F}$, $u = \dfrac{\omega}{q v_F}$ and $\chi^2 = \dfrac{1}{\pi v_F}$, where v_F is the Fermi velocity defined as $v_F = \sqrt{2 E_F}$ with $E_F = \dfrac{1}{2} \left(3 \pi^2 n \right)^{2/3}$. The density n here is associated with a corresponding density for each oscillator $n = \dfrac{\omega_i^2}{4 \pi}$. By using these dimensionless variables one can write [57, 54]:

$$\epsilon_L (\omega, q) = 1 + \frac{\chi^2}{z^2} \left(f_1 (u, z) + i f_2 (u, z) \right) \tag{2.11}$$

where

$$f_1 (u, z) = \frac{1}{2} + \frac{1}{8z} \left(g (z - u) + g (z + u) \right)$$

$$f_2 (u, z) = \begin{cases} \dfrac{\pi}{2} u, & \text{for } z + u < 1 \\[2ex] \dfrac{\pi}{8z} \left(1 - (z - u)^2 \right), & \text{for } |z - u| < 1 < z + u \\[2ex] 0, & \text{for } |z - u| > 1 \end{cases} \tag{2.12}$$

with $g(x) = (1 - x^2) \, ln \left| \dfrac{1+x}{1-x} \right|$. $\epsilon_L(\omega, q)$ consists of two parts related to the collective plasmon oscillations (described by a delta function) and single-particle excitation. According to the Lindhard dielectric theory there is a plasmon damping or so-called Landau damping at the values of q above a critical momentum transfer value q_c. It means that for $q > q_c$ plasmons decay by transferring all their energy to a single electron. At small values of momentum transfer $q < q_c$ plasmons are supposed to be undamped, therefore relaxation processes at these values are neglected in the Lindhard model, which gives rise to the delta function. However, in real materials plasmon oscillations exhibit a finite lifetime at any q. Mermin added the damping of the plasmon oscillations into Lindhard's description by including a damping constant that represent phonon-assisted electronic transitions via e-ion collisions [49, 56]:

$$\epsilon_M(\omega, q) = 1 + \frac{\left(1 + i\Gamma/\omega\right)\left(\epsilon_L(\omega + i\Gamma, q) - 1\right)}{1 + i\Gamma/\omega \left[\epsilon_L(\omega + i\Gamma, q) - 1\right] / \left[\epsilon_L(0, q) - 1\right]} \quad (2.13)$$

The Mermin model has the dispersion 'built in' so no dispersion relation is needed to calculate the ELF at any value of momentum transfer q. Fig. 2.4 shows the ELF calculated on the basis of the Drude-Lindhard and Mermin models for different q. It is
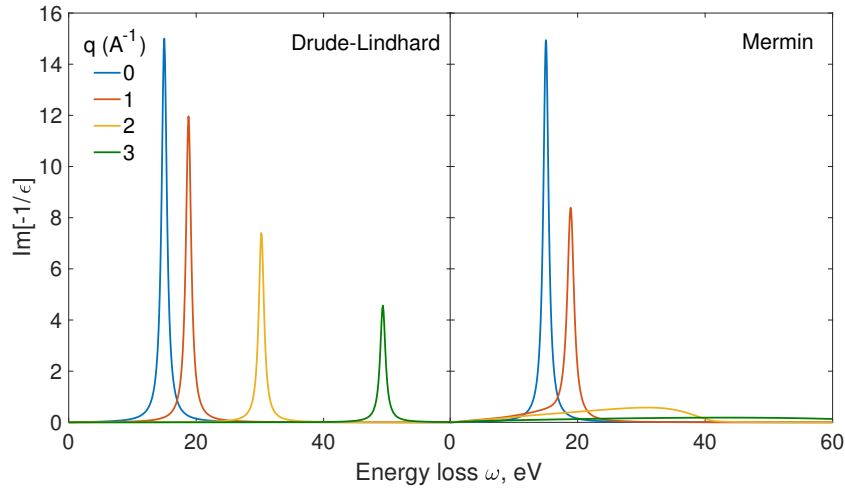

Figure 2.4: Im $\left[\dfrac{-1}{\epsilon(\omega, q)}\right]$ for Drude-Lindhard and Mermin models at the q values as indicated. Parameters were taken from [58]: Drude-Lindhard ($A = 1$, $\omega_i(0) = 15$ eV, $\Gamma = 1$ eV, $\alpha = 1$) and Mermin ($A = 1$, $\omega_i(0) = 15$ eV, $\Gamma = 1$ eV).

clearly seen that away from $q = 0$ the width of the peak in the Mermin ELF increases and becomes much larger than the width of the corresponding Drude-Lindhard loss function [54]. Such a behavior is due to the improved description of damping in the Mermin model which makes it more realistic compared to the Drude-Lindhard model.

Fig. 2.5 shows the DIIMFP for Al and Au for different incident energies. As seen from Fig. 2.5 the DIIMFP of Al has a strong and sharp peak at ≈ 15 eV corresponding to plasmon excitation. Whereas in the case of Au the DIIMFP is seen to be much broader and has a maximum at $\sim e^2/a_0 = 27.2$ eV, corresponding to the binding energies of outer electrons [17]. At low incident energies ($E_0 < 100$ eV) the shape of the DIIMFP considerably changes with the increasing incident energy for both materials. Whereas at higher E_0 ($E_0 > 200$ eV) the shape of the DIIMFP barely depends on the incident energy. Therefore at higher incident energies the mean energy loss is expected to be practically independent of E_0 to a good approximation. The dependence of the DIIMFP on the incident energy is mainly related to the value of the lower limit of integration of the DIIMFP over momentum transfer q_- (Eq. 2.6), which is essential for the outcome of the integral in Eq. 2.5. The momentum transfer during inelastic collisions plays an important role as will be explained below. Fig. 2.6 shows the projection of the ELF for
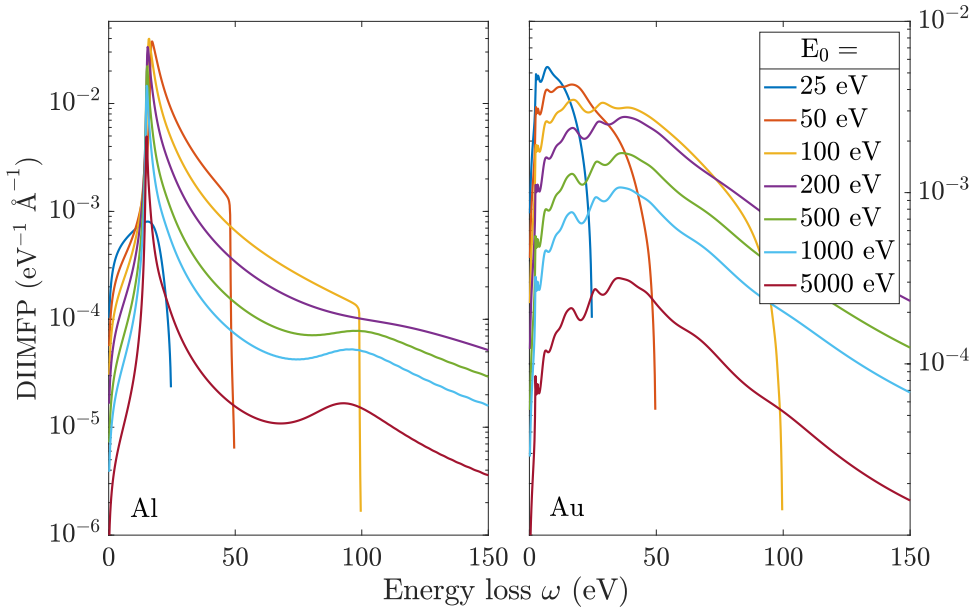

Figure 2.5: Differential inverse inelastic mean free path (DIIMFP) for Al and Au at different incident energies: $E_0 = 25, 50, 100, 200, 500, 1000,$ and 5000 eV.

Al in the (ω, q) plane calculated using the Drude-Lindhard and the Mermin model. Solid

black curves subdivide this projection into three regions describing different inelastic scattering regimes:

- **Region I**: Neither single particles nor collective excitations exist in this region. The lowest possible energy transfer to an electron in the Fermi sea accompanied with a certain momentum transfer can be found as follows:

$$\omega_{low} = -\frac{q^2}{2} + q\sqrt{2E_F}$$

- **Region II**: This domain is defined by collective plasmon excitations, whereas single-particle excitations are not possible. An important quantity to describe the difference in the possibility to excite a collective of particles or to create an electron-hole pair is the critical momentum transfer q_c. In Fig. 2.6 the value of q_c is obtained as a result of the intersection of plasmon line ω_{pl} and ω_{max} curve (will be given further in the text). For momentum transfer values $q < q_c$ collective oscillations have a long lifetime. The corresponding wavelength of such excitation is too long to interact with an individual electron in the Fermi sea. Therefore plasmons are supposed to be "undamped" in this region which means that energy deposited in the solid via plasmon excitation cannot be transferred to a single particle.

- **Region III**: In this region electron-hole pairs creation is dominant. The solid curves depicted in Fig. 2.6, which separate this domain from the others, are plotted according to the conservation rules for Fermi sea electrons, representing the minimum and maximum energy transfer which an electron in the Fermi sea is able to receive which also depends on the corresponding momentum transfer:

$$\omega_{min} = \frac{q^2}{2} - q\sqrt{2E_F}$$
$$\omega_{max} = \frac{q^2}{2} + q\sqrt{2E_F}$$

Individual collisions correspond to the domain where $\epsilon_2(\omega, q) \neq 0$. $\epsilon_2(\omega, q)$ is the part responsible for the damping and it differs from zero only in the domain between these two parabolas, where $q > q_c$ and the collective excitations are damped since $\omega(q)$ is then a possible energy transfer to an individual electron of the Fermi sea [59]. This fact can be also explained in terms of the wavelength, which is getting shorter with the increasing value of momentum transfer and at some point it becomes
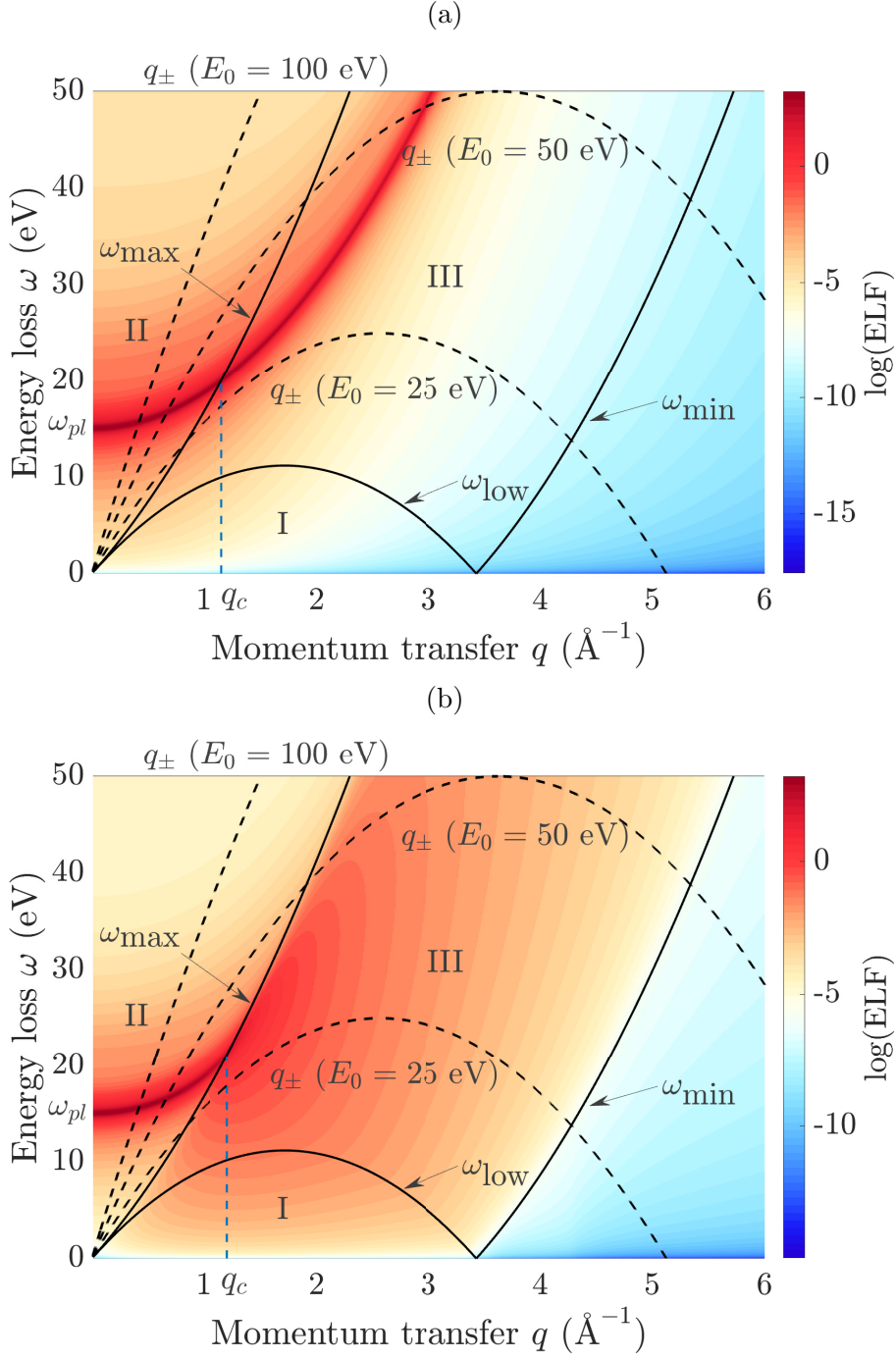
Figure 2.6: Projection of the ELF of Al, calculated on the basis of (a) the Drude-Lindhard (Eq. 2.9), and (b) the Mermin (Eq. 2.13) model dielectric function, in the (ω, q) plane. The dashed black curves correspond to the integration limits q_- and q_+ for different incident energies E_0 according to Eq. 2.6.

31

comparable with the distance between free electrons in the solid. This condition determines the interaction possibility with an individual particle. This implies that either the damping of a plasmon may lead to the creation of an electron-hole pair, or the incoming electron can transfer part of its energy directly to a target electron by means of a knock-on collision. The cut-off momentum transfer q_c in terms of wavelength can be conceived as the cut-off wavelength λ_c in the photoelectric effect, that is only photons with a specific wavelength (or the threshold frequency), depending on the material, are able to generate photoelectrons. Thus, the damping of collective excitations leads to significant contribution to SEE.

In general words it can be deduced that a plasmon can be considered as a collective excitation (or a quasi-particle) only for low values of the momentum transfer q. The corresponding wavelength associated with a particle is related to its momentum as $\lambda = h/p = 2\pi/k$. When the plasmon wavelength is larger than the average distance between free electrons, it can not transfer its energy to a single particle in the solid, however it can interact with a collective of particles. With the value of momentum transfer increasing the scattering becomes single-particle, the plasmon line enters the single-scattering region. As a consequence, plasmon oscillations have a rapid decay with the generation of a SE.

An important feature in Fig. 2.6 concerns the different description of damping in the Drude-Lindhard and the Mermin models as it was discussed earlier in Fig. 2.4. It is clearly seen that the plasmon remains undamped in the case of the Drude-Lindhard approach at $q < q_c$ while for higher values of momentum transfer only a slight damping is observed when the scattering becomes single-particle (Fig. 2.6A). Whereas in the case of the Mermin approach plasmons are seen to be strongly damped at $q > q_c$ in region III but a slight damping is observed also at $q < q_c$ (Fig. 2.6B).

Furthermore, another important point concerning the integration limits $q_\pm$ needs to be discussed. In Fig. 2.6 the integration limits $q_\pm$ (Eq. 2.6) as a function of energy loss are shown by dashed parabolas for different values of the incident energy E_0 as indicated. The left-hand half of the parabolas relates to the lower integration limit over momentum transfer q_- and the right-hand half relates to the upper limit q_+. As can be seen from Fig. 2.6 for low incident energies ($E_0 = 25$ eV) the minimum momentum transfer q_- is always almost entirely lies in Region III which means that the main contribution to the DIIMFP is made up by single-particle excitations but not by plasmons, since they cannot be excited at such low values of the incident energy. At higher incident energies

($E_0 > 50$ eV) the integration domain over momentum transfer covers both collective and single-particle excitation regions. As can be clearly noted in Fig. 2.6 the ELF along the plasmon line has the highest intensity, getting lower for higher values of the momentum transfer due to the damping. Therefore the most contribution to the DIIMFP is made up by plasmons. Since for incident energies above 100 eV the way the lower integration limit q_- crosses the most prominent plasmon features in Region II does not considerably change with the increasing incident energy the shape of the DIIMFP in Fig. 2.5 is seen to remain similar. Whereas the intensity of the DIIMFP is observed to decrease for higher E_0 since the integration domain becomes larger giving rise to a slight contribution to the right shoulder of the DIIMFP at higher losses.

Already here one can deduce that the inelastic scattering at low incident energies significantly differs from those at higher E_0. Any change in the DIIMFP can influence secondary electron emission being the result of the inelastic interaction of probing electrons with the solid. Plasmon decay was shown to be the main mechanism for the generation of SEs. An important question remains: how far the plasmon propagates from its creation region until its decay. There is not much data available on the MFP for plasmon decay. The correct way of treating this process is still not clear and further study should be carried out, theoretically and experimentally [60].

2.2.1   Calculation of the DIIMFP using optical data

The analytical expressions given by the Drude-Lindhard and Mermin dielectric functions provide a convenient framework to calculate the dielectric properties in the entire (ω, q)-plane. Parameters for the model dielectric function are usually determined by fitting the ELF to optical data, which are much more widely available [27, 28]. The dielectric function $\epsilon(\omega, q)$ with ω the energy loss and q the transferred momentum provides an important connection between measurable optical properties of materials and their electronic response to an external excitation. Such optical constants are the refractive index n and extinction coefficient k. By measuring these constants the dielectric function $\epsilon(\omega, q)$ at $q \approx 0$ can be then determined through the relations:

$$\begin{aligned}
\epsilon_1(\omega, 0) &= n^2 - k^2 \\
\epsilon_2(\omega, 0) &= 2nk
\end{aligned} \tag{2.14}$$

The ELF in the optical limit can be calculated as follows:

$$\text{Im}\left[\frac{-1}{\epsilon\left(\omega, q \approx 0\right)}\right] = \frac{\epsilon_2\left(\omega, 0\right)}{\epsilon_1\left(\omega, 0\right)^2 + \epsilon_2\left(\omega, 0\right)^2} = \frac{2nk}{\left(n^2 - k^2\right)^2 + \left(2nk\right)^2} \qquad (2.15)$$

Usually, the experimental ELF in the optical limit $\text{Im}\left[-\frac{1}{\epsilon}\left(\omega, q \approx 0\right)\right]$ is fitted with a set of oscillators within a model ELF. Then in order to calculate the DIIMFP defined by Eq. 2.5 one needs to extend the model ELF, using the parameters obtained from the fit, to all finite momentum transfers q. For example, in the case of the Drude-Lindhard model the simple quadratic dispersion from Eq. 2.10 can be used. In the case of the Mermin dielectric function the dispersion is already 'built-in'.

Acquiring such experimental data is not straightforward. In order to measure the optical response using photons in a wide wavelength range different sources and monochromators as well as other optical components are needed [26]. In the case of transmission experiments, accessing a wide wavelength range over which ϵ varies significantly requires measurements on a series of samples with different thicknesses. However, one can avoid these difficulties by using electrons as probing particles instead of photons. Electron scattering experiments are routinely carried out in the Ultra High Vacuum (UHV) equipment and a wide energy range is accessible in a single experiment. This is the reason why the possibility to extract the optical constants using experimental EELS spectra is widely used by many authors [26, 34, 37].

2.2.2 Surface excitations

Surface oscillations of loosely bound electrons in solid were theoretically introduced by Ritchie [30] in 1957. Their experimental observation by Powell and Swan [61, 62] provided convincing evidence for different modes of collective excitation in bulk and surface to exist. The gas of negatively charged electrons and positively charged ions combine into a neutral plasma of the solid. On a simple qualitative model, one can define a sphere of the minimum radius r_0, within which the net charge is equal to zero. The electric field of a fast incoming electron disturbs this equilibrium system by moving a part of the electrons beyond the sphere r_0. It means that some uncompensated charge appears within this sphere causing the electric interaction between charges according to the Coulomb's law. This leads to oscillations of free solid-state electrons or plasmons with the resonance frequency $\omega_{pl} = \sqrt{\frac{e^2 N}{\epsilon_0 m_e}}$, where N is the free electron density, ϵ_0 is the the vacuum permittivity. Such a spherically symmetric situation is acceptable only deep

inside the solid where all electrons are surrounded by other electrons within the same volume. In the near surface layer electrons, compensated the ion charge, contribute only to half of the sphere of the zero net charge due to the solid-vacuum boundary. Hence, the resonance frequency of the surface oscillations $\omega_{pl}^s = \sqrt{\frac{e^2 N/2}{\epsilon_0 m_e}}$ or $\omega_{pl}^s = \frac{\omega_{pl}}{\sqrt{2}}$. Thus, the boundary effect at the solid-vacuum interface causes a decrease in loss at the plasma frequency near the surface.

When an electron with energy E_0 crosses the surface at the angle θ with respect to the surface normal it can experience energy losses during surface excitations. The Differential Surface Excitation Probability (DSEP) is defined as the distribution of an energy loss ω in a single surface crossing. For an electron with energy E the DSEP can be obtained as follows [63]:

$$W_s\left(\omega, \theta, E\right) = \eta_s^-\left(\omega, \theta, E\right) + \eta_s^+\left(\omega, \theta, E\right) \tag{2.16}$$

where the quantity $\eta_s^\pm\left(\omega, \theta, E\right)$ is defined according to the theory of Tung et al. [64] as follows:

$$\eta_s^\pm\left(\omega, \theta, E\right) = \frac{1}{\pi E} \int\limits_{q_-}^{q_+} \mathrm{Im}\left[\frac{\left(\epsilon\left(\omega, q\right) - 1\right)^2}{\epsilon\left(\omega, q\right)\left(\epsilon\left(\omega, q\right) + 1\right)}\right] \frac{|q_s| dq}{q^3} \tag{2.17}$$

with q_s being the parallel component of momentum transfer along the surface plane:

$$q_s = \left[q^2 - \left(\frac{\omega + q^2/2}{\sqrt{2E}}\right)^2\right]^{1/2} \cos\theta \pm \left(\frac{\omega + q^2/2}{\sqrt{2E}}\right) \sin\theta \tag{2.18}$$

It is important to introduce the so-called Surface Excitation Parameter (SEP) defined as the average number of surface excitations an electron experiences when it crosses the surface once. The total SEP $\eta_s\left(\theta, E\right)$ is obtained by integrating the DSEP $W_s\left(\omega, \theta, E\right)$ over the energy loss ω. Knowledge of this quantity allows to evaluate the probability for a certain number of surface excitations to occur in a single surface crossing in a straightforward way by involving Poisson statistics [63].

Since in the Tung model the normal component of momentum transfer is not taken into account the conservation of energy and momentum is not completely satisfied. The authors of Ref. [51] performed theoretical derivations of the position and direction dependent total DIIMFP $W_{in}^{s \to v}\left(\omega, \theta, E, r\right)$ describing the probability for bulk and surface excitations for electrons crossing the solid surface for different crossing angles θ and electron distances r relative to the crossing point at the surface. In the case of an electron

traveling from solid to vacuum the total DIIMFP is given by [51]:

$$
W_{in}^{s \to v}(\omega, \theta, E, r) = \frac{2}{\pi v^2} \int_{q_-}^{q_+} \mathrm{Im}\left[\frac{-1}{\epsilon(\omega, \vec{q})}\right] \Theta(-r) \frac{dq}{q} -
$$

$$
- \frac{2\cos\theta}{\pi^3} \int_{q_-}^{q_+} dq \int_0^{\pi/2} d\alpha \int_0^{2\pi} d\varphi \frac{q \sin^2\alpha \cos(q_z r \cos\theta) \exp(-|r| Q \cos\theta)}{\widetilde{\omega}^2 + Q^2 v_\perp^2} \mathrm{Im}\left[\frac{-1}{\epsilon(\omega, \vec{Q})}\right] \Theta(-r) +
$$

$$
+ \frac{4\cos\theta}{\pi^3} \int_{q_-}^{q_+} dq \int_0^{\pi/2} d\alpha \int_0^{2\pi} d\varphi
$$

$$
\times \frac{q \sin^2\alpha \cos(q_z r \cos\theta) \exp(-|r| Q \cos\theta)}{\widetilde{\omega}^2 + Q^2 v_\perp^2} \mathrm{Im}\left[\frac{-1}{\epsilon(\omega, \vec{Q}) + 1}\right] \Theta(-r)
$$

$$
+ \frac{4\cos\theta}{\pi^3} \int_{q_-}^{q_+} dq \int_0^{\pi/2} d\alpha \int_0^{2\pi} d\varphi
$$

$$
\times \frac{q \sin^2\alpha \exp(-|r| Q \cos\theta)}{\widetilde{\omega}^2 + Q^2 v_\perp^2} \mathrm{Im}\left[\frac{-1}{\epsilon(\omega, \vec{Q}) + 1}\right]
$$

$$
\times \left[2\cos\left(\frac{\widetilde{\omega} r}{v}\right) - \exp(-|r| Q \cos\theta)\right] \Theta(r) \quad (2.19)
$$

where $\widetilde{\omega} = \omega - qv \sin\alpha \cos\varphi \sin\theta$, $Q = q\sin\alpha$, $q_z = q\cos\alpha$, $v_\perp = v\cos\theta$, and $\Theta(r)$ is the Heaviside step function. The integration limits $q_\pm$ are given by Eq. 2.6. The terms involving $\mathrm{Im}\left[\frac{-1}{\epsilon+1}\right]$ relate to surface excitations whereas terms involving $\mathrm{Im}\left[\frac{-1}{\epsilon}\right]$ relate to bulk excitations. Fig. 2.7 shows the total DIIMFP (data represented by the green curve) with the contribution of surface and bulk components calculated using Eq. 2.19 for electrons escaping from different depths inside a gold sample along the surface normal with energy $E = 100$ eV. Data represented by the blue curve relates to the first term in Eq. 2.19 which represents the DIIMFP describing true bulk excitations (as in Eq. 2.5) and is independent of depth. However, in the vicinity of the surface, the bulk excitations become depolarized due the presence of the surface leading to a decrease of the bulk modes near the surface [65]. This phenomenon is often referred to as the "Begrenzungs effect" after the German word for boundary [30, 64, 66]. The decrease of the bulk modes is described by a result of the subtraction of the second term from the first term in

Eq. 2.19. The resulting reduced contribution of bulk to the total DIIMFP due to the presence of the surface shown by the red curve in Fig. 2.7. The third and the fourth terms in Eq. 2.19 relate to the probability of surface excitations inside and outside the solid, respectively. In Fig. 2.7 the contribution of these terms is shown by the yellow curve. Therefore, the total DIIMFP (the green curve) is given by the sum of the reduced bulk and surface contributions represented by the red and yellow curves, respectively. Fig. 2.7 clearly demonstrates a decreasing of the contribution of surface excitations to the total DIIMFP for further distances away from the surface giving rise to an increasing contribution of bulk excitations.

Figure 2.7: The DIIMFP calculated using the Mermin dielectric function for an electron escaping from Au to vacuum with energy $E = 100$ eV along the surface normal ($\theta = 0°$) for different depths inside the solid: $r = 0$, 0.5, and 1 Å. Data labelled "clear bulk" represent the true bulk excitations whereas data labelled "reduced bulk" relate to the reduced contribution of bulk to the total DIIMFP due to the presence of surface excitations labelled "clear surface".

The Inverse Inelastic Mean Free Path (IIMFP) $\left(\lambda_{in}^{s\rightarrow v}\right)^{-1}(\theta, E, r)$ is obtained by integrating $W_{in}^{s\rightarrow v}(\omega, \theta, E, r)$ over energy losses:

$$\left(\lambda_{in}^{s\rightarrow v}\right)^{-1}(\theta, E, r) = \int_0^E W_{in}^{s\rightarrow v}(\omega, \theta, E, r)\, d\omega \qquad (2.20)$$

The depth distribution of the IIMFP $\left(\lambda_{in}^{s\rightarrow v}\right)^{-1}(\theta, E, r)$ is shown in Fig. 2.8 for electrons escaping from different depths inside a gold sample along the surface normal with energy $E = 100$ eV. It is seen that the surface IIMFP represented by the blue line decays rapidly both into vacuum ($r < 0$) and into the solid ($r > 0$). A characteristic width of the surface scattering zone is seen to be $\sim 1 - 2$ Å which is smaller than, or of the order of, the elastic mean free path. Therefore elastic deflections within the surface scattering zone are expected to be quite rare [65].

The value of the total SEP for escaping electrons is given by the integration of the IIMFP $\left(\lambda_{in}^{s\rightarrow v}\right)^{-1}(\theta, E, r)$ over the surface scattering zone [51]:

$$\eta_s^{s\rightarrow v}(\theta, E) = \int_r \left(\lambda_{in}^{s\rightarrow v}\right)^{-1}(\theta, E, r)\, dr \qquad (2.21)$$

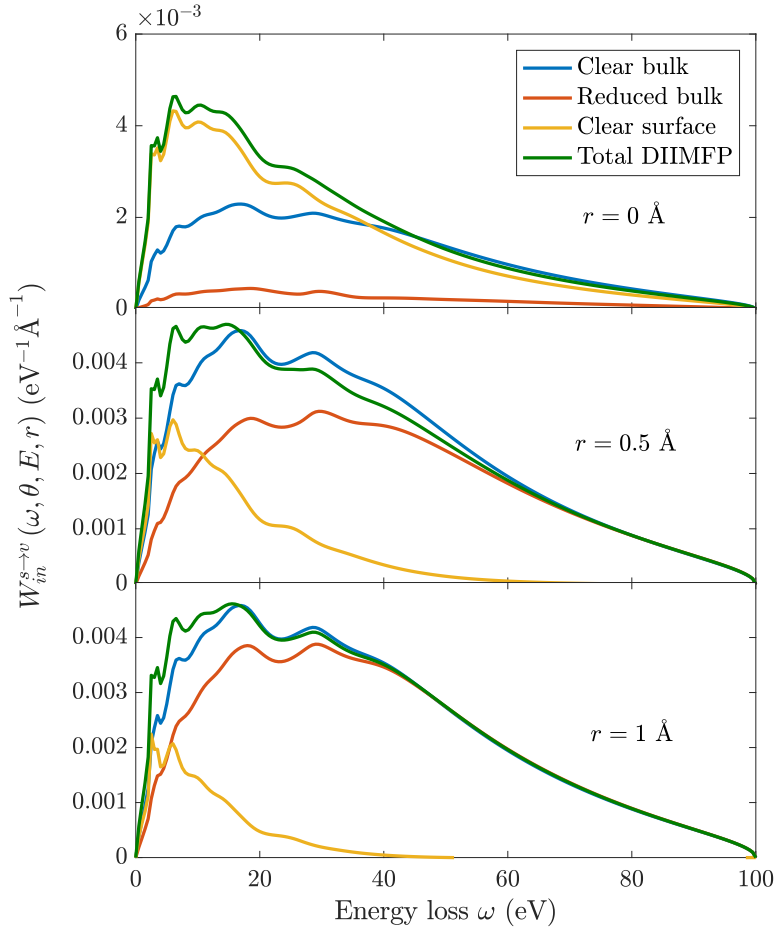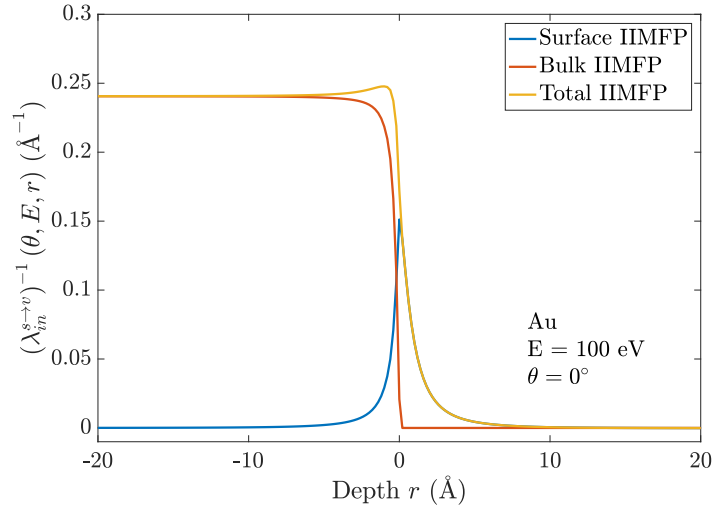**Figure 2.8:** Depth distribution of the IIMFP $(\lambda_{in}^{s\rightarrow v})^{-1}(\theta, E, r)$ calculated using the Mermin dielectric function for an electron escaping from Au to vacuum with energy $E = 100$ eV along the surface normal ($\theta = 0°$).

2.2.3   Inner-shell ionization

During inelastic scattering impinging electrons mainly interact with the electrons in the outer (less tightly bound) shells of atoms in the solid [67]. As a result of such an interaction plasma oscillations of the electron gas or plasmons are excited. However, when an electron energy is sufficient, it can interact with the electrons of the ion inner-shells and cause their ionization. The total IMFP is given by the superposition of partial IMFPs for the corresponding inelastic process as follows:

$$\lambda_{in}^{-1} = \lambda_{pl}^{-1} + \lambda_{ion}^{-1} \tag{2.22}$$

where λ_{pl} is the IMFP between two successive plasmon excitations, and λ_{ion} is the IMFP between two successive inner-shell ionizations. Even if λ_{ion}^{-1} has such a small contribution to the total inelastic cross section, it is non-negligible [59]. A vacancy created in the inner-shell as a result of an energetic electron ionization may be followed by radiative (fluorescence radiation) or nonradiative (Auger) emission. There is a large branching of possible transitions, in particular for heavy atoms. Reliable data on the electron-impact cross sections for ionization λ_{ion}^{-1} for all elements, from hydrogen ($Z = 1$) to einsteinium ($Z = 99$), can be found in Ref. [67]. Various empirical and semi-empirical formulas are also available based on simple physical models and/or fitted to available experimental data [68, 69]. Fig. 2.9 shows the ionization cross sections (in units of squared angstroms) versus incident electron energy E_0 for the L_1 and L_2 shells of Si calculated using different analytical approaches [68, 69, 67]. It is clearly seen from Fig. 2.9 that results given by the formulas of Casnati and Bote (the blue and yellow solid curves) are in a good agreement to each other. Whereas the energy dependence of the ionization cross section represented by Gryzinsky's formula (the red solid curve) considerably differs from the others. In this work the Bote formula from Ref. [67] is used to calculate the ionization cross sections by means of the FORTRAN software provided by the authors.

2.3   Production of secondary electrons

The inelastic scattering of impinging electrons implies an energy and momentum transfer to the solid state electrons. Since energy and momentum are always conserved this energy deposition and momentum transfer brought the electronic subsystem of the solid to an excited state. Quantum mechanically this implies the electronic transitions as the
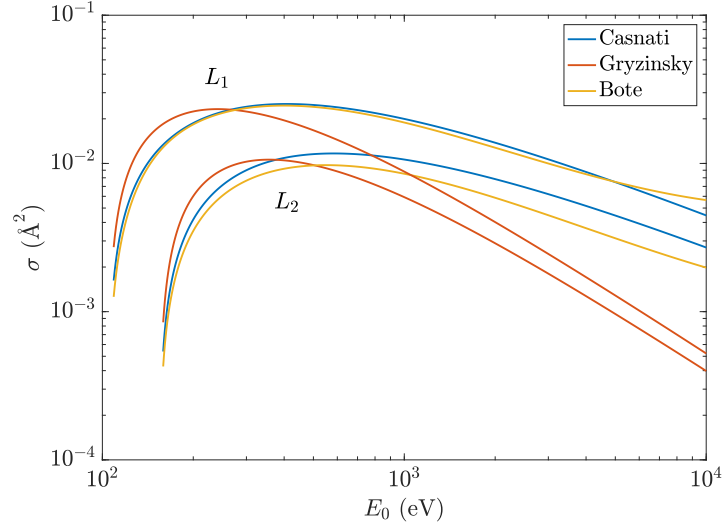
Figure 2.9: Comparison of cross sections for ionization of the L_1 and L_2 shells of silicon atoms by electron impact calculated using the analytical formulas of Casnati (the blue solid curve) [69], Gryzinsky (the red solid curve) [68], and the Bote analytical formula from Ref. [67] (the yellow solid curve) obtained through the FORTRAN software provided by the authors.

most relevant processes, consisting of the promotion of an electron from an occupied to an unoccupied state (provided that the unoccupied state is available) by the energy and momentum transferred in the collision. These available unoccupied states represent accessible channels through which promoted secondary electrons manage to escape above vacuum [3].

In the MC model it is assumed that at each inelastic interaction the energy loss ω, experienced by the primary electron, is transferred to a secondary electron. In the case of the interaction with the valence band the SE produced has the energy $E_{SE} = E_F + \omega$. Here it is assumed that SEs are excited only from the Fermi level. While this is a commonly adopted approach [41], the authors of Ref. [40] took into account the band structure effect, within which the probability distribution of electron excitation in the valence band with a certain energy E is assumed to be proportional to the density of states of a free electron gas:

$$P(E, \omega) \propto \sqrt{E(E + \omega)} \qquad (2.23)$$

where $E < E_F$. The excited secondary electron gains the energy $E_{SE} = E + \omega$. In this case a larger fraction of produced secondary electrons has a smaller energy. The smaller energy SEs have the less their probability to escape over the surface barrier. Therefore

the SEY is decreasing. The question remains whether the only one secondary electron is generated as a result of the inelastic scattering of the primary electron. As it was suggested in Refs. [70, 71] the single electron generation process is indeed dominant. However, the possibility of creating a swarm of secondaries in a single collision cannot be ruled out [3].

In the case of ionization of an inner-shell electron a secondary electron with the energy $E_{SE} = \omega - E_b$ is produced, where E_b is the binding energy of the ionised shell.

Usually in the three-step MC model the momentum transfer during the production of SEs is essentially neglected [38]. The initial angular distribution of SEs is assumed to be isotropic since by the time the electron comes out it completely 'forgets' its initial momentum due to the momentum relaxation after multiple elastic scatterings.

2.4 Escape over the surface potential barrier

The physical model employed in the three-step MC algorithm implies a binary encounter approximation. This approach assumes that the volume occupied by an atom significantly exceeds the volume in which the electron interaction takes place [17]. Thus, electron wavelengths are considered to be smaller than the inter-atomic distance or the electron correlation lengths. This condition is generally satisfied for medium energy electrons, whereas for low energy electrons this is no longer valid since the electron wavelength becomes larger than the inter-atomic distance by several orders of magnitude. However, inside the solid this wavelength is decreased due to the potential step at the surface-vacuum interface as depicted by the purple curve in Fig. 2.10 which shows the model for the potential barrier at the surface-vacuum interface. Since only those electrons that can escape and then be detected are relevant inside the solid, the electron wavelength is always limited by the one corresponding to the inner potential, which is usually of the order of 15 eV. Therefore for electrons which reach vacuum the validity of the employed model is connected to the presence of the surface potential barrier.

A simple model for the potential difference between the vacuum and the solid consists in assuming a step-barrier potential with a height equal to the so-called inner potential U_i [72]. Disruption of the periodicity of the crystal lattice at the surface leads to the potential step, represented by the inner potential U_i as the energy difference between the bottom of the valence band and the vacuum level [38]. Here and below the bottom of the valence band is used as zero for the energy scale. The value of U_i is defined as
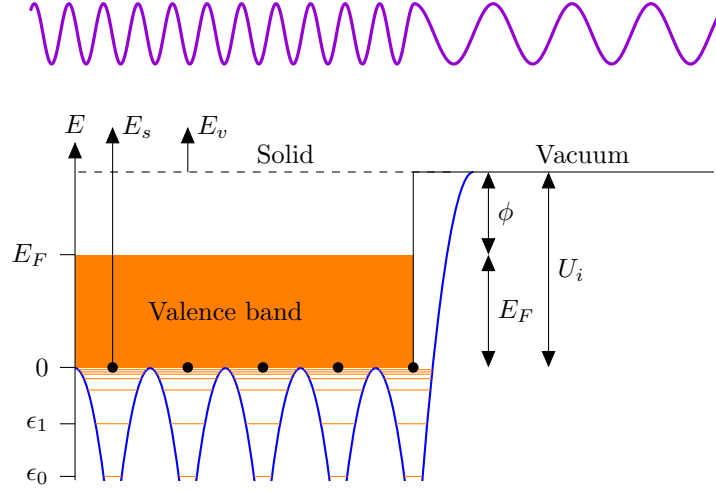
Figure 2.10: Model for the potential barrier at the surface-vacuum interface for metals. The bottom of the valence band is taken as zero energy scale. ϕ and E_F together constitute to U_i. Consequently, the energy in vacuum E_v differs from the energy in solid E_s just by the height of U_i. Adapted from [72].

$U_i = E_F + \phi$, where ϕ is the work function of the solid. The work function ϕ dictates the energy conservation law to be satisfied for electrons escaping from the solid. Electrons with energy $E < \phi$ cannot escape from the solid. The inner potential U_i dictates the momentum conservation law. When an electron, considered as a plane wave, travels from vacuum with a given energy E_v to a medium with the inner potential U_i at any angle other than zero from the normal it will be refracted at the solid surface boundary. The energy of the incoming electron is increased by U_i and the energy of the outgoing electron is decreased by U_i (see Fig. 2.10):

$$
\begin{aligned}
E_s &= E_v + U_i \\
E_v &= E_s - U_i
\end{aligned}
\tag{2.24}
$$

At the boundary between the vacuum and the medium, the wave's phase velocity is changed, usually causing a change in direction. An electron beam traveling along the normal (perpendicular to the boundary) will suffer a change in its energy, but not in the direction according to Snell's law. Consider an electron crossing the solid-vacuum interface. Using the relationship between the energy and momentum

$$
E = \frac{\hbar^2 k^2}{2m}
\tag{2.25}
$$

42

and expanding the momentum into its parallel and perpendicular components

$$E = \frac{\hbar^2}{2m} \left(k_{\parallel}^2 + k_{\perp}^2 \right) = \frac{\hbar^2}{2m} \left(k^2 \sin^2 \theta + k^2 \cos^2 \theta \right) \tag{2.26}$$

let us write a relationship between the energies in vacuum and inside the solid, using only the parallel momentum component as it remains unchanged after crossing the solid surface boundary $k_{\parallel}^s = k_{\parallel}^v$:

$$k_s^2 \sin^2 \theta_s = k_v^2 \sin^2 \theta_v \tag{2.27}$$

or in terms of the energy:

$$\frac{E_s}{E_v} = \frac{\sin^2 \theta_v}{\sin^2 \theta_s} \tag{2.28}$$

Thus, for an electron traveling from vacuum to the solid:

$$\sin \theta_s = \sin \theta_v \sqrt{\frac{E_v}{E_s}} = \sin \theta_v \sqrt{\frac{E_v}{E_v + U_i}} \tag{2.29}$$

where θ_s and θ_v are the polar angles inside the solid and in vacuum, respectively, both defined with respect to the surface normal. For an electron traveling from the solid to vacuum

$$\sin \theta_v = \sin \theta_s \sqrt{\frac{E_s}{E_v}} = \sin \theta_s \sqrt{\frac{E_s}{E_s - U_i}} \tag{2.30}$$

Alternatively, Eqs. 2.29 and 2.30 can be rewritten as follows, respectively:

$$\cos \theta_s = \sqrt{\frac{E_v \cos^2 \theta_v + U_i}{E_v + U_i}} \tag{2.31}$$

$$\cos \theta_v = \sqrt{\frac{E_s \cos^2 \theta_s - U_i}{E_s - U_i}} \tag{2.32}$$

When an electron strikes the solid boundary at an angle larger than a particular critical angle with respect to the surface normal $\theta_s > \theta_c$, it can be reflected back inside the solid instead of escaping over the solid surface. Such a phenomenon is known as total internal reflection. The critical angle θ_c represents the largest possible angle of incidence still resulting in a refracted trajectory and is given by:

$$\sin \theta_c = \sqrt{\frac{E_s - U_i}{E_s}} \tag{2.33}$$

$$\cos \theta_c = \sqrt{\frac{U_i}{E_s}} \tag{2.34}$$

Therefore, the trajectories inside the solid with a polar angle $\theta_s > \theta_c$ are reflected back into the solid. In the case $\theta_s = \theta_c$ the refracted beam travels along the boundary between the two media. In other words, the critical angle θ_c determines an escape cone inside the solid. It means that not only does the electron need to have enough energy to overcome the surface potential barrier ($E > \phi$), but it must also travel toward the surface-vacuum interface within the escape cone with a given solid angle:

$$\Delta\Omega_{esc} = 2\pi \int\limits_0^{\theta_c} \sin\theta d\theta = 2\pi \left(1 - \sqrt{\frac{U_i}{E}}\right) \tag{2.35}$$

For high energy electrons ($E \gg U_i$) the refraction effect at the surface-vacuum interface is negligible whereas for low energy electrons, which are mostly represented by SEs, it becomes crucial since their energy becomes comparable with the value of U_i, which is typically about 15 eV [72]. In other words, the inner potential determines the way the SE peak goes to zero in the electron spectrum. Fig. 2.11 demonstrates the impact of the presence of the refraction effect at the surface-vacuum interface. The green curve is the result of the MC simulation of the SE peak assuming a total absence of the refraction effect. The red curve is the result of the MC simulation including the barrier. The blue curve is calculated using a simple analytic expression aiming to predict the SE peak given by:

$$\frac{dj(E)}{dE} = \exp\left(-\frac{E}{\omega_{\text{mean}}}\right) \cdot \exp\left(-\frac{E_F}{\omega_{\text{mean}}}\right) \cdot \left(1 - \sqrt{\frac{\phi + E_F}{E + E_F}}\right) \tag{2.36}$$

where $dj(E)/dE$ is the differential energy distribution of SEs at the emitted energy E measured with respect to the Fermi level, ω_{mean} is the mean energy loss. As can be seen from Fig. 2.11 when the presence of the barrier is not considered all electrons are able to escape from the solid giving rise to an exponentially increasing intensity of the SE peak (data represented by the green curve). When the barrier is considered this growth is limited due to the formation of the escape cone inside the solid only within which electrons can overcome the surface potential barrier.

Another important question concerns the description of the escape process which is of particular importance since it controls the final shape of the SE peak [73]. The transmission probability over the surface potential barrier can be represented assuming a
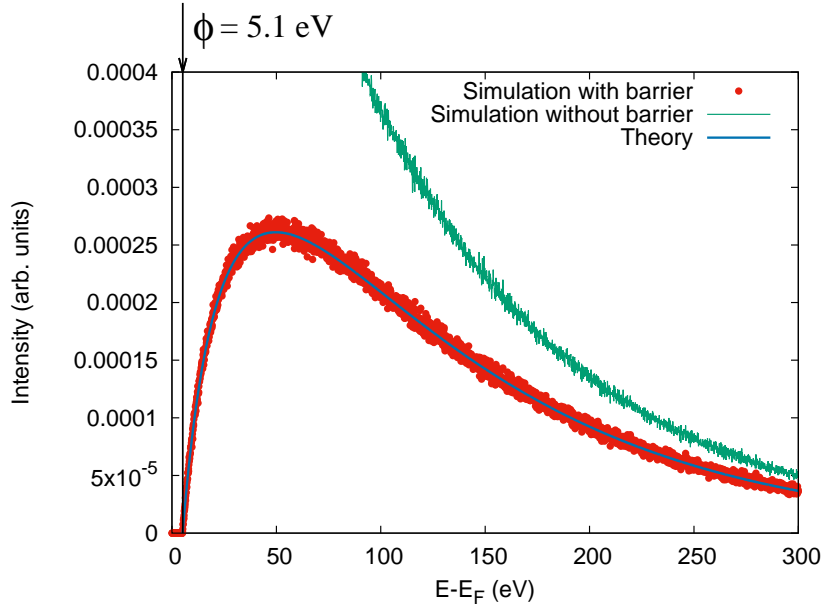
Figure 2.11: Results of the calculations of the SE peak. Red datapoints: MC simulation assuming the presence of the refraction effect at the surface-vacuum interface. Green curve: MC simulation assuming the absence of the refraction effect at the surface-vacuum interface. Blue curve: analytic calculation using Eq. 2.36.

simple step function as follows:

$$
T = \begin{cases} 1 & \text{if } E \cos^2 \theta_s > U_i \\ 0 & \text{otherwise} \end{cases}
\tag{2.37}
$$

Further improvement of the expression describing the transmission probability is accomplished by using the quantum mechanical representation given as follows [74, 41]:

$$
T = \begin{cases} \dfrac{4\sqrt{1 - U_i/E \cos^2 \theta_s}}{\left(1 + \sqrt{1 - U_i/E \cos^2 \theta_s}\right)^2} & \text{if } E \cos^2 \theta_s > U_i \\ 0 & \text{otherwise} \end{cases}
\tag{2.38}
$$

which requires a random number to sample the probability for the electron to escape or to be internally refracted otherwise. As seen from Fig. 2.12 for large escape angles θ_s the difference between the two approaches (Eqs. 2.37,2.38) is bigger than in the case of the electron escape along the angles closer to the surface normal. The quantum

Figure 2.12: Comparison of the transmission coefficient T given by Eqs. 2.37,2.38 for different escape angles θ_s inside the solid with $U_i = 21$ eV.

mechanical transmission probability over the surface potential barrier introduces an additional probability for an electron to be internally refl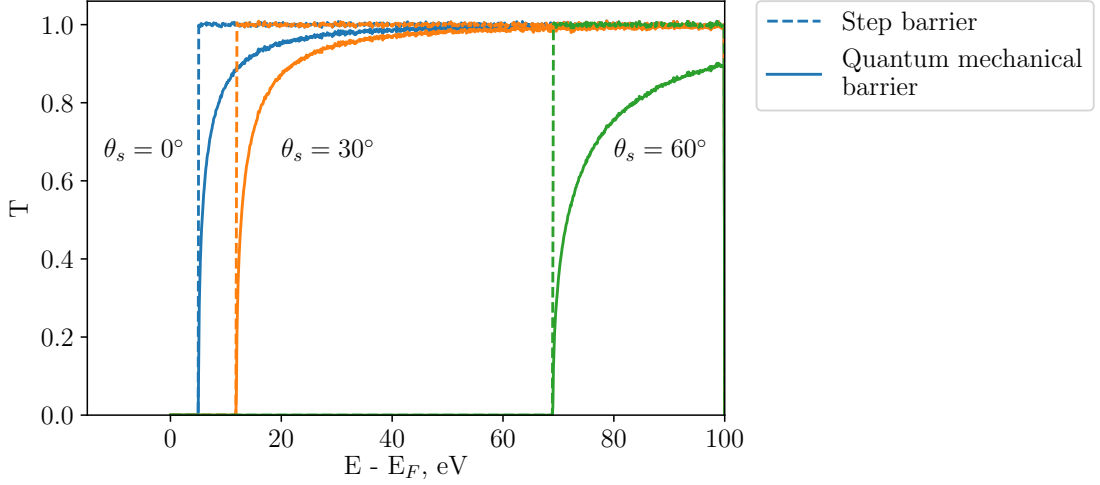ected at the surface boundary. The reflected electrons can additionally lose their energy and therefore a lower number of electrons are able to overcome the surface potential barrier. Fig. 2.13 shows the comparison of SE peaks calculated using the two approaches for the description of the transmission over the surface potential barrier. It is clearly seen from Fig. 2.13 that the use of the quantum-mechanical approach leads to a decreasing of the SE peak.

A final aspect in this section concerns the value of the inner potential U_i. Calculated values of the inner potential can be found in Ref. [50] for most materials. In Ref. [50] theoretical calculations of U_i employ two approaches to determine extreme boundaries for this value. The neutral-atom scattering factors of Doyle and Turner provide an upper bound for U_i [75], whereas a lower limit can be obtained from calculations based on the ionized-free-atom bonding model of Radi [76]. For some materials, the values of U_i between these boundaries show discrepancies of a factor of 2 giving rise to an uncertainty of the inner potential. An empirical approach to evaluate the value of U_i between the two limits was proposed by Ross and Stobbs [77]:

$$\frac{U_i\,(\text{Radi})}{U_i\,(\text{Doyle-Turner})} \approx 0.0325 \frac{Z}{\Omega} + 0.6775 \tag{2.39}$$

where Z is the atomic number and Ω is the volume of a single cell of the lattice. There
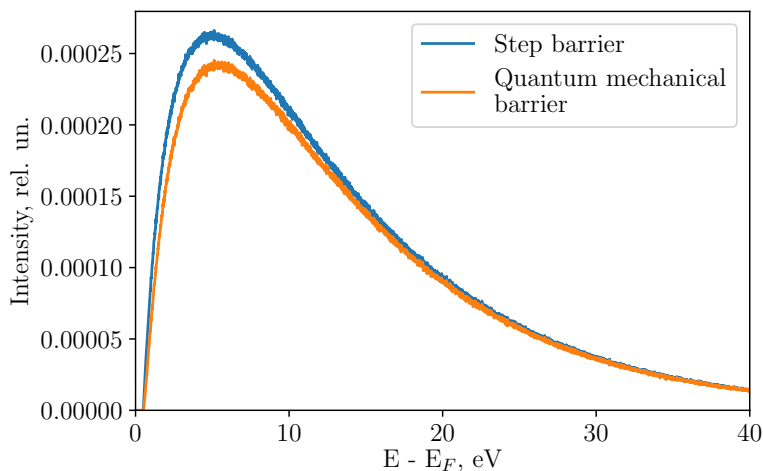
Figure 2.13: Comparison of the intensities of SE peaks calculated using the step and the quantum-mechanical transmission coefficient T given by Eqs. 2.37,2.38. The detection of electrons into the entire hemisphere above the surface is used.

are not a lot of experimental techniques available for measurements of the inner potential and the scatter in measured values found in the literature is wide [50]. Only limited experimental data for U_i are available so far [78]. For example, measurements of U_i using refraction and phase-shifting techniques have been performed Gajdardziska-Josifovska and Carim and can be found in Ref. [50]. Therefore an accurate determination of values of the inner potential is still unresolved question. The influence of the value of U_i on the SEY will be discussed further in the text in Section 5.1.

2.5 Insulators

The energy loss mechanisms for electrons differ in metals and insulators [11]. In metals, electrons lose energy by interacting mainly with the valence band electrons. The kinetic energy of a secondary electron must be more than the value of the inner potential U_i when it reaches the surface in order to escape. The value of U_i for metals is typically about 15 eV. This large minimum escape energy and the high collision probability due to the large number of conduction electrons result in low SEYs for metals. In insulators, the minimum kinetic energy for a secondary electron to escape is the electron affinity χ, represented by the difference between the vacuum level and the bottom of the conduction band as shown in Fig. 2.14. The critical polar angle inside the solid in the case of
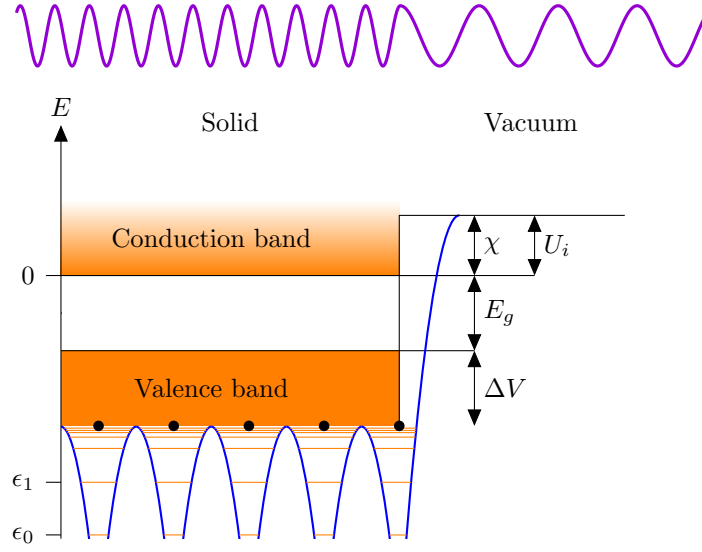
Figure 2.14: Model for the potential barrier at the surface-vacuum interface for insulators. The bottom of the conduction band is taken as zero energy scale. The electron affinity χ is considered to be the mean inner potential U_i for insulators. E_g is the band gap, ΔV is the width of the valence band.

insulators is then given by:

$$\sin \theta_c = \sqrt{\frac{E_s - \chi}{E_s}} \tag{2.40}$$

$$\cos \theta_c = \sqrt{\frac{\chi}{E_s}} \tag{2.41}$$

The value of χ is typically on the order of 1 eV. Electrons mainly lose energy through the excitation of valence band electrons into the conduction band. The wide band gap prevents secondary electrons with kinetic energy less than the band gap energy E_g from participating in such electron-electron collisions. For these electrons, electron-phonon collisions are mainly responsible for the energy loss. Because of the absence of electron-electron scattering, the secondary electron loses much less energy as it moves through material and the escape depth becomes large. Therefore, in general, the SEY in insulators is higher compared to one in metals.

In each inelastic event, provided that $\omega > E_g + E'$, a SE is produced with energy $E_{SE} = \omega - E_g - E'$, where E' is the energy of the target electron in the valence band. The secondary electron which is promoted from the valence band to the conduction band can then participate in the transport process [79]. However, the main mechanism responsible for the creation of cascades of secondary electrons is no longer effective at

energies below E_g. It means that the electrons with energies $E < E_g$ move in the solid without multiplication but they can lose (or gain) energy by interacting with the lattice via electron-phonon scattering [60].

2.5.1   Electron-phonon scattering

A phonon is the quantum mechanical description of an elementary vibrational motion in which a lattice of atoms or molecules uniformly oscillates at a single frequency ω [80]. Solids exhibit two types of phonons: acoustic phonons and optical phonons. The interaction of low energy electrons with Longitudinal Optical (LO) phonons is dominant [81]. The optical energy loss function $\text{Im}\left[\dfrac{-1}{\epsilon\left(\omega, q \approx 0\right)}\right]$ for insulator materials contains the contribution of optical phonons. This allows to calculate the inverse IMFP with inclusion of phonons using the first Born approximation as soon as accurate optical data are available:

$$\lambda^{-1}\left(E\right) = \int_0^{E-E_F} \frac{d\omega}{\pi E} \int_{q_-}^{q_+} \text{Im}\left[\frac{-1}{\epsilon\left(\omega, q\right)}\right] \frac{dq}{q} \tag{2.42}$$

However, the first Born approximation is no longer valid at very low energies where phonons actually exhibit.

According to Fröhlich the inverse IMFP for electron-phonon scattering is given by the expression describing the probability of LO phonon emission ('+') and absorption ('–') [82, 81, 83]:

$$\lambda^{-1}_{e-ph\pm}\left(E\right) = \frac{e^2}{4\pi\epsilon_0\hbar^2}\frac{m_e}{2E}\hbar\omega\left(\frac{1}{\epsilon_\infty} - \frac{1}{\epsilon}\right)\left(N_{LO} + \frac{1}{2} \pm \frac{1}{2}\right)\ln\left(\frac{1 + \sqrt{1 \mp \hbar\omega/E}}{\pm 1 \mp \sqrt{1 \mp \hbar\omega/E}}\right) \tag{2.43}$$

where $\hbar\omega$ is the phonon energy, ϵ is the static dielectric constant, ϵ_∞ is the square of refractive index, N_{LO} is the average number of phonons in one mode at temperature T given by the Bose-Einstein distribution:

$$N_{LO} = \frac{1}{\exp\left(\hbar\omega/k_B T\right) - 1}$$

The authors of Ref. [81] have shown that the IMFP obtained by means of the dielectric theory in context of Eq. 2.42 and presented in Fig. 2.15 corresponds to those calculated by the phonon-assisted model Eq. 2.43. In Fig. 2.15 the IMFP based on the dielectric theory was calculated using the oscillator parameters obtained from the fitting of the model

Drude-Lindhard ELF (Eq. 2.9) to optical ELF [28]. The last allows concluding that the use of the dielectric theory for the first-principle calculation of the IMFP with the inclusion of electron-phonon scattering is possible providing that accurate optical data are available. However, for a more precise description of the electron-phonon scattering, one should use a more reliable phonon-assisted model, e.g. the one based on the Fröhlich theory [82].
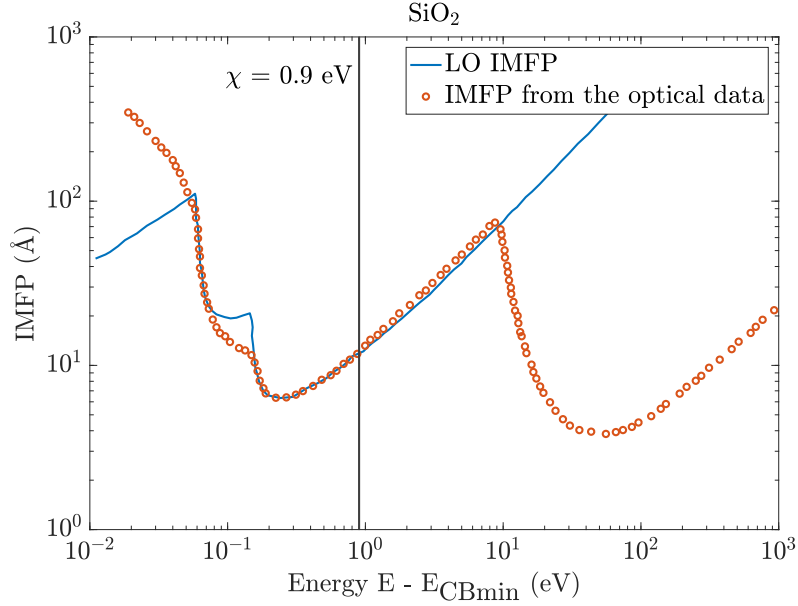
Figure 2.15: The IMFP in SiO₂ based on the dielectric theory Eq. 2.42 (red data points) and Fröhlich theory Eq. 2.43 (LO phonos, blue solid line).

2.5.2 Polaronic effect

The polaron concept was first introduced by Landau in 1933 to describe an electron moving in a dielectric crystal where the atoms move from their equilibrium positions to effectively screen the charge of an electron. An electron induces the polarization field around it when moving in an insulating material. It can then suffer a stabilizing interaction and get trapped in the ionic lattice. Such an effect is essential for quantitative understanding the SEE from insulating targets. The probability for an electron with energy E to get trapped in the ionic lattice is given as follows [79]:

$$\lambda_{trap}^{-1}(E) = S_{trap} \exp\left(-\gamma_{trap}E\right) \tag{2.44}$$

As seen from Eq. 2.44 the lower the electron energy, the more chance for the electron to get trapped. The constant γ_{trap} limits the energy domain and the constant S_{trap} refers to the frequency of this type of process. Moreover, as soon as the electron got trapped as a polaron its mobility is assumed to be neglected.

Therefore the total IMFP for an electron moving in an insulator is given by:

$$\lambda_{in}^{-1} = \lambda_{pl}^{-1} + \lambda_{ion}^{-1} + \lambda_{e-ph}^{-1} + \lambda_{trap}^{-1} \tag{2.45}$$

where λ_{ion}^{-1} is the probability to interact with inner-shell electrons. The SE generated upon the ionization has the energy $E_{SE} = \omega - E_b$.

Chapter 3

Solution of the Boltzmann-type transport equation in non-crystalline media

In Section 1.1 a typical energy distribution of electrons reflected from the solid surface was considered with a detailed description of the three main parts distinguished in the spectrum. Experimentally these data are acquired by means of electron spectroscopy techniques such as EELS and XPS. There are other techniques available which produce the same type of data but in this work, we consider EELS and XPS. In the case of Reflection Electron Energy Loss Spectroscopy (REELS) a target is bombarded with an electron beam with the subsequent acquirement of the energy loss spectrum of reflected electrons. In the XPS technique, the solid surface is irradiated by an X-ray beam. As a result of the interaction of photons with atoms of the solid, photo-electrons are generated with a characteristic energy of core shells. The resulting energy distribution of electrons emitted from the solid surface contains an elastic peak and an inelastic background (as in a REELS spectrum). However, in XPS elastic peaks are positioned at the energy characteristic for certain core shells of atoms in the solid. Therefore this technique allows performing the elemental analysis of the investigated target.

Quantitative interpretation of electron energy loss spectra needs a theoretical description. Assume we have an electron or an X-ray beam incident on a solid surface with incident energy E_0 in direction $\vec{\Omega_0} = \{\mu_0, \varphi\}$ with $\mu_0 = \cos\theta_0$ as schematically depicted in Fig. 3.1. The quantity of interest is the flux density of electrons reflected or emitted from the solid
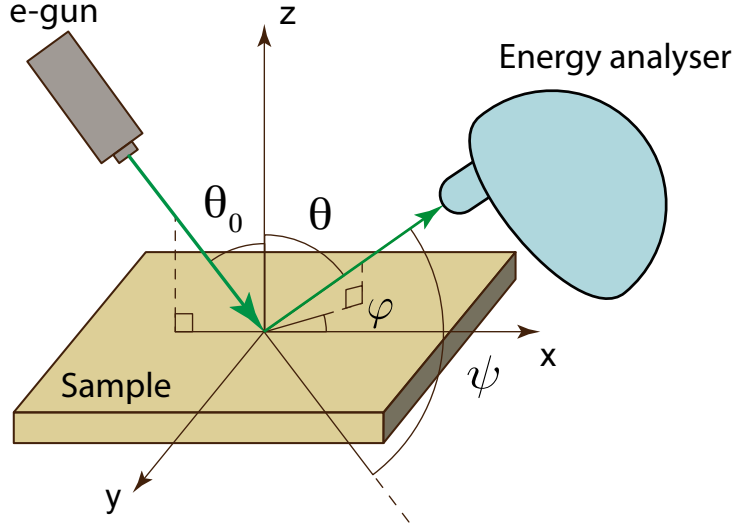
Figure 3.1: Illustration of the experimental geometry. A sample is illuminated by the electron beam (or the X-ray irradiation). Here θ_0 is the polar angle of incidence, θ is the emission polar angle, φ is the azimuthal angle, and ψ is the scattering angle.

in a certain direction above the surface with a certain energy. For this reason, we consider the transport of the electron beam in the solid for the problem of reflection (REELS) or the photon-induced electron emission (XPS). As was discussed in Section 1.1 electron transport in solids implies elastic and inelastic scattering. The DECS $W_{el}\left(\vec{\Omega}, E_0\right)$ and the DIIMFP $W_{in}\left(\omega, E_0\right)$ are used to describe elastic and inelastic scattering, respectively, where ω is the energy loss. Considering a case with plane symmetry, the transport equation for the flux density $N\left(z, \omega, \vec{\Omega}\right)$ of electrons travelling at depth z in direction $\vec{\Omega}$ with energy $E = E_0 - \omega$ due to sources at $z = z_0$ emitting in the direction $\vec{\Omega} = \vec{\Omega_0}$ can be written as follows [17]:

$$
\begin{aligned}
\mu \frac{\partial}{\partial z} N\left(z, \omega, \vec{\Omega}\right) = \ & -\frac{1}{\lambda_{tot}} N\left(z, \omega, \vec{\Omega}\right) + \\
& + \ \frac{1}{\lambda_{in}} \int_0^\omega N\left(z, \varepsilon, \vec{\Omega}\right) x_{in}\left(\omega - \varepsilon, E_0 - \varepsilon\right) d\varepsilon + \\
& + \ \frac{1}{\lambda_{el}} \int_{4\pi} N\left(z, \omega, \vec{\Omega}'\right) x_{el}\left(\vec{\Omega}' \to \vec{\Omega}, E_0 - \omega\right) d\vec{\Omega}' + \\
& + \ f_0\left(E\right) \delta\left(z - z_0\right) \delta\left(\vec{\Omega} - \vec{\Omega_0}\right)
\end{aligned}
\tag{3.1}
$$

Here, $\mu = \cos\theta$ is the polar direction of the electron's motion with respect to the

inward surface normal; λ_{in} and λ_{el} are the IMFP and the EMFP, respectively; $\lambda_{tot} = \lambda_{in}\lambda_{el}/(\lambda_{in} + \lambda_{el})$ is the Total Mean Free Path TotMFP; $f_0(E)$ is the normalized energy distribution at the source; and δ is the Dirac delta-function. $x_{in}(\omega, E_0)$ and $x_{el}(\vec{\Omega}, E_0)$ are the normalized DIIMFP and DECS, respectively:

$$
\begin{aligned}
x_{in}(\omega, E_0) &= \frac{W_{in}(\omega, E_0)}{\int\limits_0^{E_0} W_{in}(\omega, E_0)\, d\omega} \\
x_{el}(\vec{\Omega}, E_0) &= \frac{W_{el}(\vec{\Omega}, E_0)}{\int\limits_{4\pi} W_{el}(\vec{\Omega}, E_0)\, d\vec{\Omega}}
\end{aligned}
\tag{3.2}
$$

fulfilling the following normalization conditions:

$$
\begin{aligned}
\int\limits_0^{E_0} x_{in}(E_0, \omega)\, d\omega &= 1 \\
\int\limits_{4\pi} x_{el}(\vec{\Omega}, E_0)\, d\vec{\Omega} &= 1
\end{aligned}
\tag{3.3}
$$

The first term on the right-hand side of Eq. 3.1 represents the probability that a particle is scattered out of the solid surface either by an elastic deflection or an energy loss event in an inelastic process. The second and third terms represent the gain in the flux density $N\left(z, \omega, \vec{\Omega}\right)$ due to inelastic and elastic collisions, respectively. Eq. 3.1 needs to be complemented with boundary conditions for a given problem (reflection or photo-electron emission).

Finding a solution to the integral-differential transport equation (Eq. 3.1) represents a challenging task [17]. First a simplified version of Eq. 3.1 was considered by Chwolson for the radiative transfer assuming only elastic scattering processes [84, 36]. Schuster and Schwarzschild also investigated this simplified form of Eq. 3.1 dividing the radiation field into an outward and an inward intensity streams [32]. The solution of the obtained system of two equations provides in fact a 'first' approximation for the solution of Eq. 3.1. However, such a division of the radiation field into two streams does not include any effects of the anisotropic scattering or polarisation being extremely important for the radiative transfer. Nowadays one of the exact approaches to find a solution of Eq. 3.1 accounting for the boundary conditions and interaction characteristics is the so-called Partial Intensity Approach (PIA). In reality it is known that the energy and angular variable in the flux density coming from the surface after the interaction of the incident beam with the solid are interrelated [85, 86]. Therefore the flux density cannot be factorized into

functions that depend on the energy and directional variable only. However, assuming that the energy loss process is independent of the deflection process and that energy fluctuations after a given number of inelastic collisions n are weak, it follows that the energy and angular variable in the partial flux density of n-fold scattered electrons should be uncorrelated [17]. Then it is possible to find the formal solution of the transport equation (Eq. 3.1) for the energy spectrum $I\left(\omega, \vec{\Omega}\right)$ in the PIA. The energy spectrum $I\left(\omega, \vec{\Omega}\right)$ is defined as the number of electrons escaping from a unit area of the surface per unit time and energy into a certain direction $\vec{\Omega}$ and is related to the flux density $N\left(z, \omega, \vec{\Omega}\right)$ as follows:

$$I\left(\omega, \vec{\Omega}\right) = \mu N \left(z = 0, \omega, -1 \leq \mu \leq 0\right) \tag{3.4}$$

Therefore the energy distribution $I\left(\omega, \vec{\Omega}\right)$ in the PIA is given by a superposition of the partial loss distributions $L_n\left(\omega\right)$ after n collisions weighted with the number of electrons within the group of n-fold inelastically scattered electrons or the so-called partial intensities C_n [87, 88]:

$$I\left(\omega, \vec{\Omega}\right) = \sum_{n=0}^{\infty} C_n\left(\vec{\Omega}\right) L_n\left(\omega\right) \tag{3.5}$$

Note that the zero-order partial intensity $C_0\left(\vec{\Omega}\right)$ corresponds to the intensity of the elastic peak formed by electrons escaping from the solid without suffering inelastic events. The partial loss distribution $L_n\left(\omega\right)$ represents the n-fold self-convolution of the normalized DIIMFP as follows:

$$L_n\left(\omega\right) = \int_0^{\omega} \overline{x_{in}^{n-1}}\left(\varepsilon\right) x_{in}\left(\omega - \varepsilon\right) d\varepsilon \tag{3.6}$$

where $L_0\left(\omega\right) = \delta(\omega)$, $\overline{x_{in}^0}\left(\omega\right) = \delta(\omega)$, $\overline{x_{in}^1}\left(\omega\right) = x_{in}\left(\omega\right)$.

When the distribution of path lengths s of electrons for the considered problem is known the partial intensities $C_n\left(\vec{\Omega}\right)$ can be found after multiplying the Path Length Distribution (PLD) $K\left(s, \vec{\Omega}\right)$ with the probability for n-fold scattering as a function of the path length $W_n\left(s\right)$ and integrating [17]:

$$C_n\left(\vec{\Omega}\right) = \int K\left(s, \vec{\Omega}\right) W_n\left(s\right) ds \tag{3.7}$$

The PLD can be conveniently calculated employing a Monte Carlo simulation or analytical approaches [89, 90]. However, partial intensities can be directly obtained by means of the so-called Invariant Imbedding Method (IIM) which allows to skip the computation of the PLD. In the following Section 3.1 this approach is described in more detail.

3.1 Invariant imbedding method

As it was shown above in order to compute the partial intensities C_n one has to make an extra step to calculate the path length distribution. However, the concept of invariant imbedding allows computing these coefficients directly by means of the Numerical Solution (NS) of the Ambartsumian-Chandrasekhar (AC) equations which can be derived within the framework of the classical radiative transfer theory [31, 32, 91]. The principles of invariance originally introduced by Ambartsumian [31] stated that the diffusely reflected intensity from a semi-infinite medium cannot be changed if a plane layer of finite thickness having the same scattering properties as those of the medium is added [91]. On the basis of this idea, Ambartsumian [31] obtained a non-linear integral equation for the radiance factor in the case of a semi-infinite medium on the basis of the IIM. Chandrasekhar [32] developed the ideas of Ambartsumian and derived four integral-differential equations for the reflection and the transmission problem for a layer of finite thickness. Dashen first started to use the IIM for electrons [92] inspired by earlier works of Belman [93]. Afanas'ev [33, 94] finalized the general derivation of four nonlinear equations for the transmission and the reflection function for electrons. Borodyansky first employed the IIM for the photo-emission problem using a simplified elastic scattering cross section [89]. The final system of the non-linear AC equations for all three considered problems namely the reflection, the transmission, and the photo-emission can be found in Ref. [36] where it was written down on the basis of the following assumptions:

1. The sample surface is considered as a plane.

2. The sample has amorphous or polycrystalline structure.

3. The sample is homogeneous within the information depth.

4. In the case of the photo-emission problem:

    - processes of reflection and refraction of X-ray beams are neglected.

    - the photon mean free path exceeds the photoelectron IMFP and TrMFP by

several orders of magnitude, and therefore the atoms excited by radiation are assumed to be uniformly distributed inside the sample.

- elastic scattering of photons is assumed to be negligible.

5. The energy dependence of electron scattering characteristics is neglected assuming that they are fixed for the incident energy E_0 and stay the same while an electron slows down in the solid being the essence of the so-called Quasi-Elastic (QE) approximation.

The obtained equations are non-linear and heterogeneous. However, they are more convenient for the solution of the boundary problem for the transport equation from the numerical point of view. The numerical solution of the system of the non-linear AC equations for the reflection, the transmission, and the photo-emission problem was developed by Kaplya [36, 35] based on the discrete ordinate formalism by reducing the AC equations to the algebraic Ricatti and Lyapunov equations.

Let us consider a representative example of using the principles of invariance for the derivation of the non-linear equation for the reflection problem where only elastic scattering processes are considered. For this purpose, it is useful to introduce the so-called reflection function $R(z, \mu_0, \mu, \varphi)$ defined as the number of electrons reflected from a solid layer of thickness z in the direction $\vec{\Omega} = \{\mu, \varphi\}$ divided by the number of electrons incident on the solid surface in the direction $\vec{\Omega_0} = \{\mu_0, \varphi_0 = 0\}$. The derivation of the non-linear equation for the reflection function $R(z, \mu_0, \mu, \varphi)$ involves the following considerations [94, 36]:

1. Consider a layer of thickness z. Let's add a thin layer of the same material of thickness Δz on top of it thereby increasing its thickness by Δz. The added layer is thin enough for multiple scattering to be neglected ($\frac{\Delta z}{\lambda_{tot}} \ll 1$) meaning that only single scattering processes are allowed whereas higher-order scattering processes are ignored assuming that their contribution is negligible with respect to the single scattering processes.

2. The matter of interest is to determine the difference in the reflected electron flow appeared after the addition of the thin layer. This difference is derived by considering possible single scattering processes in the layer Δz.

Consider the reflection function $R(z + \Delta z, \mu_0, \mu, \varphi)$ of the system $(z + \Delta z)$ which is formed by the reduced electron flux reflected from the layer z and the additional electron flux formed as a result of single scattering processes in the layer Δz. Fig. 3.2 schematically
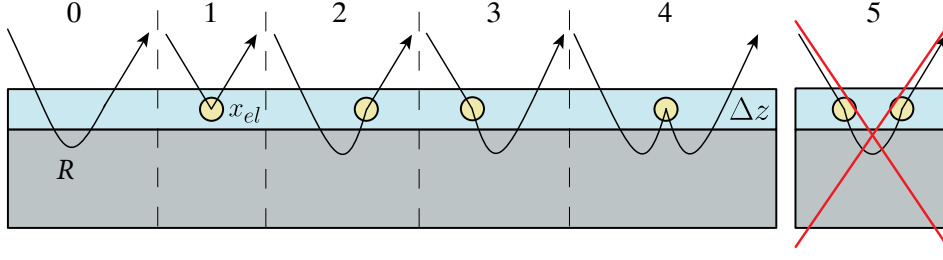
Figure 3.2: Illustration of the reflection processes formed in the layer Δz. Yellow circles: the single elastic scattering. Solid arcs: the reflection function $R(z, \mu_0, \mu, \varphi)$.

demonstrates additional single scattering processes taking place in the layer Δz which are described as follows:

"0": the electron flux reflected from the layer z is reduced due to the presence of the layer Δz which can expressed as follows:

$$R(z, \mu_0, \mu, \varphi) \exp\left[-\frac{\Delta z}{\lambda_{tot}} \left(\frac{1}{\mu_0} + \frac{1}{\mu} \right) \right] \tag{3.8}$$

Eq. 3.8 describes the electrons which travelled through the layer Δz in incoming and outgoing directions without suffering any scattering events.

"1": a single elastic backscattering over the angle of interest in the layer Δz.

"2": after the transport in the substrate layer z the electron direction can be changed into upwards by means of the reflection in the way that the electrons are still outside the detection cone. However, after experiencing a small angle deflection in the course of a single elastic process in the layer Δz the electrons can be scattered into the detector.

"3": the opposite effect can take place, in which electrons first experience a small angle deflection in the layer Δz and then their direction can be corrected into the angle of interest by means of the reflection from the substrate medium.

"4": after the reflection from the substrate with the subsequent elastic backscattering from the layer Δz the electrons can again be reflected from the substrate over the detection angle. This process can take place several times with several subsequent reflections and backscattering though it has a small probability.

"5": higher-order scattering processes are ignored.

Note that all cases "0"–"5" presented in Fig. 3.2 are for the same incidence and emission angles. Let us introduce the '+' and '−' superscripts for the DECS x_{el} referring to the sign of the cosine of the polar angle:

$$
\begin{cases}
x_{\mathrm{el}}^{+}\left(\mu_0, \mu, \varphi\right) = x_{\mathrm{el}}\left(\mu_0, \mu, \varphi\right), & \operatorname{sign}\left(\mu_0 \cdot \mu\right) = 1, \\
x_{\mathrm{el}}^{-}\left(\mu_0, \mu, \varphi\right) = x_{\mathrm{el}}\left(\pm\mu_0, \mp\mu, \varphi\right), & \operatorname{sign}\left(\mu_0 \cdot \mu\right) = -1.
\end{cases}
\tag{3.9}
$$

Here the '−' index is applied for the back scattering, whereas the '+' sign is used for the forward scattering. Therefore the reflection function of the system $z + \Delta z$ can be written as follows:

$$
R\left(z + \Delta z, \mu_0, \mu, \varphi\right) = R\left(z, \mu_0, \mu, \varphi\right) \exp\left[-\frac{\Delta z}{\lambda_{tot}}\left(\frac{1}{\mu_0} + \frac{1}{\mu}\right)\right] +
$$
$$
+ \frac{1}{\lambda_{el}} \cdot \Delta z \cdot x_{el}^{-}\left(\mu_0, \mu, \varphi\right) +
$$
$$
+ \frac{1}{\lambda_{el}} \Delta z \int_0^1 \int_0^{2\pi} R\left(z, \mu_0, \mu', \varphi'\right) x_{el}^{+}\left(\mu', \mu, \varphi - \varphi'\right) d\varphi' \frac{d\mu'}{\mu'} +
$$
$$
+ \frac{1}{\lambda_{el}} \Delta z \int_0^1 \int_0^{2\pi} x_{el}^{+}\left(\mu_0, \mu', \varphi'\right) R\left(z, \mu', \mu, \varphi - \varphi'\right) d\varphi' \frac{d\mu'}{\mu'} +
$$
$$
+ \frac{1}{\lambda_{el}} \Delta z \int_0^1 \int_0^{2\pi} \int_0^1 \int_0^{2\pi} R\left(z, \mu_0, \mu', \varphi'\right) x_{el}^{-}\left(\mu', \mu'', \varphi'' - \varphi'\right) R\left(z, \mu'', \mu, \varphi - \varphi''\right) d\varphi' \frac{d\mu'}{\mu'} d\varphi'' \frac{d\mu''}{\mu''}
\tag{3.10}
$$

By expanding the exponential function $\exp\left[-\frac{\Delta z}{\lambda_{tot}}\left(\frac{1}{\mu_0} + \frac{1}{\mu}\right)\right]$ into a Taylor series:

$$
\exp\left[-\frac{\Delta z}{\lambda_{tot}}\left(\frac{1}{\mu_0} + \frac{1}{\mu}\right)\right] \approx 1 - \frac{\Delta z}{\lambda_{tot}}\left(\frac{1}{\mu_0} + \frac{1}{\mu}\right)
\tag{3.11}
$$

setting Δz to zero and replacing it by dz, and dividing both sides of Eq. 3.10 by dz we receive the following:

$$
\frac{R\left(z + dz, \mu_0, \mu, \varphi\right) - R\left(z, \mu_0, \mu, \varphi\right)}{dz} + R\left(z, \mu_0, \mu, \varphi\right) \frac{1}{\lambda_{tot}}\left(\frac{1}{\mu_0} + \frac{1}{\mu}\right) =
$$
$$
= \frac{1}{\lambda_{el}} x_{el}^{-}\left(\mu_0, \mu, \varphi\right) +
$$

$$+ \frac{1}{\lambda_{el}} \int\limits_{0}^{1} \int\limits_{0}^{2\pi} R\left(z, \mu_0, \mu', \varphi'\right) x_{el}^{+} \left(\mu', \mu, \varphi - \varphi'\right) d\varphi' \frac{d\mu'}{\mu'} +$$

$$+ \frac{1}{\lambda_{el}} \int\limits_{0}^{1} \int\limits_{0}^{2\pi} x_{el}^{+} \left(\mu_0, \mu', \varphi'\right) R\left(z, \mu', \mu, \varphi - \varphi'\right) d\varphi' \frac{d\mu'}{\mu'} +$$

$$+ \frac{1}{\lambda_{el}} \int\limits_{0}^{1} \int\limits_{0}^{2\pi} \int\limits_{0}^{1} \int\limits_{0}^{2\pi} R\left(z, \mu_0, \mu', \varphi'\right) x_{el}^{-} \left(\mu', \mu'', \varphi'' - \varphi'\right) R\left(z, \mu'', \mu, \varphi - \varphi''\right) d\varphi' \frac{d\mu'}{\mu'} d\varphi'' \frac{d\mu''}{\mu''}$$

$$(3.12)$$

Using the dimensionless variable for the thickness $\tau = z/\lambda_{tot}$ yields the equation for the reflection function [33]:

$$\frac{\partial}{\partial \tau} R\left(\tau, \mu_0, \mu, \varphi\right) + \left(\frac{1}{\mu_0} + \frac{1}{\mu}\right) R\left(\tau, \mu_0, \mu, \varphi\right) = \Lambda x_{el}^{-} \left(\mu_0, \mu, \varphi\right) +$$

$$+ \Lambda \int\limits_{0}^{1} \int\limits_{0}^{2\pi} R\left(z, \mu_0, \mu', \varphi'\right) x_{el}^{+} \left(\mu', \mu, \varphi - \varphi'\right) d\varphi' \frac{d\mu'}{\mu'} +$$

$$+ \Lambda \int\limits_{0}^{1} \int\limits_{0}^{2\pi} x_{el}^{+} \left(\mu_0, \mu', \varphi'\right) R\left(z, \mu', \mu, \varphi - \varphi'\right) d\varphi' \frac{d\mu'}{\mu'} +$$

$$+ \Lambda \int\limits_{0}^{1} \int\limits_{0}^{2\pi} \int\limits_{0}^{1} \int\limits_{0}^{2\pi} R\left(z, \mu_0, \mu', \varphi'\right) x_{el}^{-} \left(\mu', \mu'', \varphi'' - \varphi'\right) R\left(z, \mu'', \mu, \varphi - \varphi''\right) d\varphi' \frac{d\mu'}{\mu'} d\varphi'' \frac{d\mu''}{\mu''}$$

$$(3.13)$$

where $\Lambda = \lambda_{el}^{-1}/\lambda_{tot}^{-1}$ is the single scattering albedo.

Introducing the transmission and photo-electron flux density functions the non-linear equations for the transmission and photo-emission problems can be obtained in a similar way [36, 37]. The transmission function $T\left(z, \mu_0, \mu, \varphi\right)$ is defined as the number of electrons transmitted through a solid layer of thickness z in the direction $\vec{\Omega} = \{\mu, \varphi\}$ divided by the number of electrons incident on the solid surface in the direction $\vec{\Omega_0} = \{\mu_0, \varphi_0 = 0\}$. The derivation of the non-linear equation for the transmission function $T\left(z, \mu_0, \mu, \varphi\right)$ proceeds via considering single scattering processes taking place in the layer Δz added on top of the layer z as depicted in Fig. 3.3. Note that the transmission function $T\left(z, \mu_0, \mu, \varphi\right)$ does not describe the electrons that have passed through the layer z without suffering elastic or inelastic scattering. These electrons can be described by the Poisson distribution
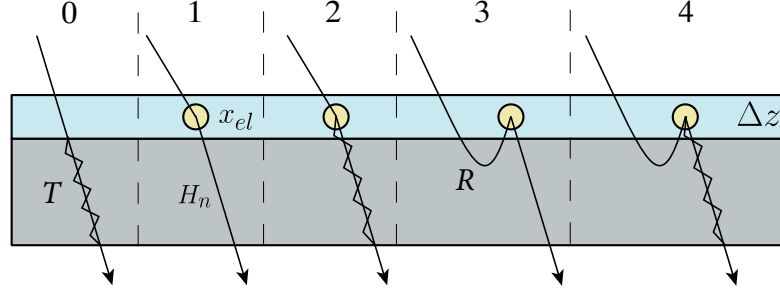
61

Figure 3.3: Illustration of the transmission processes taking place in the layer Δz. Yellow circles: the single elastic scattering. Solid lines: the function $H_n\left(\dfrac{\tau}{\mu}\right)$ describes the electrons that have passed through the layer z without suffering elastic or inelastic scattering. Solid arcs: the reflection function $R\left(z, \mu_0, \mu, \varphi\right)$. Zigzag lines: the transmission function $T\left(z, \mu_0, \mu, \varphi\right)$.

function $H_n\left(\dfrac{\tau}{\mu}\right)$ given by:

$$H_n\left(\frac{\tau}{\mu}\right) = \exp\left(-\frac{\tau}{\mu}\right)\left(\frac{1-\Lambda}{\mu}\tau\right)^n \frac{1}{n!}$$

The photo-electron flux density function $Q\left(z, \mu_0, \mu, \varphi\right)$ is defined as the number of photo-electrons emitted from a solid layer of thickness z in the direction $\vec{\Omega} = \{\mu, \varphi\}$ divided by the number of photons incident on the surface of this layer in the direction $\vec{\Omega_0} = \{\mu_0, \varphi_0 = 0\}$. The derivation of the non-linear equation for the photo-electron flux density function $Q\left(z, \mu_0, \mu, \varphi\right)$ proceeds via considering single scattering processes taking place in the layer Δz added on top of the layer z as depicted in Fig. 3.4. Note that in order to obtain the equation for the transmission function and the photo-electron flux density function, one should first determine the reflection function. In this connection the equation for the reflection function is self-consistent. As seen from Fig. 3.4 in the photo-emission problem the knowledge of the differential photo-ionization cross section $x_{ph}\left(\vec{\Omega_0}, \vec{\Omega}, E_0\right)$ is required to describe the emission of photo-electrons inside the solid which can be calculated using the formalism described in Ref. [95].

In general case when energy loss processes are taken into account the NS implies that the obtained non-linear equations are first discretized in the angular domain by defining a set of Gaussian quadrature points and weights in the polar angle direction. The obtained differential matrix equations can be solved by using either the Backward Differentiation Formula (BDF) [96] or the matrix exponential formalism [97] providing the partial intensities $R_n\left(\vec{\Omega}\right)$, $T_n\left(\vec{\Omega}\right)$, and $Q_n\left(\vec{\Omega}\right)$ to describe the energy loss spectrum
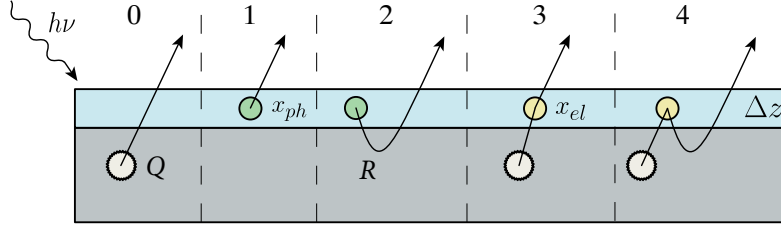
Figure 3.4: Illustration of the photo-electron emission processes taking place in the layer Δz. Green circles: the single photo-electron emission process described by the differential photo-ionization cross section $x_{ph}\left(\vec{\Omega_0}, \vec{\Omega}, E_0\right)$. Yellow circles: the single elastic scattering. Solid arcs: the reflection function $R\left(z, \mu_0, \mu, \varphi\right)$. White circles with zigzag path: the photo-electron flux density function $Q\left(z, \mu_0, \mu, \varphi\right)$.

of reflected, transmitted, and photo-emitted electrons in the PIA, respectively, as follows:

$$
\begin{aligned}
R\left(\omega, \vec{\Omega}\right) &= \sum_{n=0}^{\infty} R_n\left(\vec{\Omega}\right) L_n\left(\omega\right) \\
T\left(\omega, \vec{\Omega}\right) &= \sum_{n=0}^{\infty} T_n\left(\vec{\Omega}\right) L_n\left(\omega\right) \\
Q\left(\omega, \vec{\Omega}\right) &= \sum_{n=0}^{\infty} Q_n\left(\vec{\Omega}\right) L_n\left(\omega\right)
\end{aligned}
\tag{3.14}
$$

The entire computational procedure is implemented using the ESCal software [98] developed on the basis of the object-oriented programming on the MATLAB platform. In Ref. [35] the numerical solution of the system of the AC equations is validated against Monte Carlo simulations and experimental angular distributions of scattered electrons. An agreement within 1% is obtained between them, while the computational time for solving the system of non-linear AC equations is in the order of a second on Intel Xeon CPU E5-1620 3.60GHz (the performance can be enhanced even further by using acceleration techniques for the discrete ordinate method [99] or by parallel computing [100]). Due to the high performance the proposed technique for the calculation of partial intensities can be effectively used in the direct search methods of nonlinear optimization.

3.1.1 Multi-layered systems

As was discussed above the IIM approach can be applied only for homogeneous samples. In the case of the samples consisting of several layers of a different material, the reflection function can be calculated through corresponding reflection functions derived for each of these layers which are homogeneous when considered separately. Fig. 3.5 shows a two-layered system consisting of the top layer of thickness z_1 of one material and a semi-infinite bottom layer of another material. Using dimensionless variable $\tau_1 = z_1/\lambda_{tot}$
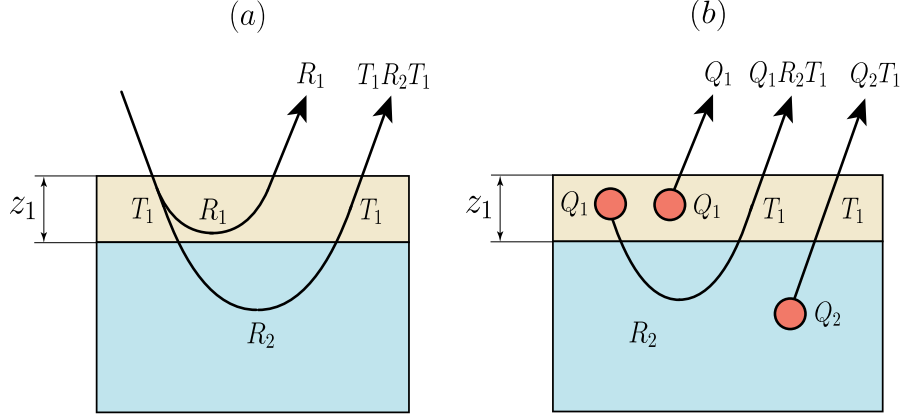
Figure 3.5: Schematic processes of the formation of (a) the reflection; and (b) the photo-emission functions for multi-layered systems.

the reflection function is given by [36, 37]:

$$
R\left(\omega, \mu_0, \mu, \varphi\right) = R_1\left(\tau_1, \omega, \mu_0, \mu, \varphi\right) +
$$

$$
+ \int_0^\omega d\varepsilon \int_0^\varepsilon d\varepsilon' \int_0^{2\pi}\int_0^1\int_0^{2\pi}\int_0^1 T_1\left(\tau_1, \omega - \varepsilon, \mu_0, \mu', \varphi'\right) R_2\left(\varepsilon - \varepsilon', \mu', \mu'', \varphi'' - \varphi'\right)
$$

$$
\cdot\, T_1\left(\tau_1, \varepsilon', \mu'', \mu, \varphi - \varphi''\right) \frac{d\mu'}{\mu'} d\varphi' \frac{d\mu''}{\mu''} d\varphi'' \quad (3.15)
$$

where R_1 and T_1 are the reflection and transmission functions for the top layer, respectively, while R_2 stands for the reflection function of the semi-infinite bottom layer ($\tau_2 \to \infty$). Analogously, the photo-electron flux density for the two-layered system (Fig. 3.5b) reads as follows [36, 37]:

$$
Q\left(\omega, \mu_0, \mu, \varphi\right) = Q_1\left(\tau_1, \omega, \mu_0, \mu, \varphi\right) +
$$

$$
+ \int_0^\omega d\varepsilon \int_0^{2\pi}\int_0^1 Q_2\left(\omega - \varepsilon, \mu_0, \mu', \varphi'\right) T_1\left(\tau_1, \varepsilon, \mu', \mu, \varphi - \varphi'\right) \frac{d\mu'}{\mu'} d\varphi' +
$$

$$
+ \int_0^\omega d\varepsilon \int_0^\varepsilon d\varepsilon' \int_0^{2\pi}\int_0^1\int_0^{2\pi}\int_0^1 Q_1\left(\tau_1, \omega - \varepsilon, \mu_0, \mu', \varphi'\right)
$$

$$
\cdot\, R_2\left(\varepsilon - \varepsilon', \mu', \mu'', \varphi'' - \varphi'\right) T_1\left(\tau_1, \varepsilon', \mu'', \mu, \varphi - \varphi''\right) \frac{d\mu'}{\mu'} d\varphi' \frac{d\mu''}{\mu''} d\varphi'' \quad (3.16)
$$

Here Q_1 and Q_2 are the photo-electron flux densities for the top and bottom layers, respectively.

When the thickness of the top layer is much less than the transport mean free path the trajectories in this layer can be approximated by straight lines. As shown in Ref. [101], the error induced by this assumption does not exceed 3% excluding the cases of glancing sighting angles. Consequently, Eqs. 3.15 and 3.16 can be simplified as follows [36, 37]:

$$
\begin{aligned}
R\left(\omega, \mu_0, \mu, \varphi\right) &= R_1\left(\tau_1, \omega, \mu_0, \mu, \varphi\right) + \\
&+ \int_0^\omega R_2\left(\omega - \varepsilon, \mu_0, \mu, \varphi\right) L\left[\tau_1\left(\frac{1}{\mu} + \frac{1}{\mu_0}\right), \varepsilon\right] d\varepsilon
\end{aligned}
\tag{3.17}
$$

$$
\begin{aligned}
Q\left(\omega, \mu_0, \mu, \varphi\right) &= Q_1\left(\tau_1, \omega, \mu_0, \mu, \varphi\right) + \\
&+ \int_0^\omega Q_2\left(\omega - \varepsilon, \mu_0, \mu, \varphi\right) L\left(\frac{\tau_1}{\mu}, \varepsilon\right) d\varepsilon
\end{aligned}
\tag{3.18}
$$

3.1.2   Inclusion of surface effects

In order to account for surface excitations an energy loss signal from the surface can be described employing the Poisson statistics for plural surface scattering as follows [63, 58]:

$$
I_S\left(\omega, \mu, E_0\right) = \sum_{k=0}^\infty \mathcal{P}_k\left(\eta_s\left(\mu, E_0\right)\right) L_k\left(\omega\right)
\tag{3.19}
$$

where the function $\mathcal{P}_k$ represents the Poisson distribution:

$$
\mathcal{P}_k\left(x\right) = x^k \frac{e^{-x}}{k!}
\tag{3.20}
$$

In Eq. 3.19 the partial loss distribution $L_k\left(\omega\right)$ represents the k-fold self-convolution of the direction dependent DSEP $x_{inS}\left(\omega, \mu, E_0\right)$ (as in Eq. 3.6) which is found after integrating the part of the total DIIMFP (Eq. 2.19) related to surface excitations over all depths outside and inside the solid:

$$
x_{inS}\left(\omega, \mu, E_0\right) = \int_{-\tau_s}^{\tau_s} W_{in}^{s \to v}\left(\omega, \mu, E_0, r\right) dr
\tag{3.21}
$$

where $\pm\tau_s = \pm z_s/\mu$ define the boundaries for the region where surface excitations are considered. "$-$" refers to the vacuum side and "$+$" refers to the inner side of the solid.

Note that according to Eq. 2.19 the total DIIMFP $W_{in}^{s \to v}(\omega, \mu, E_0, r)$ includes both bulk and surface contributions. Whereas in Eq. 3.21 only surface components from this equation are used in order to calculate the DSEP:

$$
W_{in}^{s \to v}(\omega, \mu, E_0, r) = \frac{4\mu}{\pi^3} \int\limits_{q_-}^{q_+} dq \int\limits_{0}^{\pi/2} d\alpha \int\limits_{0}^{2\pi} d\phi
$$

$$
\times \frac{q \sin^2 \alpha \cos(q_z r \mu) \exp(-|r| Q\mu)}{\widetilde{\omega}^2 + Q^2 v_\perp^2} \mathrm{Im} \left[\frac{-1}{\epsilon\left(\omega, \vec{Q}\right) + 1} \right] \Theta(-r)
$$

$$
+ \frac{4\mu}{\pi^3} \int\limits_{q_-}^{q_+} dq \int\limits_{0}^{\pi/2} d\alpha \int\limits_{0}^{2\pi} d\phi
$$

$$
\times \frac{q \sin^2 \alpha \exp(-|r| Q\mu)}{\widetilde{\omega}^2 + Q^2 v_\perp^2} \mathrm{Im} \left[\frac{-1}{\epsilon\left(\omega, \vec{Q}\right) + 1} \right]
$$

$$
\times \left[2\cos\left(\frac{\widetilde{\omega}r}{v}\right) - \exp(-|r| Q\mu) \right] \Theta(r) \quad (3.22)
$$

The value of the total SEP $\eta_s(\mu, E_0)$ in Eq. 3.19 is found by integrating the DSEP $x_{inS}(\omega, \mu, E_0)$ over energy losses. An experimental REELS spectrum can be then described as follows:

$$
R(\omega, \mu_0, \mu, \varphi) = I_S \otimes R_B \otimes I_S \otimes G =
$$

$$
= I_S(\omega, \mu_0, E_0) \otimes \left(\sum_{n=0}^{\infty} R_n(\mu_0, \mu, \varphi) L_n(\omega) \right) \otimes I_S(\omega, \mu, E_0) \otimes G(\omega) \quad (3.23)
$$

where $R_B(\mu_0, \mu, \varphi)$ represents the reflection function from the semi-infinite bulk, and $G(\omega)$ represents the Gaussian function which approximates the broadening of the elastic peak. The symbol $\otimes$ relates to the convolution operator defined as follows:

$$
F_1 \otimes F_2 = \int\limits_{0}^{\omega} F_1(\varepsilon) \cdot F_2(\omega - \varepsilon) \, d\varepsilon \quad (3.24)
$$

The double convolution of the bulk signal R_B with the surface signal I_S is performed due to the fact that electrons cross the surface twice, i.e. during its incoming to and

outgoing from the solid. In fact, the authors of Ref. [51] provide a separate equation for the DIIMFP for electrons travelling from vacuum to solid $W_{in}^{v \to s}(\omega, \mu_0, E_0, r)$, however this was shown to be quite similar with the DIIMFP for electrons travelling from solid to vacuum $W_{in}^{s \to v}(\omega, \mu, E_0, r)$. Therefore the latter quantity can be used for the calculation of both signals I_S to a good approximation.

3.2 Monte Carlo model for the electron-induced secondary electron emission from solids

Monte Carlo simulation is a widely used approach for the solution of electron transport problems related to surface analysis. Currently, the results of MC simulation can act as a substitute for experimental data during the approbation of computational techniques. One of the greatest advantages of the MC method is the possibility to deal with the most complex boundary conditions concerning the medium where electron transport takes place, as well as the experimental geometrical arrangement [17]. From the mathematical point of view, the MC method allows evaluation of the complicated multidimensional integral of the transport equation by statistical sampling of the integrand. Assuming that the electron path consists of linear steps interrupted by scattering processes, a computer is utilized to simulate the trajectories of particles as they move inside the solid. The scattering events and the duration of particle path is determined through the use of random numbers. For electron transport, an average number of stochastically generated trajectories is used as representative for the particle flux density in the considered situation. Each individual trajectory is generated according to the physical laws governing the electron–solid interaction. This implies that the generated scattering angles and energy losses are distributed according to the physical quantities describing these scattering processes: the DECS and the DIIMFP [17].

In this work, the Monte Carlo model is presented to describe the electron-induced secondary electron emission from solids. For this purpose, it is of paramount importance to account for the true slowing down of electrons in order to describe the transport of both primary and secondary electrons in the solid. This approach accounts for the energy dependence of scattering characteristics of an electron while it slows down in the solid [17] which is highly important to describe the formation of the secondary electron cascade. In the present algorithm trajectories of individual electrons are modeled by assuming that their paths can be described by straight lines between scattering processes. The

considered scattering processes comprise elastic and inelastic interaction of electrons with the solid. The frequency of elastic and inelastic events is governed by the total mean free path given by:

$$\lambda_{tot}^{-1} = \lambda_{el}^{-1} + \lambda_{in}^{-1} \tag{3.25}$$

Elastic processes are responsible for change of the direction of motion whereas the electron energy is assumed to remain unchanged. Inelastic processes are responsible for change of the energy and the direction of motion, and creation of a secondary electron. Deflections during energy loss processes are considered by means of the binary collision model. When an electron with energy E loses energy ω in an inelastic event the scattering angle ψ_{in} due to the deflection after such a collision is given by the following equation [102]:

$$\sin \psi_{in} = \sqrt{\frac{\omega}{E}} \tag{3.26}$$

In the present model, it is assumed that each inelastic process leads to an electronic transition inside the solid from the Fermi edge to an unoccupied state since the unoccupied state is always available due to the band structure considered within a free-electron model. Provided that the final state is above the vacuum level, i.e. the energy ω lost by the primary electron exceeds the work function ϕ of the solid, an electron in the solid has been liberated with energy $E = E_F + \omega$ which can escape from the surface as a SE. Note that the bottom of the valence band is used as the energy reference for elastic scattering processes whereas the Fermi level is used as the energy reference for inelastic scattering processes. Each time a SE is created all the information about the correspondent inelastic event lead to the production of this electron is stored in the simulation stack until the current trajectory of the primary electron is terminated. Further, all SEs are simulated along the same scheme as primaries one after another. If these SEs undergo energy losses, further SEs are added to the simulation stack, giving rise to the formation of the secondary electron cascade [72].

The description of elastic scattering is based on the DECS and EMFPs calculated using the ELSEPA code [53]. Linear response theory based on empirical optical constants is used to describe inelastic scattering [42, 41]. Inelastic scattering is considered assuming both bulk and surface excitations. The model proposed by Li in Ref. [51] based on the position and direction dependent DIIMFP is used to describe surface excitations. For the sampling algorithm in the absence of surface excitations the reader is referred to Refs. [17, 36]. The procedure of sampling a scattering angle and an energy loss from the databases for the DECS and DIIMFP (prepared beforehand) is performed according to

the sampling algorithm of Coleman [103], which is also described in Refs. [40, 72]. The determination of the type of event happening during the electron transport in the solid involves the use of the following quantities: the inverse elastic mean free path λ_{el}^{-1}, the inverse inelastic mean free path λ_{in}^{-1}, which consists of those for surface scattering λ_{inS}^{-1} and for bulk scattering λ_{inB}^{-1}.

The core of the MC algorithm reads:

1. Initialize the trajectory at the origin of the coordinate system which is located at the surface with direction pointing towards the inside of the solid and with the primary energy E_0.

2. Track the electron trajectory using the following steps:

   If the electron travels in vacuum ($z \in [-20 : 0]$ Å, only surface scattering is possible):

   (a) Find the minimum mean free path λ_{min} among those between surface scattering events (for all E, z, θ, where z is the depth).

   (b) Sample a step $s = -\lambda_{min} ln (\xi)$ along the current direction, where ξ is a random number.

   (c) Determine the type of the event:

   - no interaction with probability $\lambda_{min}^{-1} / \left(\lambda_{min}^{-1} + \lambda_{inS}^{-1} \right)$. As the minimum step is used one needs to check whether an interaction takes place at all.

   - surface excitation with probability $\lambda_{inS}^{-1} / \left(\lambda_{min}^{-1} + \lambda_{inS}^{-1} \right)$ with subsequent sample of an energy loss ω from the database for the current electron energy E, depth z and direction of motion θ, and subsequent calculation of a deflection during the inelastic process according to Eq. 3.26. Provided that $\omega > \phi$ a trajectory for the secondary electron produced as a result of the inelastic event with primary energy $E = \omega + E_F$ is added to the simulation stack. The position of the SE is set to the symmetrized position inside the solid.

   If the electron travels inside the solid ($z > 0$):

   (a) Calculate the total mean free path $\lambda_{tot}^{-1} = \lambda_{el}^{-1} + \lambda_{in}^{-1}$.

   (b) Sample a step $s = -\lambda_{tot} ln (\xi)$ along the current direction.

   (c) Determine the type of the event:

- elastic interaction with probability $\lambda_{el}^{-1}/\left(\lambda_{el}^{-1} + \lambda_{in}^{-1}\right)$ with subsequent update of the electron direction of motion.

- inelastic interaction with probability $\lambda_{in}^{-1}/\left(\lambda_{el}^{-1} + \lambda_{in}^{-1}\right)$ with subsequent sample an energy loss ω from the database for the current E.

  Determine the type of the inelastic interaction if the electron is in the surface scattering region ($z \in [0:20]\,\text{Å}$):

  - surface excitation with probability $\lambda_{inS}^{-1}/\left(\lambda_{inB}^{-1} + \lambda_{inS}^{-1}\right)$ with subsequent sampling of an energy loss ω from the database for the current electron energy E, depth z and direction of motion θ, and subsequent calculation of a deflection during the inelastic process according to Eq. 3.26.

  - bulk excitation with probability $\lambda_{inB}^{-1}/\left(\lambda_{inB}^{-1} + \lambda_{inS}^{-1}\right)$ with subsequent sampling an energy loss ω from the database for the current electron energy E, and subsequent calculation of a deflection during the inelastic process according to Eq. 3.26.

  Provided that $\omega > \phi$ a trajectory for the secondary electron produced as a result of the inelastic event with primary energy $E = \omega + E_F$ is added to the simulation stack.

3. If the electron crosses the solid surface when travelling from vacuum to solid ($z = 0$, $\cos\theta > 0$) its trajectory is refracted according to Eq. 2.29 and its energy is increased by the value of the work function ϕ.

   If the electron crosses the solid surface when travelling from solid to vacuum ($z = 0$, $\cos\theta < 0$) within the escape cone defined by Eq. 2.35, i.e. provided that $E\cos^2\theta$ exceeds the value of the inner potential U_i, its trajectory is refracted according to Eq. 2.30 and its energy is decreased by the value of the work function ϕ. Otherwise, the electron trajectory is reflected back into the solid (total internal reflection) and is sampled further by going back to step 2.

4. If the electron leaves the solid without entering the analyzer or if the electron leaves the energy window of interest, disregard the trajectory and initialize the next one starting from the trajectories for SEs collected in the simulation stack. Otherwise, sample the current trajectory further by going back to step 2.

   If the electron hits the analyzer, update the corresponding histograms of measured quantities.

3.3 Approbation of the presented approaches

In this section an experimental confirmation of the reliability of the methods presented above is performed. The comparison of results of any analytical, numerical or statistical method with experimental data is the most reliable way to confirm the validity of the used approaches. Let us first start with the reliability testing of the MC algorithm employing the slowing down energy regime.

3.3.1 The slowing down regime

In this work, the Monte Carlo approach is employed in the SD regime and used to simulate the generation of secondary electrons in solids and to predict secondary electron yields. As a reminder, the MC model within the slowing down regime accounts for the energy dependence of interaction characteristics of an electron during its slowing down in a solid. Since the secondary electron emission process involves three steps – production, transport, and escape over the surface potential barrier of secondary electrons – a lot of parameters influence the resulting SEY value, such as the elastic and inelastic mean free path, the elastic and inelastic cross sections, the work function ϕ and the inner potential U_i, etc. The implemented MC algorithm is based on widely used by many authors MC codes and described in Section 3.2. In order to test the software reliability results of the MC simulation of the reflection coefficient from several targets were compared with experimental results. Another testing of the implemented MC algorithm was performed by comparing results of the MC calculation of the average number of surface excitations with experimental data. In the following Subsubsections results of such comparisons are presented.

3.3.1.1 Reflection coefficient

The reflection coefficient η is defined as the number of electrons inelastically backreflected from the solid divided by the number of incident electrons. In fact, the quantity measured experimentally is the Total Electron Yield (TEY) σ made up by the true secondary electron yield δ and the inelastic reflection coefficient η:

$$\sigma = \delta + \eta \tag{3.27}$$

71

One of the main mechanisms for an electron to slow down in the solid is the production of true secondary electrons during the inelastic interaction with the solid state electrons. Thus there are three groups among electrons escaping from the solid: elastically reflected primary electrons, inelastically scattered (or backreflected) primary electrons, which have lost part of their energy in the solid, and true secondary electrons with low energies (below 50 eV) [104]. It is not possible to experimentally draw an exact energetic boundary between inelastically scattered primary and true secondary electrons since both fast secondaries (with energies above 50 eV) and slow primaries (with energies below 50 eV) can contribute to the resulting spectrum. Nevertheless, on the basis of some commonly accepted considerations, true secondary electrons are supposed to be those with energies below 50 eV. Those electrons with energies above 50 eV are designated as inelastically reflected primaries. One of the reasons for such a separation is a significant exceeding of the number of secondary electrons with low energies over the number of primary electrons due to the creation of the secondary electron cascade as explained in Section 1.1 (see Fig. 1.1).

The acquirement of the TEY is carried out in vacuum instruments of different configurations having such common constituents as an electron gun and a collector. A typical experimental set-up can be found in Refs. [104, 105]. The total electron yield is generally measured for perpendicular incidence of electrons as a function of the incident energy ranging up to several keV, using a hemispherical collector with a suppressor grid aimed to decrease the number of stray electrons [104]. The anode of the electron gun and the sample are at ground potential. The value of σ is acquired by applying a positive bias on the grid. A negative voltage drop (- 50 V) applied between the grid and the sample prevents electrons with energies below 50 eV from reaching the collector and is used for measuring η. Then, the SEY δ is obtained as follows:

$$\delta = \sigma - \eta \tag{3.28}$$

where the reflection coefficient η contains electrons backreflected from the solid surface with energies above 50 eV including elastically reflected electrons. As it was mentioned above it is not possible experimentally distinguish between primary and secondary electrons, whereas in the MC simulation primary and secondary electrons can be traced separately. Therefore in order to predict the reflection coefficient as close as possible to the experiment in the MC calculation, updating of correspondent histograms for this quantity is done when both primary and secondary electrons with energies above 50 eV hit the detector. The results of the calculation of the reflection coefficient η by means of
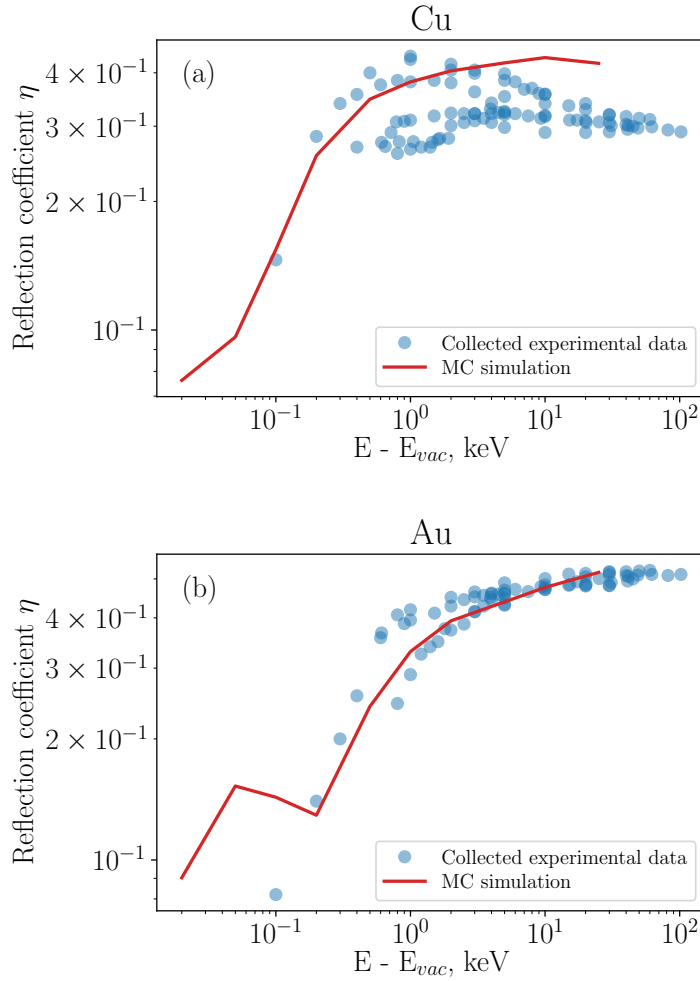
Figure 3.6: Comparison of results of the MC simulation for the reflection coefficient η as a function of the incident energy with collected experimental data [39, 104] for (a) Cu, and (b) Au.

the MC simulation are shown in Fig. 3.6 for Cu and Au compared with experimental data from Refs. [39, 104]. As seen from Fig. 3.6 the results of the MC simulation describe the experimental data with a sufficient accuracy. This example provides a good test for the developed MC code described in detail in Section 3.2.

3.3.1.2   Inclusion of surface excitations

Super-surface electron scattering, i.e., electron energy losses and associated deflections in vacuum above the surface of a medium, is shown to contribute significantly to electron

73

spectra [52]. For the super–surface scattering process, the momentum transfer during inelastic collisions plays an essential role [102] and can be taken into account by means of the binary collision model (see Eq. 3.26). Fig. 3.7 illustrates the super-surface scattering process for 500 eV electrons backscattered from a gold surface [52] showing (a) the situation without deflection, (b) a finite super-surface scattering with a deflection angle ψ_{in} before elastic backscattering, and (c) after elastic backscattering. As illustrated in Fig. 3.7(b), an electron during its approaching to the surface may suffer a super-surface energy loss transferring a small amount of momentum, which gives rise to a deflection over the scattering angle ψ_{in}. After such a super-surface energy loss process, the scattering angle during the subsequent elastic interaction then corresponds for the strong deflection over the scattering angle ψ' since it is no longer at the minimum of the DECS [52]. Therefore the reflection probability increases significantly when the incoming electron experiences a deflection in a super-surface collision. The opposite effect can take place when an electron is scattered out of a maximum in the DECS in the course of a super-surface collision (Fig. 3.7(c)).

The authors of Ref. [52] have demonstrated that when deflections in inelastic scattering are taken into account, both the vacuum and medium contribution of the surface excitation probability (solid curves) exhibit strong oscillations which are anticorrelated with the oscillations observed in the elastic backscattering probability. In the present work, surface excitations were incorporated into the MC algorithm on the basis of Li's theory [51] briefly described in Subsection 2.2.2. In order to provide an independent test of the validity of this implementation the results of MC calculations of the angularly distributed average
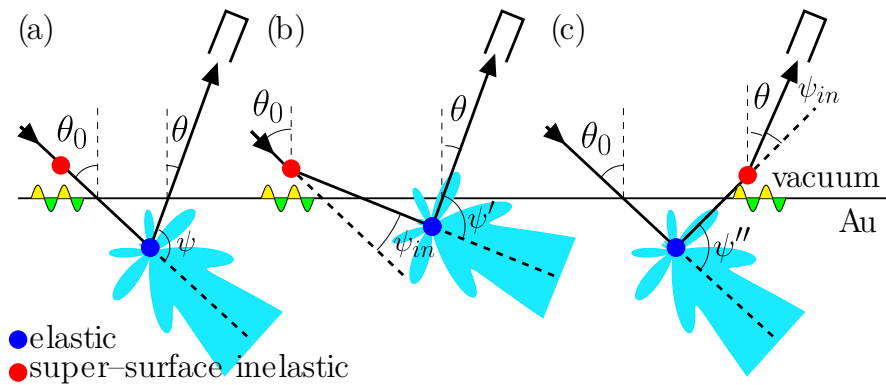

Figure 3.7: Super-surface scattering processes: (a) without deflections during surface excitations; surface excitation before (b) and after (c) back scattering with correspondent deflections ψ_{in}. Adapted from Ref. [52].
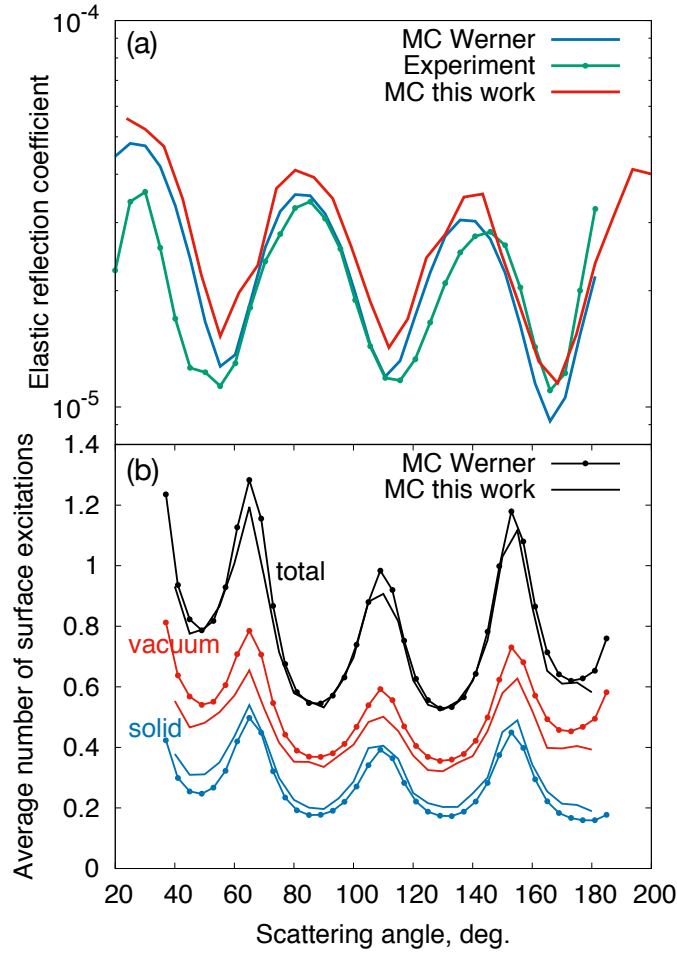
Figure 3.8: (a) Solid curves: results of Monte Carlo calculations obtained in this work (red) and the ones from Ref. [52] (blue). Data points with solid curves: measured elastic peak intensity normalised to theory at a scattering angle of $80°$; (b) Solid curves: results of the Monte Carlo calculations of the average number of surface excitations performed with deflections during inelastic scattering (this work). Solid curves with data points: results of Monte Carlo calculations taken from Ref. [52]. Lower curves (blue): surface excitations taking place inside the medium; Middle curves (red): surface excitations in vacuum; Upper curves (black): surface excitations in vacuum and medium (total); Note that this comparison is in absolute units.

number of surface excitations taken from Ref. [52] were used. Fig. 3.8(a) compares the angular distribution of the elastic reflection coefficient calculated on the basis of the MC model presented in this work and results of MC calculations obtained by the authors of Ref. [52]. The experimental results are also shown. The present results for the surface excitations, shown as solid curves in Fig. 3.8(b), are compared with results from Ref. [52], shown as data points with solid curves. The latter comparison is performed for the situation when surface excitations take place inside the medium (blue curves), in vacuum

(red curves), and both inside the medium and in vacuum (black curves). The agreement between the present MC calculations and the ones taken from Ref. [52] allows to conclude that the implementation of surface scattering effects in the present MC code is correct.

3.3.2 The quasi-elastic limit

For the approbation of the IIM approach the results provided by this method are compared with results of the MC simulation. An example of application of the MC algorithm and the IIM method is shown in Figs. 3.9-3.12. Fig. 3.9 shows the angular distribution of the elastic peak intensity (zero-order partial intensity) for 500 eV electrons incident on a gold sample at the angle $\theta_0 = 70°$ with respect to the surface normal. The experimental data are taken from Ref. [52]. For comparison, the results of the Small-Angle Approximation (SAA) (green dash-dotted curves) and the Single Scattering Approximation (SSA) (purple dashed curves) are also shown. The SAA (green dash-dotted curve in Fig. 3.9) is based on the direct accounting for flux isotropization due to small angle scattering events
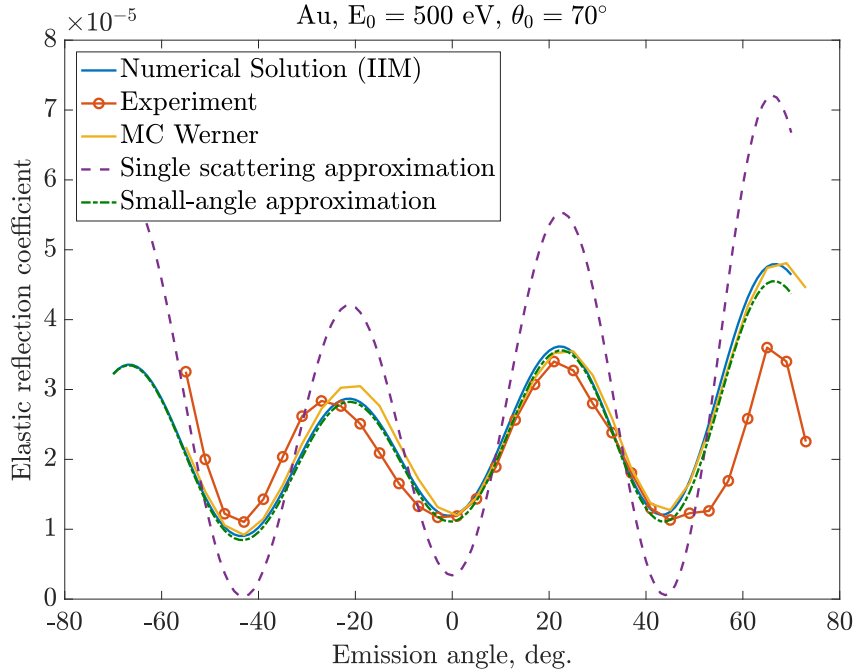

Figure 3.9: Solid curves: angular distribution of the elastic peak intensity according to the numerical solution of the non-linear equation for the reflection function within the invariant imbedding method (IIM) [36, 35] (blue), and the Monte Carlo (MC) simulation (yellow) [52]; Data points with solid curve: measured elastic peak intensity normalised to theory at an emission angle of 5° [52]; Dashed curve: the single scattering approximation; Dash-dotted curve: the small angle approximation.

[33, 35]. This approach as well as the IIM are seen to reproduce the experimental data quite well and are in close agreement with Monte Carlo model calculations (yellow solid curve). The SSA is based on the approach known as the Straight Line Approximation (SLA) introduced by Rubin and Everhart [106, 107]. This model neglects changing of the direction of motion for particles since the elastic scattering cross section has a sharp peak for forward scattering $x_{el}(\psi \approx 0°) \gg x_{el}(\psi > 90°)$. In the case of the reflection problem considered the SSA implies that electrons travel along straight lines before and after the one elastic backscattering [36]. The SSA model is seen to fail in reproducing the results of measurements and the MC simulation, demonstrating the importance of accounting for multiple elastic scattering. In Fig. 3.9 the elastic reflection coefficient is observed to exhibit several minima at emission angles of $-45°$, $0°$, and $43°$ referred to as the so-called Ramsauer-Townsend minima. This phenomenon relates to the interference of partial waves experiencing different phase shifts during their passage through the screened Coulomb field of the nuclei in the gold sample [52].

Fig. 3.10 shows the higher order (reduced) partial intensities in the reflection problem $c_n = C_n/C_0$ plotted versus the number of inelastic collisions n that electrons suffer in the solid calculated by means of the IIM and the MC approach for Cu, Ag, and Au. In the case of the IIM these quantities were calculated using the numerical solution of of the non-linear equation for the reflection function within the IIM [36, 35]. For the emission angle $\theta = 60°$ a slight difference between the two approaches is observed for Cu (Fig. 3.10a). Whereas reasonable agreement is seen for other emission angles ($\theta = 0°$ and $\theta = 30°$) presented in Fig. 3.10. Consider as a representative example the partial intensities for Au. For emission angles of $0°$ and $60°$ a monotonic decrease in the reduced partial intensities with increasing n is observed. For emission angle of $60°$ a maximum in the partial intensities is seen, which is attained at around $n = 3$. This behavior can be explained as follows. For those emission angles at which the DECS exhibit a minimum an electron has a higher probability for inelastic collision to happen giving rise to a higher C_n for $n > 0$. For those emission angles at which the DECS exhibit a maximum an electron can be reflected immediately at the very surface region giving rise to a higher C_n for $n = 0$.

Using the partial intensities the energy distribution can be obtained according to Eq. 3.5. Fig. 3.11 shows the results of the MC simulation and the calculation using the IIM approach for REELS spectra for Cu, Ag, and Au. Note that here only bulk scattering effects are taken into account, whereas surface excitations are not considered. For the presented materials, a reasonable agreement between the two computational approaches
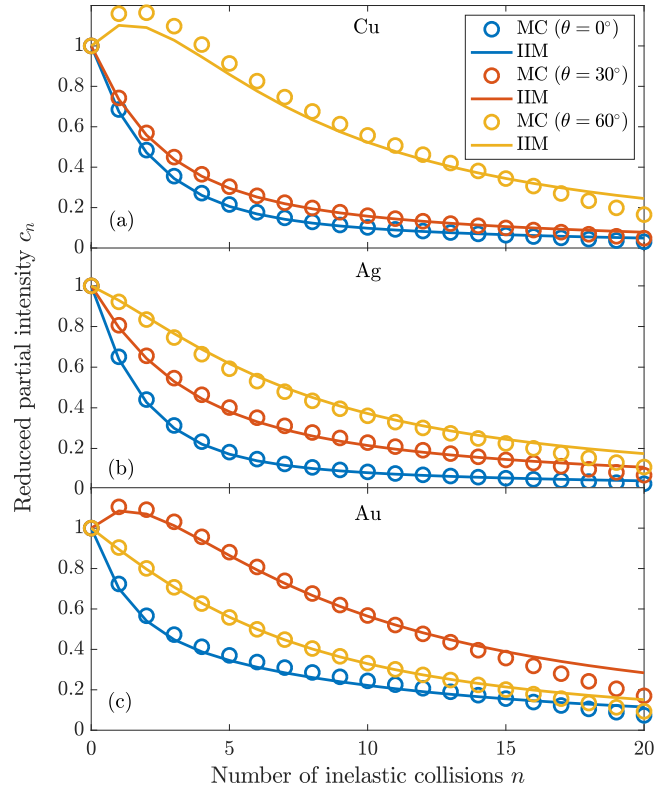
Figure 3.10: Reduced partial intensities ($c_n = C_n/C_0$) for (a) Cu, (b) Ag, and (c) Au for normal incidence of 500 eV electrons and for three angles of emission as indicated. Circles: Monte Carlo (MC) simulation results; solid curves: the invariant imbedding method (IIM).

is observed.

Fig. 3.12 shows the results of the comparison of REELS spectra with account for surface excitations calculated using the MC simulation and the IIM approach for Cu, Ag, and Au. For the presented materials the agreement between the two computational approaches is seen to be satisfied. However one can notice that the inelastic background in the range of energy losses up to 40 eV is lower in the case of the IIM approach. Such a difference is caused by different ways to describe surface excitations used in the two methods. In the IIM approach, the DIIMFP averaged over depth is used assuming that electrons cross the surface only along the angle of incidence and emission. Whereas in the MC simulation the electron movement is traced step by step, using the DIIMFP for the current position, angle, and energy at each inelastic event in the surface region. Note also that in Fig. 3.12 the case of normal incidence is considered. In the case of glancing incident or emission angles, the difference between the two approaches is getting larger
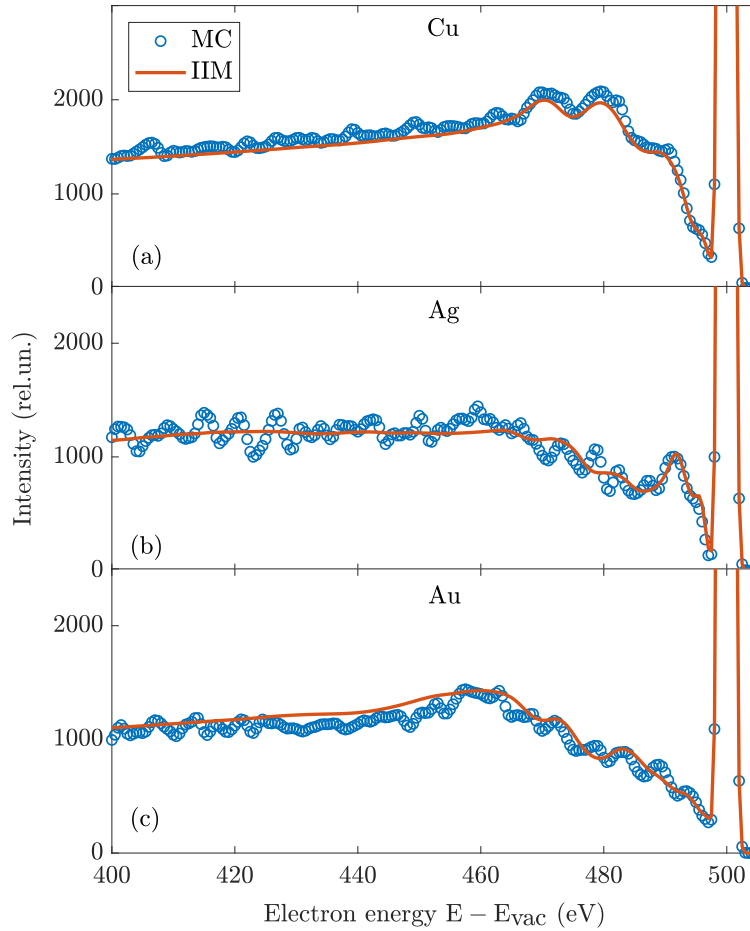
Figure 3.11: Reflection electron energy loss spectra for (a) Cu; (b) Ag; and (c) Au for normal incidence of 500 eV electrons and for the emission angle of $\theta = 60°$. Blue curves: results of the Monte Carlo simulation (MC). Red curves: results of analytic calculations on the basis of the invariant imbedding approach (IIM). Note that here the one-layered model including only bulk scattering is considered.

(this case is not shown). This is mainly due to the fact that for glancing geometries surface effects have a stronger contribution to the electron spectrum and therefore should be considered more accurately as it is done in the MC approach.
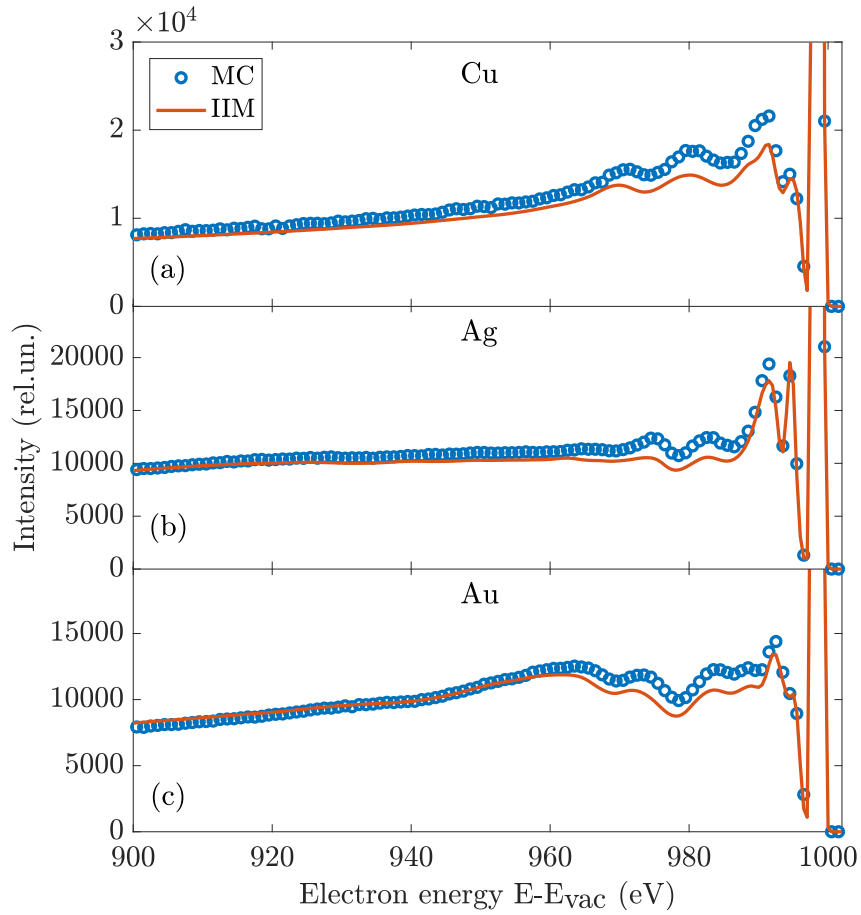
Figure 3.12: Reflection electron energy loss spectra with account for surface excitations for (a) Cu; (b) Ag; and (c) Au for normal incidence of 1000 eV electrons and emission into the entire hemisphere above the sample. Blue curves: results of the Monte Carlo simulation (MC). Red curves: results of analytical calculations on the basis of the invariant imbedding approach (IIM).

Chapter 4

Applications of the IIM for surface analysis

4.1 Retrieval of the DIIMFP from REELS and XPS using the IIM

Employing the EELS technique is a widely used approach to measure dielectric properties of a target in terms of the ELF [26, 37, 29]. In EELS experiments a wide range of energy losses is accessible which is a great advantage compared to measurements using photons as probing particles (see Subsection 2.2.1). Usually the technique called Transmission Electron Energy Loss Spectroscopy (TEELS) is employed for the measurement of the ELF in a transmission electron microscope. However, in this case, one has to use samples of different thicknesses in order to get the ELF in a wide range of energy losses for different materials. The REELS technique represents a good alternative to the TEELS technique having similar advantages but not requiring for the samples of different thicknesses. A REELS spectrum represents an overlapped contribution of n-fold scattered electrons whereas the ELF is a property of a single scattering of electrons. Therefore the retrieval of the ELF from such a signal requires an accurate description of electron transport in the solid accounting for both elastic and inelastic scattering. It is important to emphasize that inelastic scattering should be considered in terms of bulk and surface excitations. Note that in fact, the property extracted from a REELS spectrum is the DIIMFP and the DSEP. The ELF is obtained from the DIIMFP by means of the fitting procedure using a model dielectric function. One of the most reliable approaches to retrieve the DIIMFP is

deconvolution. The method proposed by Werner et al. [26] consist in the measurement of two REELS spectra in bulk and surface sensitive modes. Then the contribution of plural scattering is eliminated by means of the deconvolution procedure providing the DIIMFP and the DSEP. The use of two spectra allows (with due implementation) obtaining a unique result for these quantities.

Another approach to retrieve the DIIMFP is using direct fitting algorithms. In this case, in order to obtain the dielectric function from a REELS experiment one assumes a model function and determines the parameters for which it describes the measured spectrum best. In order to fit a spectrum, one modifies these parameters of the dielectric function and calculates the spectrum using the partial intensity approach. Then it is possible to estimate its quality by comparison of the calculated energy loss spectrum with the experimental one. The value of the DIIMFP $x_{in}(\omega, E_0)$ is derived by means of the fitting procedure on the base of minimizing a functional:

$$M = \int\limits_{0}^{\omega_{max}} \left[R\left(\omega, \mu_0, \mu, \varphi\right) - R_{exp}\left(\omega, \mu_0, \mu, \varphi\right) \right]^2 d\omega \qquad (4.1)$$

Such an algorithm requires multiple calculations of an energy loss spectrum, which implies that the method used for this purpose to be not time-consuming. The invariant imbedding method is therefore considered to be a perfect candidate for this goal. The fitting procedure employs the following steps for the calculation of energy loss spectra by means of the numerical solution of the nonlinear equation for the reflection function obtained within the IIM:

1. Setting initial oscillator parameters for a model ELF.

2. Calculation of the DIIMFP $x_{in}(\omega, E_0)$ using Eq. 2.5 for a considered primary energy E_0 for which the energy loss spectrum to be calculated.

3. Computation of partial intensities R_n by means of the numerical solution of the non-linear AC equation for the reflection function [36, 37].

4. Calculation of the energy loss distribution employing the PIA within the QE approximation:

$$R\left(\omega, \mu_0, \mu, \varphi\right) = \sum_{n=0}^{\infty} R_n\left(\mu_0, \mu, \varphi\right) L_n\left(\omega\right) \qquad (4.2)$$

5. Comparison of the obtained energy loss spectrum with experimental results. Those

oscillator parameters that give the minimum value of M in Eq. 4.1 are considered to be the resulting ones.

The above procedure allows one to retrieve the DIIMFP even from composite materials of a complicated structure for which optical data might be not available. Note that the retrieval of the DIIMFP is possible to perform by using not only the REELS technique but also the XPS technique. Let us first consider a representative example of the DIIMFP extraction from XPS spectra for graphene oxide samples annealed in a wide range of temperatures. Furthermore it, an interpretation procedure of EPES and REELS signals from the samples containing hydrogen isotopes will be also discussed after that. This procedure is considered for the interpretation of deuterium in Be-D samples with different fluence of D-ions.

4.1.1 Investigation of the structural evolution of graphene oxide during thermal reduction

Graphene has unique chemical and physical properties which opens great opportunities for its utilization in electronics, electrochemistry, solar energetics and other fields of science and engineering. Graphene Oxide (GO) is known as a precursor for the cost-effective and mass production of graphene-based materials [108]. The thermal reduction of GO is one of the most perspective methods of the production of graphene [109, 110, 111, 112, 113]. Investigation of physical and chemical changes occurring in GO samples during the annealing process at different temperatures is high of interest. This problem was studied by different authors using different measurement techniques. In Ref. [114] Hall measurements were used to define the conductivity of graphene-like samples obtained from GO at different heating temperatures. Authors of Ref. [111, 112] used the X-Ray diffraction analysis to study thermal recovery dynamics. Combination of diffraction scanning calorimetry, thermogravimetric analysis, mass-spectroscopy and XPS allowed authors of Ref. [110] to determine thermodynamic properties of thermal recovery of GO and define the evaporating gas compounds. The gas compounds were also studied in Ref. [115] by mass-spectrometry and infrared spectrometry. The authors of Ref. [116] have studied the evolution of the chemical composition of GO samples experienced by the thermal treatment using the XPS method and determined the structural changes in multi-layered GO utilizing X-ray diffraction analysis. In this work, the structural evolution of GO samples during the annealing in a wide temperature range of $T = 20 - 1000°C$ was studied by means of XPS.

4.1.1.1 Preparation of GO samples

GO samples were prepared in the National Research University "Moscow Power Engineering Institute" in Russia employing a widely used Hummers method [117]. The standard synthesis procedure has resulted in the production of a paper-like multi-layered GO film with the thickness of 40 – 60 µm. The film was cut into 11 peaces of about 30×15 mm in size, which then were subjected to the thermal treatment at different temperatures. The heat treatment of the samples was performed in the high-temperature oven setup Planar GROW-2S, designed for the growth of carbon nanotubes by Chemical Vapor Deposition (CVD). The samples were placed into the oven in a quartz container with dimensions of 20×3×2.5 cm (length, width, height). The annealing process of the samples was performed in a slow argon flow (50 cm^3/min) with the pressure up to 10 Torr. Only the slow heating process leads to the stable reproducible results as it was shown by the experiments. For example, if the heating temperature is about 1°C/sec uncontrolled "explosion" damage occurs to the sample. The annealing temperatures used are 20, 100, 150, 160, 170, 200, 300, 400, 600, 800, and 1000°C. The duration of the thermal treatment was 10 minutes for all temperatures.

4.1.1.2 Conductivity and density measurements

The current-voltage characteristics of the samples annealed at different temperatures were measured by means of a standard apparatus. A sample was clamped between contacts of the measurement device by means of copper foil crampons providing a homogeneous flow of electric current through the sample. The density of the samples treated at different temperatures was measured by the use of the balance Sartorius QUINTIX124. Therewith the size of the samples was measured by means of a micrometer. The measurements indicate the spread in the thickness of the samples of about 20%. Since this parameter is used at determination of the conductivity of the samples, this non-homogeneity is the main source of the measurement error.

4.1.1.3 Measurement of XPS spectra

XPS spectra for the eleven reduced graphene oxide (rGO) samples were measured on the Kratos Axis Ultra DLD experimental setup in Moscow State University in Russia. The pass energy for survey energy spectra was set on $E_p = 160$ eV, for short energy range of approximately 100 eV near the C 1s peak – $E_p = 40$ eV. Four samples were being placed

in the measurement plate simultaneously. The Al Kα anode monochromatic X-Ray source was used for the measurements. Measurements of the samples which suffered heat treatment at 100°C were performed with neutralizer because of a charging. The samples annealed at higher temperatures had enough conductivity not to cause the charging effect, therefore no neutralizer was needed. The acquired experimental XPS spectra for the eleven GO samples annealed at different temperatures are shown in Fig. 4.1. In Fig. 4.1 the XPS spectra are split into three groups according to observed similarities. Fig. 4.1A shows the XPS spectra for GO samples annealed in the temperature range of $T = 20 - 170$°C, Fig. 4.1B shows the XPS spectra for GO samples annealed in the temperature range of $T = 200 - 400$°C, and Fig. 4.1C shows the XPS spectra for GO samples annealed in the temperature range of $T = 600 - 1000$°C. In Fig. 4.1A the elastic C 1s peak (positioned at 0 eV energy loss) is observed to be accompanied by a peak of similar intensity shifted to higher energy losses (or to higher binding energies) and referred to as chemical shift which is a manifestation of the oxidation in the sample, which is the reason why the π plasmon peak (usually positioned at energy loss of $6 - 7$ eV) is not present in the spectra. In Fig. 4.1A the amount of the oxidation is seen to decrease with the annealing temperature increasing, and in Fig. 4.1B it becomes barely noticeable whereas the π plasmon peak becomes observable at ~ 6.5 eV in the spectra related to the GO samples annealed at temperatures above 300°C. In Fig. 4.1C the presence of any oxidation at the XPS spectra is not observed anymore. The discussed observations clearly demonstrate the relation of the π plasmon peak to the conductivity of the sample. In order to investigate this phenomenon in more detail, it is necessary first to retrieve the information on the single scattering properties or the DIIMFP for all 11 samples. This allows one to determine the evolution of the intensity of the π plasmon peak with the annealing temperature. Then the results of measurements of the conductivity for the eleven rGO samples can be compared with the temperature dependence of the intensity of the π plasmon peak.

4.1.1.4 Retrieval of the DIIMFP using the acquired XPS spectra

In the following, a description is provided for the procedure employed for fitting the acquired XPS spectra via modelling of the ELF as described in Section 4.1. The description of the XPS signal is based on the boundary problem solution for the transport equation (Eq. 3.1) using the IIM approach described in Section 3.1. The XPS spectrum
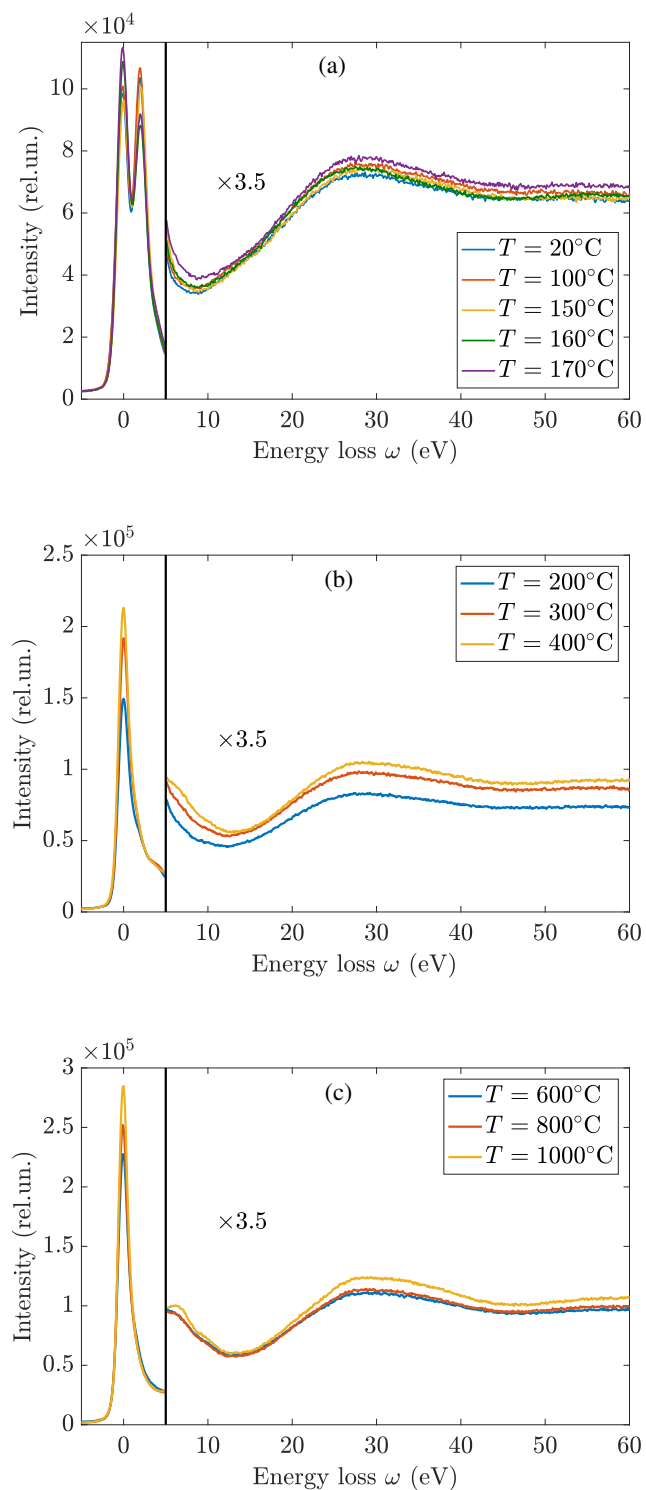
85

Figure 4.1: Experimental XPS spectra of rGO for three groups of annealing temperatures. $\omega = E_b - E_b^{C\,1s}$

$Q\left(\omega, \mu_0, \mu, \varphi\right)$ in the PIA is represented as follows:

$$Q\left(\omega, \mu_0, \mu, \varphi\right) = \sum_{n=0}^{\infty} Q_n\left(\mu_0, \mu, \varphi\right) L_n\left(\omega\right) \quad (4.3)$$

The partial intensities Q_n are found from the numerical solution of the system of the non-linear AC equations for the reflection and the photo-emission functions obtained within the IIM, which is described in detail in Refs. [36, 35].

It is well known that reduced graphene oxide contains a wide variety of oxygen groups attached to carbon [118]. The C 1s region at the XPS spectra (see Fig. 4.1) is dominated by four signals. The signal positioned at 0 eV energy loss (related to the kinetic energy $E = 1198.6\,\text{eV}$ and the binding energy $E_b = 284.6\,\text{eV}$) originates from carbon (C-C). The signal shifted by ~ 2 eV from C-C peak to higher energy losses (higher binding energies) originates from carbon in epoxide (C-O) functional groups. The third peak shifted by $\sim 3\,\text{eV}$ to higher binding energies is attributed to carbonyl groups (C=O). The fourth peak shifted by $\sim 4\,\text{eV}$ originates from carbon in carboxyl groups (O=C-OH). Epoxide, located on the basal plane of rGO, is the major component; carbonyl and carboxyl, distributed at the edges of rGO, are minor [119]. Therefore the summary energy spectrum of the C 1s region for the rGO can be described as the sum of contributions of the four identified components:

$$Q\left(\omega, \mu_0, \mu, \varphi\right) = Q^{C-C}\left(\omega, \mu_0, \mu, \varphi\right) + Q^{C-O}\left(\omega, \mu_0, \mu, \varphi\right) + \\ + Q^{C=O}\left(\omega, \mu_0, \mu, \varphi\right) + Q^{O=C-OH}\left(\omega, \mu_0, \mu, \varphi\right) \quad (4.4)$$

Each of these four components is represented within the PIA according to Eq. 4.3. The coefficients Q_0^{C-C}, Q_0^{C-O}, $Q_0^{C=O}$ and $Q_0^{O=C-OH}$ are identified with the intensities of elastic peaks and correspond to photo-electron emission from C-C, C-O, C=O, and O=C-OH each having different chemical shifts.

To take into account the instrumental function of the energy analyzer and the Doppler broadening of peaks, which depends on experimental parameters, the energy distribution of photoelectrons $Q\left(\omega, \mu_0, \mu, \varphi\right)$ is convoluted with the Gaussian function defined as follows:

$$Q_G\left(\omega, \mu_0, \mu, \varphi\right) = \int_0^\omega Q\left(\omega - \varepsilon, \mu_0, \mu, \varphi\right) G\left(\varepsilon\right) d\varepsilon \quad (4.5)$$

$$G\left(\varepsilon\right) = \frac{1}{\sqrt{2\pi}\sigma_g} \exp\left(-\frac{\varepsilon^2}{2\sigma_g^2}\right)$$

It is also necessary to consider effects that lead to the asymmetric form of the photoelectron line which can be performed using the standard Doniach-Sunjic (DS) line shape [120]:

$$Q_{DS}\left(\omega, \mu_0, \mu, \varphi\right) = \int_0^\omega Q_G\left(\omega - \varepsilon, \mu_0, \mu, \varphi\right) Y\left(\varepsilon\right) d\varepsilon \qquad (4.6)$$

$$Y\left(\varepsilon\right) = \frac{\Gamma\left(1-\alpha\right)}{\left(\varepsilon^2 + \gamma^2\right)^{(1-\alpha)/2}} \cos\left(\frac{\pi\alpha}{2} + \left(1-\alpha\right)\arctan\left(\frac{\varepsilon}{\gamma}\right)\right)$$

where $\Gamma\left(x\right)$ is the gamma function, α is the asymmetric parameter, γ is the full width at the half height. Thus we have three parameters σ, α, and γ to describe the elastic peak shape in the XPS spectrum.

To describe inelastic scattering the ELF was computed as a sum of Drude-Lindhard oscillators with parameters A_i, ω_i, and γ_i. Then the correspondent DIIMFP was calculated using Eq. 2.5. Note that the one-layered model was used, i.e. surface excitations were not taken into account. Thus, the parameters used in the fitting procedure on the base of minimizing a functional:

$$M = \int_0^{\omega_{max}} \left[Q_{DS}\left(\omega, \mu_0, \mu, \varphi\right) - Q_{exp}\left(\omega, \mu_0, \mu, \varphi\right)\right]^2 d\omega \qquad (4.7)$$

Therefore such a minimisation procedure implies varying of the following parameters: σ_g, α, γ, zero partial intensities Q_0^{C-C}, Q_0^{C-O}, $Q_0^{C=O}$, and $Q_0^{O=C-OH}$ (each with the correspondent energy position in the spectrum) for elastic peaks, a set of oscillators with A_i, ω_i, and γ_i for the ELF. The fitting parameters vary until the minimum of the functional M in Eq. 4.7 has been reached.

4.1.1.5   Analysis of the obtained results

Figs. 4.2, 4.3 show representative examples of fits of the calculated XPS spectra to the experimental data for the GO samples annealed at T = 160°, where no π-plasmon peak is observed, and at T = 800°, where it is clearly seen. The resulting normalized DIIMFPs (NDIIMFPs) extracted from the XPS spectra for several annealing temperatures are depicted in Fig. 4.4. Here the evolution of the π-plasmon peak (at ~ 6.5 eV) is clearly
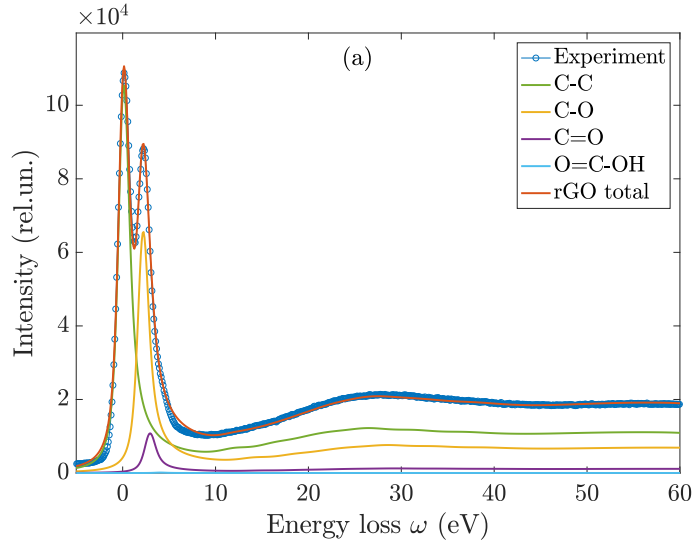
Figure 4.2: The resulting fit to the experimental XPS spectrum of the GO sample annealed at T $= 160°$.

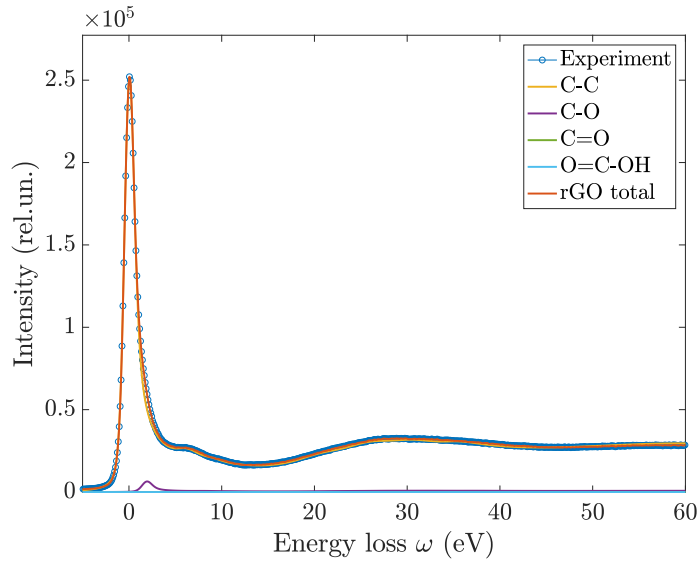**Figure 4.3:** The resulting fit to the experimental XPS spectrum of the GO sample annealed at T $= 800°$.

observed with the annealing temperature increasing starting from T $= 200°$. Whereas no changes in the intensity of $(\pi + \sigma)$ plasmon (at ~ 26 eV) are seen.

Fig. 4.5 shows the comparison of the evolution of the intensity of the π plasmon peak and the conductivity of the samples with the increasing annealing temperature. The most significant changes in these quantities are observed to occur in the temperature range
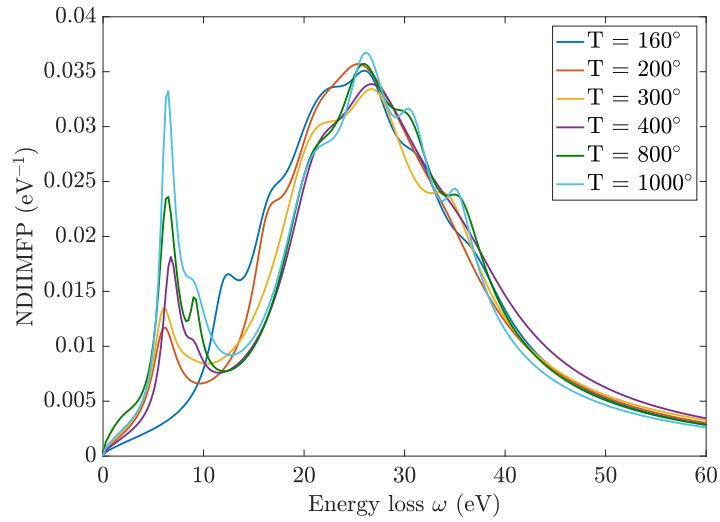
Figure 4.4: Evolution of the NDIIMFP of GO samples annealed at different temperatures.
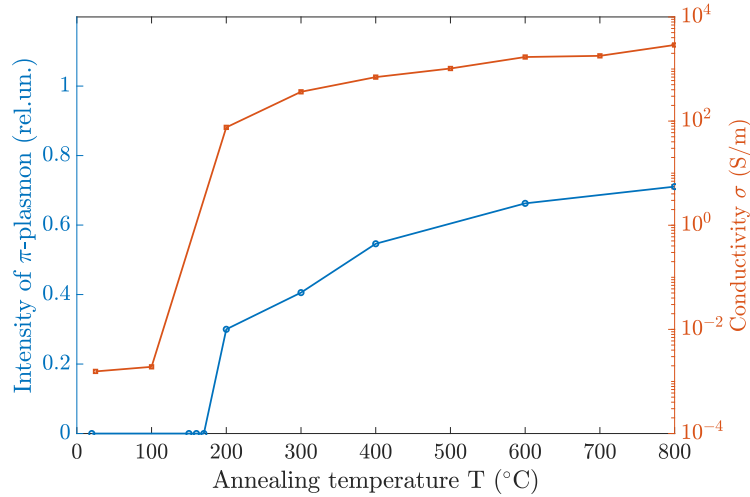

Figure 4.5: Dependency of π plasmon excitation probability and conductivity of rGO samples on the annealing temperature. The intensity of the π plasmon is normalised to those at T = 1000°.

of $100 - 200°$C. The intensity of π plasmon rapidly increases at about $200°$C and then only a slight increasing of its intensity is observed. The conductivity in this temperature range changes by five orders of magnitude from 10^{-3} up to approximately 100 S/m. The consequent heating of the material results in a considerably smoother increasing of the conductivity. The maximum value of the conductivity reached is $\smile$ 3500 S/m, which is about one order of magnitude lower than the reference value of the conductivity
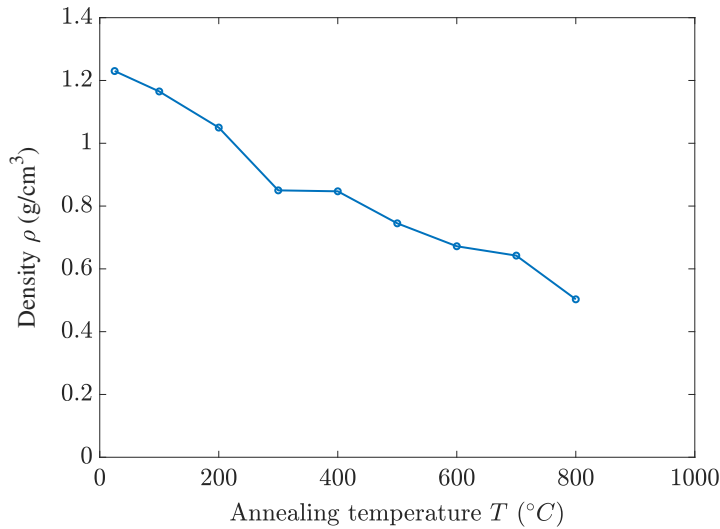
Figure 4.6: Dependence of the density of rGO samples on the annealing temperature.

of natural graphite [121]. Such a rapid increase in the conductivity indicates that the percolation mechanism is responsible for the transition of the material from insulating to conducting state [122, 123]. The percolation transition occurs due to the formation of one or several conducting channels formed by the chains of adjacent conducting fragments of reduced GO. Further annealing results in a smoother increasing of the conductivity through the formation of a larger number of conducting fragments in rGO and, therefore, a larger number of conducting channels. A detailed description of this process can be found in Ref. [123].

The reduction process of GO is also accompanied by a decrease in the density of the material. Fig. 4.6 presents the dependence of the density of the GO samples on the annealing temperature. The density measurements indicate that the thermal treatment does not change the thickness of the samples so that the observed changes in the density of the material due to annealing are caused by the removal of oxygen and other elements engaged into the structure of graphene oxide. Therefore the removal of oxygen makes the GO samples more brittle. As is seen from Fig. 4.6, heating the samples up to 800°C results in a decrease of their density by about 2.4 times, from 1.2 to 0.5 g/cm^3. The density of graphite is about 2.2 g/cm^3, which exceeds the one for the GO sample annealed at $T = 800$°C by about 4-5 times. Therefore the average distance between the graphene sheets in the GO sample annealed at 800°C is $4 - 5$ times larger than that in graphite. This fact allows to expect that the inter-layer interaction in the reduced graphene oxide

is negligible.

4.1.1.6 Summary

The proposed framework on the calculation of XPS spectra allows to describe not only zero-loss peaks but also complete XPS spectra including the inelastic background. Using the calculation routine of the framework the reconstructed DIIMFP can be used to describe EELS and XPS spectra of the samples [37]. It is shown that photoelectron spectra can provide a great amount of information about processes that take place during the annealing of the GO samples. Heat treatment of the GO samples in the temperature range of $150 - 170°C$ causes the percolation transition, at which the conductivity of the material increases by 5 orders of magnitude. The correlation between the conductivity and π plasmon intensity was demonstrated. The analysis shows that a material has been obtained has electronic properties of graphite but its density is much lower. This very interesting fact makes reduced graphene oxide a unique material which can be relevant for different technological applications.

4.1.2 Detection and analysis of hydrogen isotopes using electron spectroscopy techniques

The field of plasma-wall interaction comprises all processes involved in the exchange of mass and energy between plasma and the surrounding wall materials. Plasma facing materials experience particularly adverse conditions since they are intended to withstand intense neutron flux for a sufficient period of time, and high heat loads. Plasma facing materials must have high thermal conductivity for the efficient heat transport, high cohesive energy for low erosion by particle bombardment, and low atomic number Z to minimize plasma cooling [124]. Current fusion reactors are fueled by deuterium-tritium (D-T) fusion reactions, which produce high-energy neutrons that can damage the first wall. A divertor is a device that allows the online removal of waste material from the plasma while the reactor is still operating. The divertor is usually protected by a different material than the one used for the major area of the first wall. Presently, in the International Thermonuclear Experimental Reactor (ITER) beryllium is chosen as the plasma-facing material for the first wall and tungsten/carbon for the divertor. Carbon has traditionally been used as a plasma facing material because it has a favourable combination of low Z, high thermal conductivity and strong bonding [124]. However,

it is known to have a susceptibility to chemical sputtering by hydrogen isotopes. Any tritium that reacts with the carbon surface will redeposit elsewhere in the reactor vessel in the form of hydrocarbons, which is difficult to detect and recover. This is the reason why it is high of importance to have a technique for the precise detection of hydrogen isotopes in solids. Plasma facing components in ITER will receive most of the particle flux and/or heat loads is the tungsten divertor, while others will be composed of beryllium [125]. Hydrogen isotope retention in beryllium can play a role in the lifetime of ITER's beryllium inner walls because of erosion [126]. Several studies based on the ion irradiation of Be samples have been devoted to D behavior to ensure that tritium retention will not be a limiting issue in ITER operations [127].

Methods based on electron spectroscopy usually have problems with direct detection of hydrogen and helium [22, 128]. Nevertheless, recently several techniques have been proposed for measuring the bound hydrogen by means of electron spectroscopy [20, 21, 22, 23]. Elastic peak electron spectroscopy (EPES) is a perspective tool for this goal [129, 23, 24] used in combination with other electron spectroscopy techniques such as EELS and XPS. This technique is analogous with the Rutherford backscattering spectroscopy, but utilizes electrons instead of ions as primary projectiles [130]. Using electrons instead of ions as projectiles allows to avoid the ion damage to the sample. Thus, EPES has the same experimental conditions as the EELS method. For RBS analysis accelerators are required, which are not only huge in footprint but also come with a huge price tag. EPES and EELS only require commercially available electron sources, and an electron energy analyzer, and can be integrated into laboratory photoelectron setups. This also enables to combine common surface analysis techniques such as XPS and EELS allowing valuable, well defined in-situ measurements without exposing the sample to the air.

The EPES technique is based on the sensibility to small energy losses during elastic processes, since nucleus of atoms have different mass. This requires a high energy resolution of energy analyzers in order to resolve elastic peaks in the energy spectrum shifted due to this small energy loss. Therefore this method allows to analyze even light elements including hydrogen. Eq. 2.3 shows that the elastic energy loss is of the order of 10 eV for $E_0 = 30$ keV and decreases with decreasing primary energy. For example, for 30 keV electrons and $\psi = 45°$ the energy shift of elastic peaks of tritium, deuterium, and hydrogen is $\Delta E = 3.2, 4.8,$ and 9.6 eV, respectively. Therefore it becomes possible to resolve and then interpret the elastic peak of hydrogen in the EPES spectrum due to such a sufficient energy shift ΔE.
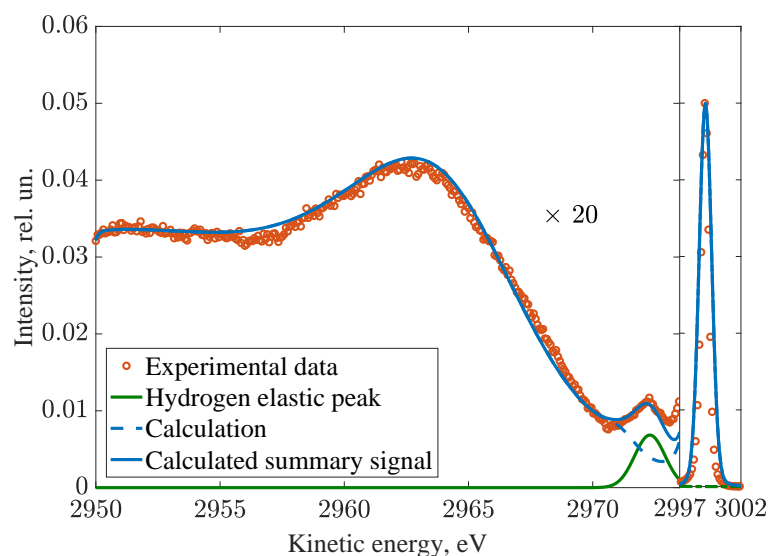
Figure 4.7: Comparison of the experimental REELS spectrum for the hydrocarbon sample (red circles) [23] with the calculated REELS spectrum using the DIIMFP retrieved from the XPS data (dashed line). The green line corresponds to the derived EPES signal after subtracting the inelastic background.

In order to interpret an elastic peak in the energy spectrum one has to determine the area under this peak, which requires the subtraction of the inelastic background from the total energy loss signal. This is known to be a very challenging task [24] since elastic peaks, formed by electrons reflected by different atoms in a solid, overlap with the inelastic signal of a dominant element in the spectrum. In Ref. [24] a hydrocarbon sample was analyzed using the joint interpretation of the REELS and XPS spectra measured for this sample. Since H 1s valence electrons are not useful in elemental identification using the XPS method [131], the resulting energy spectrum does not contain the contribution from hydrogen which allows to conveniently retrieve the DIIMFP, which then can be used for the calculation of the REELS spectrum. The result is shown in Fig. 4.7 with dashed blue curve. The subsequent comparison of the calculated (dashed blue curve in Fig. 4.7) and measured (red data points in Fig. 4.7) REELS spectra allows the interpretation of the elastic peak of hydrogen which remains unaccounted for (green curve in Fig. 4.7). The interpretation procedure is described further in the text. Note that it is important to acquire both XPS and REELS spectra in-situ for the same sample.

Another possibility to interpret the presence of hydrogen or its isotopes in a sample is by employing different geometrical arrangements. Such an approach allows obtaining

different values of the recoil energy loss due to different values of the scattering angle and therefore one can avoid the intersection of the elastic peak of hydrogen with the inelastic background of a dominating element in the energy loss spectrum. In this work, this technique is employed for the investigation of deuterium implantation into beryllium samples [25].

4.1.2.1 Investigation of deuterium implantation into beryllium samples

4.1.2.1.1 Experiment

Investigated samples were prepared and measured in the Forschungszentrum Jülich GmbH. A polished, quadratic beryllium sample with a side length of 10 mm was used as base material for the experiments. The average roughness Ra of the samples was below 0.1 μm. The samples were supplied by MaTecK and had a bulk purity of at least 99.8% Be. All experiments were conducted in a multi-chamber UHV-setup with a base pressure of 10^{-8} Pa from Prevac. The system is equipped with the hemispherical analyser (HSA) R4000 and a monochromatic Al Kα X-ray source MX 650 for XPS both from Scienta-Omicron. Two electron sources EM-802 from Staib serve as excitation sources for EELS. The angle between the first electron source and the HSA is 60° ("normal" geometry) and between the second source and the HSA 120° ("glancing" geometry). The sample is located at a 4-axis manipulator with heating capabilities up to 1370 K and can be rotated towards the electron sources. For sample cleaning and the implantation of the hydrogen isotope deuterium, a Prevac ion source IS 40E1 is used. The sample was cleaned by annealing at 900 K and sputtering with Ar+ ions with a kinetic energy of 5 keV. The cleaning steps were repeated cyclically until no surface contamination was visible in the XPS survey spectrum. There was no beryllium oxide detectable in the high resolution XPS spectrum of the Be 1s core level. Thus, the sample surface was atomically clean. After the cleaning process D-ions were implanted with an acceleration voltage of 3 kV and a fluence of $5.5 \cdot 10^{21}$ m^{-2}. After the implantation a XPS survey scan showed no contamination of the sample. No beryllium oxide was visible in the Be 1s core level spectrum. After the cleaning procedure and after the implantation, EELS spectra were recorded at three different primary electron energies E_0: 1500, 3000, and 5000 eV. Each spectrum was recorded two times: in "normal" and "glancing" geometries as shown in Fig. 4.8.

In between the recording of the EELS spectra the sample was analysed by XPS in order
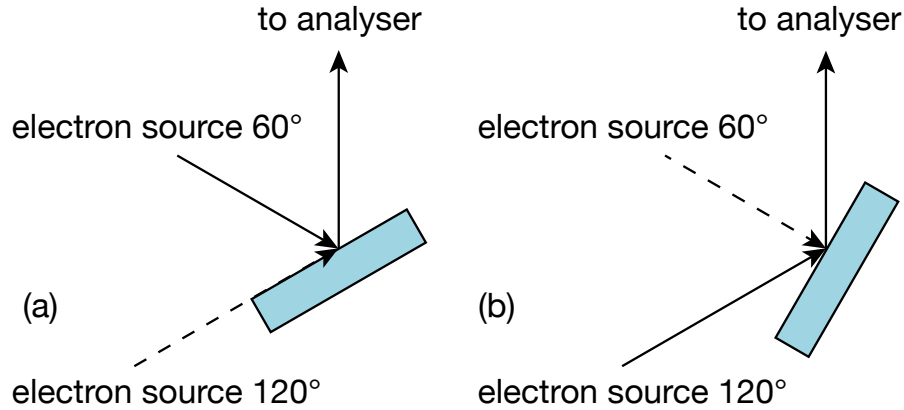
Figure 4.8: Schematic view of the sample rotation in the experimental set-up: (a) "normal" geometry: the rotation angle is 30°, the angle between the electron gun and the analyser is 60°, the scattering angle $\psi = 120°$ ($\theta_0 = 30°$, $\theta = 30°$); (b) "glancing" geometry: the rotation angle is 60°, the angle between the electron gun and the analyser is 120°, the scattering angle $\psi = 60°$ ($\theta_0 = 60°$, $\theta = 60°$). The azimuthal angle $\varphi = 0°$

to check for surface oxidation during the experiments. No BeO was detectable in the high resolution spectra of the Be 1s region. The difference in the spectra of the clean reference measurements and the measurements of the implanted sample therefore can all be assigned to the implantation of deuterium. The same procedure was performed for the implantation of the Be sample with De-ions with the fluence of $20.1 \cdot 10^{21}$ m^{-2}.

4.1.2.1.2 The interpretation procedure

The interpretation of elastic peaks in energy spectra requires knowledge of three parameters [25]:

1. The recoil energy loss characterizing the energy position of the elastic peak according to Eq. 2.3. Results of the calculation of ΔE for Be and D depending on the incident energy E_0 and the scattering angle ψ are summarized in Table 4.1.

2. The broadening of the elastic peak which can be approximated by the Gaussian distribution (Eq. 4.5) [132] with the HWHM given by:

$$\sigma = \sqrt{\sigma_D^2 + \sigma_A^2 + \sigma_E^2} \qquad (4.8)$$

where σ_D is the Doppler broadening, σ_A is the broadening due to the energy analyzer slit function, σ_E is the broadening of the electron beam. The quantities

Table 4.1: The recoil energy loss ΔE for Be and D for different incident energies E_0 and geometry arrangements.

E_0 (keV)	ψ (deg.)	ΔE_{Be} (eV)	ΔE_D (eV)	$\Delta E_D - \Delta E_{Be}$ (eV)
1.5	120	0.28	1.23	0.95
1.5	60	0.09	0.41	0.32
3	120	0.55	2.46	1.91
3	60	0.18	0.82	0.64
5	120	0.91	4.09	3.18
5	60	0.31	1.37	1.06

Table 4.2: Physical quantities describing the broadening of elastic peaks for Be samples with different D-ion fluences.

Fluence (m^{-2})	E_0 (keV)	σ (eV) Be	D	σ_{AE} (eV)	σ_D (eV) Be	D
$5.5 \cdot 10^{21}$	5	0.57^{*}	0.98	0.37	0.43	0.91
$20.1 \cdot 10^{21}$	5	0.60^{*}	1.00	0.42	0.43	0.91

* taken from the experimental data.

σ_A and σ_E are characteristics of an analytic equipment, which can be conveniently rewritten as $\sigma_{AE}^2 = \sigma_A^2 + \sigma_E^2$. In order to determine the hardware peak broadening σ_{AE} one can use the following expression:

$$\sigma_{AE}^2 = \sigma^2 - \sigma_D^2$$

with the Doppler broadening σ_D given by:

$$\sigma_D = 4E_0 \frac{v_{th}}{u}$$

$$v_{th} = \sqrt{\frac{3k_B T}{M}}$$

(4.9)

where $u = \sqrt{2E_0/m_e}$ is the electron velocity, v_{th} is the velocity of the thermal motion of atoms, k_B is the Boltzmann constant, and T is the temperature. The value of σ is obtained from the fit to the experimentally observed elastic peak of Be using the Gaussian function. Table 4.2 contains resulting values for all broadening quantities for Be samples with different D-ion fluences.

3. The electron signal intensity or the area under the peak of elastically scattered electrons which is determined by the zero-loss partial intensity $R_0\left(\omega, \mu_0, \mu, \varphi\right)$ which in the case of Be-D material is found as the sum of the zero-loss partial intensities for Be and D.

As seen from Table 4.1 the difference in the energy position between elastic peaks of Be and D in the spectra at incident energies $\simeq 1.5$ and $\simeq 3$ keV is ranging from 0.32 up to 1.91 eV. The energy resolution of the experimental set-up does not allow to resolve the elastic peak of deuterium from the elastic peak of beryllium in the energy spectra. Therefore, the concentration of deuterium atoms was determined only for the spectra measured at the incident energy of $\simeq 5$ keV where $\Delta E_D - \Delta E_{Be} = 3.18$ eV in "normal" geometry ($\psi = 120°$). The DIIMFPs were retrieved from the experimental REELS spectra of beryllium samples implanted with different fluences of deuterium ions $5.5 \cdot 10^{21}$ and $20.1 \cdot 10^{21}$ m^{-2} on the basis of the fitting algorithm described in Section 4.1. Note, that the REELS spectrum acquired in the "glancing" geometry was used to retrieve the DIIMFP since for the scattering angle $\psi = 60°$ the recoil energy loss $\Delta E = 1.37$ eV (see Table 4.1) is not enough to distinguish the elastic peak of deuterium in the spectrum. Therefore this no-loss peak is not overlapped with the inelastic background of Be which allows to perform the retrieval procedure. Then the same DIIMFP can be used for the calculation of the REELS spectrum in the "glancing" geometry since the DIIMFP does not depend on the geometry factors. Different laws for energy losses in the near-surface region and in the bulk were used in terms of the DSEP to describe surface excitations and the DIIMFP for excitations in bulk. In Fig. 4.9 results of the fitting procedure are shown for REELS spectra measured at $E_0 \simeq 5$ keV incident energy in "normal" and "glancing" geometries for the Be-D spectra with a fluence of $5.5 \cdot 10^{21}$ m^{-2}. The entire calculation procedure is described in detail in Refs. [34, 37]. The calculated REELS spectra are seen to be in a satisfactory agreement with the experimental data. Similar results were obtained for the Be-D spectra with a fluence of $20.1 \cdot 10^{21}$ m^{-2} (not shown). The value of the recoil energy loss for the scattering angle $\psi = 120°$ in "normal" geometry $\Delta E = 3.18$ eV makes the elastic peak of deuterium visible in the spectrum overlapped with the inelastic background of Be. Therefore the main purpose is now to make an accurate subtraction of this inelastic background in order to determine the area under the elastic peak of deuterium. After doing that the relative concentrations of Be and D can be calculated.

The comparison of the calculated and experimental REELS spectra for Be samples implanted by D-ions with the fluence of $5.5 \cdot 10^{21}$ and $20.1 \cdot 10^{21}$ m^{-2} acqiured in the
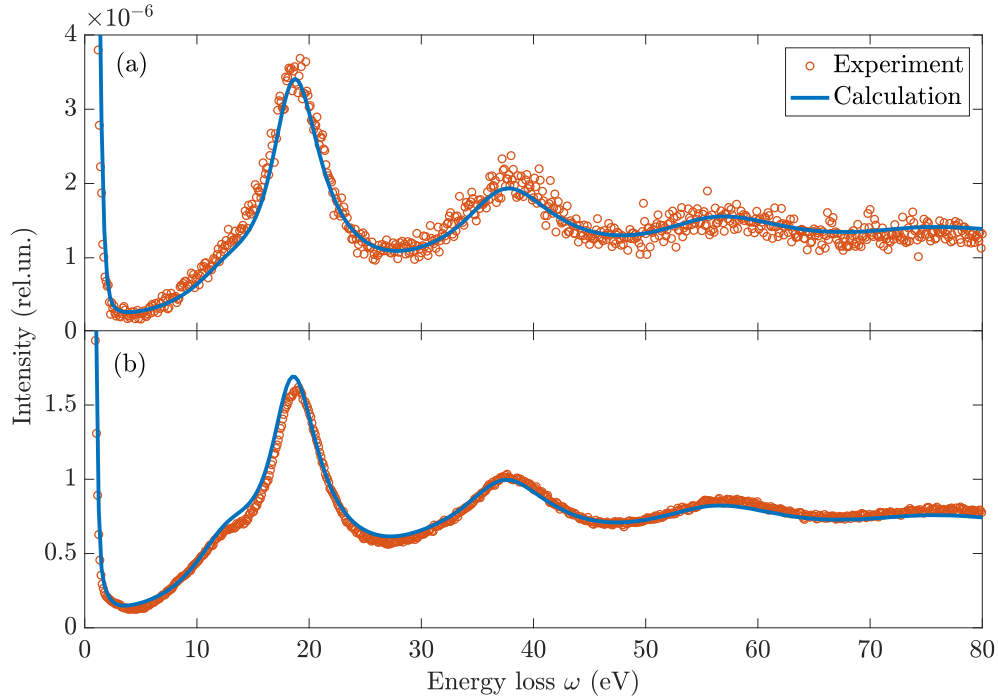
Figure 4.9: REELS spectra of the Be sample with deuterium ion fluence of $5.5 \cdot 10^{21}$ m^{-2} for $E_0 \simeq 5$ keV: a) "normal" geometry; b) "glancing" geometry.

"normal" geometry is shown in Fig. 4.10. Calculated REELS spectra without taking into account the elastic peak of deuterium are presented in Fig. 4.10 by green lines. The discrepancy between the calculation and the experiment (red circles) at the energy loss of 2-5 eV is due to the presence of the elastic peak of deuterium. In order to take it into account the elastic peak of deuterium was calculated according to Eqs. 2.3, 4.8 and the area under this peak S_D was determined (black dash-line). The result of the complete calculation with D is shown with blue lines in Fig. 4.10. Determining the area under the elastic peak of beryllium S_{Be} and using the DECS $W_{el}^{Be}(\psi)$ and $W_{el}^{D}(\psi)$, the relative concentrations can then be determined. Obtained values of the areas under elastic peaks of Be and D are summarized in Table 4.3. The composition ratio is given by:

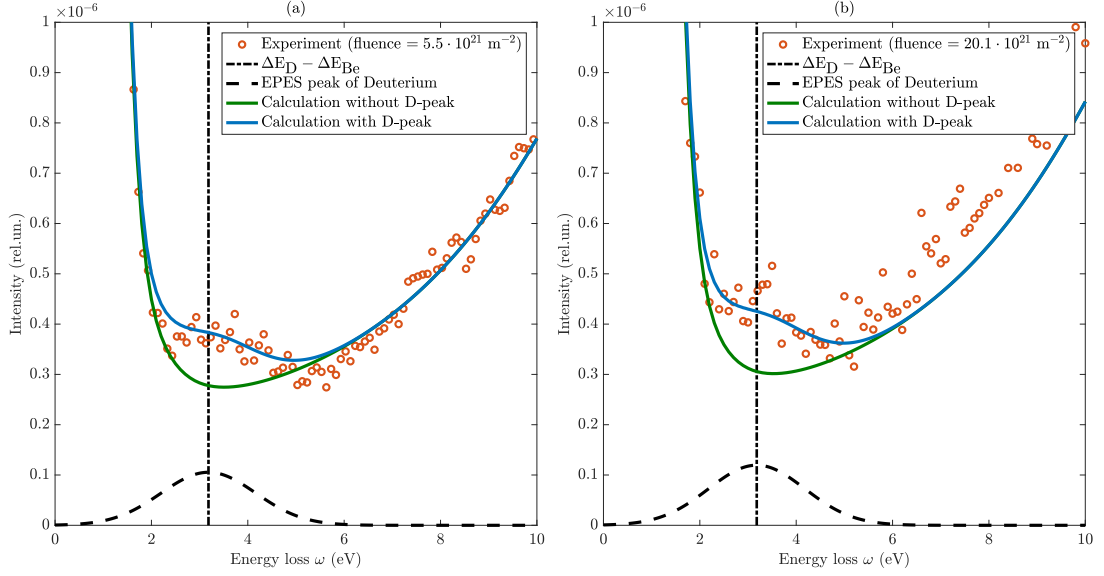$$\frac{n_D}{n_{Be}} = \frac{S_D W_{el}^{Be}(\psi)}{S_{Be} W_{el}^{D}(\psi)} \qquad (4.10)$$

99

Figure 4.10: Energy loss spectra of electrons reflected from the Be substrate with deuterium ion fluence of a) $5.5 \cdot 10^{21}$ m^{-2}, b) $20.1 \cdot 10^{21}$ m^{-2}.

Table 4.3: Results of the determination of the areas under elastic peaks of Be and D for different D-ion fluences.

Fluence (m^{-2})	S$_{Be}$	S$_D$
$5.5 \cdot 10^{21}$	$3.6 \cdot 10^{-5}$	$2.6 \cdot 10^{-7}$
$20.1 \cdot 10^{21}$	$3.4 \cdot 10^{-5}$	$3.0 \cdot 10^{-7}$

For the fluence of $5.5 \cdot 10^{21}$ m^{-2}:

$$\frac{n_D}{n_{Be}} = \frac{2.6 \cdot 10^{-7} \cdot 9.6 \cdot 10^{-7}}{3.6 \cdot 10^{-5} \cdot 5.8 \cdot 10^{-8}} = 0.12 \pm 0.03$$

For the fluence of $20.1 \cdot 10^{21}$ m^{-2}:

$$\frac{n_D}{n_{Be}} = \frac{3.0 \cdot 10^{-7} \cdot 9.6 \cdot 10^{-7}}{3.4 \cdot 10^{-5} \cdot 5.8 \cdot 10^{-8}} = 0.15 \pm 0.03$$

From these results it is followed that the concentration ratio n_D/n_{Be} in the very surface layer with thickness $d \simeq 9.2$ nm is 0.12 ± 0.03 at fluence of $5.5 \cdot 10^{21}$ m^{-2} and 0.15 ± 0.03 at fluence of $20.1 \cdot 10^{21}$ m^{-2}.

4.1.2.2 Summary

The possibility of quantitative analysis of hydrogen isotopes by means of the combination of EELS and EPES techniques was demonstrated [25]. In conclusion, the possibility of using the EPES technique for the determination of hydrogen in metals with D-concentrations down to 11% has been shown. This method has a great potential to address recent problems in material research for nuclear fusion, energy storage and fuel cells. Classical methods of surface analysis like, e.g. XPS and Auger Electron Spectroscopy, will greatly benefit if paired with the EPES and EELS techniques for hydrogen detection in-situ.

Chapter 5

Low energy (1 - 100 eV) electron inelastic mean free path (IMFP)

In the past 30 years, the determination of IMFP values at energies above 200 eV has been an active area of research and nowadays commonly accepted values are calculated using dielectric response theory, employing optical constants [28, 27]. It is important to emphasize that different approaches give a similar IMFP in this energy range and are in a good agreement with experimental results. However, different models give widely different values for the IMFP at low energies as illustrated in Fig. 1.2, which shows the IMFP for Cu according to the Penn algorithm based on the Simplified Single-Pole Approximation (SSPA) (represented by the solid red curve) [42] and the IMFP theoretically calculated using the Mermin dielectric function, which gives significantly lower values (represented by the solid green curve). Data points show experimentally measured or theoretically calculated values found in the literature [43, 42, 44, 18, 45, 46, 47, 48]. Below 100 eV it is complicated to conceive any experimental method to verify theoretical calculations. EPES technique is usually employed for the experimental determination of IMFPs [18], although, it becomes less reliable at energies below 100 eV. There is a number of other experimental techniques but all of them require measurements at low energies, which is essentially a big challenge [46]. In the present work, an approach is presented to retrieve the low energy IMFP values from measurements of Secondary Electron Yields (SEY) at high energies. An attempt of the experimental measurement of the IMFP at low energies by means of the EPES is also discussed.

5.1 Determination of the IMFP at low energies from analysis of secondary electron yields (SEY)

The SEY is the main parameter describing secondary electron emission. Since it is
impossible to experimentally distinguish between primary and secondary electrons, those
electrons in the electron energy spectrum with an energy below 50 eV are usually
designated as secondary electrons. This is based on the assumption that the number of
inelastically backreflected primaries with energies below 50 eV is low in comparison with
those in the SE cascade, which is mainly made up of low energy electrons. This is clearly
seen from Fig. 1.1 which shows the results of the Monte Carlo simulation for electron
emission from a gold surface. While some features characterising the inelastic process
can be distinguished near the peak of elastically backscattered electrons at 1000 eV, the
SE peak below ~ 50 eV is essentially featureless. The model calculations demonstrate
that secondary electrons (red curve in Fig. 1.1) with considerable kinetic energies of
the order of the elastic peak energy may be emitted from the surface, although the
majority is released with energies below ~ 50 eV. For such low energies, the contribution
of backscattered primaries (green curve in Fig. 1.1) to the total spectrum is more than
an order of magnitude smaller than the contribution of secondaries, which is the reason
why by convention electrons with energies below ~ 50 eV are designated as secondary
electrons. The physical reason for the peak at energies below ~ 50 eV is the fact that the
typical energy of the solid state electrons is of the order of 1 Hartree (27.2 eV), giving
rise to a mean energy loss in an inelastic collision of the same order of magnitude, for
arbitrary incident energies. Fig. 5.1 shows the results of the Monte Carlo simulation for
electron emission from a gold surface for incident energy $E_0 = 100$ eV. It is clearly seen
from Fig. 5.1 that for low incident energies (below ~ 100 eV) the contribution of low
energy primary electrons in the SE peak becomes more significant, although the main
contribution is still determined by secondary electrons.

Since the emission of secondary electrons for any incident energy always involves the
formation and emission of a cascade of slow electrons (< 50 eV) the SEY for arbitrary
energies depends sensitively on the inelastic mean free path (IMFP) values at low energies
(below 100 eV). This makes it possible to retrieve the information about the low energy
IMFP from the high energy SEY experiments. The SEY measurements found in the
literature are usually performed for incident energies ranging from several eV to several
keV. To theoretically describe the secondary electron emission from solids one needs
quantitative knowledge of electron scattering processes including those at energies below
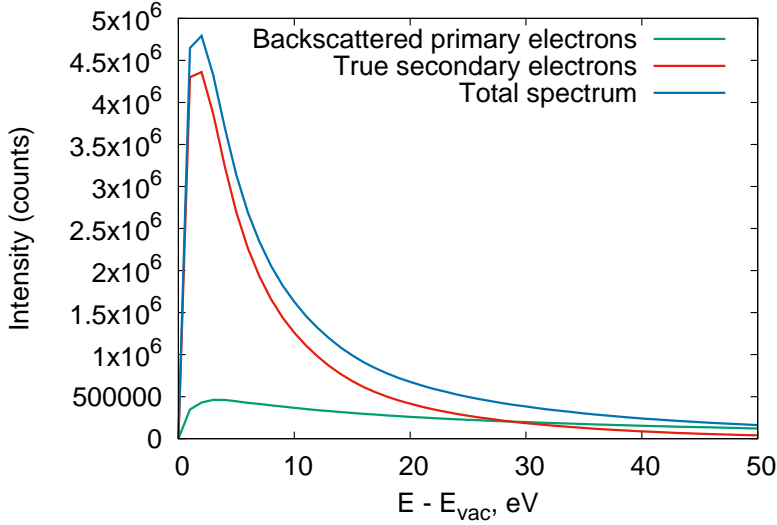
Figure 5.1: Monte Carlo simulation of secondary electrons emitted from a Au target, for a primary electron energy of $E_0 = 100$ eV for normal electron incidence and emission into the entire hemisphere above the sample. The total energy distribution (blue curve) is made up of backscattered primary electrons (green curve) and secondary electrons (red curve).

100 eV. In particular, quantitative knowledge of IMFP values at low energies are needed. Fig. 5.2A shows the IMFP for Au according to the formalism by Penn within the SSPA (represented by the dot-dashed green curve) [133] and the IMFP theoretically calculated using the Mermin dielectric function, which gives significantly lower values (represented by the dashed black curve). Further, let the Penn algorithm be defined as the one based on the SSPA. Data points show experimentally measured or theoretically calculated values found in the literature [134, 135, 136, 42, 18, 137, 47]. Note that IMFP values based on the Penn algorithm are known to be less reliable for energies below 100 eV, this approach is used in the present paper for comparison only. The Mermin dielectric function $\epsilon_M(\omega, q)$ [49] represents an improvement over the Lindhard dielectric function since it includes broadening due to the finite lifetime of excitations, which makes this model a more realistic and widely-used to calculate the IMFP [138, 139, 54].

Fig. 5.2B shows results of the MC simulation of the SEY for Au assuming the two extreme sets of IMFP data addressed above. Note that the IMFP data in Fig. 5.2A are identical for energies above 100 eV. It is clearly seen that even at high energies the SEY values depend very strongly on the IMFP values at energies below 100 eV. Fig. 5.3 conveys this idea very clearly. Each panel of Fig. 5.3 shows 20 trajectories of primary electrons impinging on a gold target and concurrently the secondary electron cascade for different energies (50, 500 and 5000 eV) for the two extreme energy dependencies of the IMFP
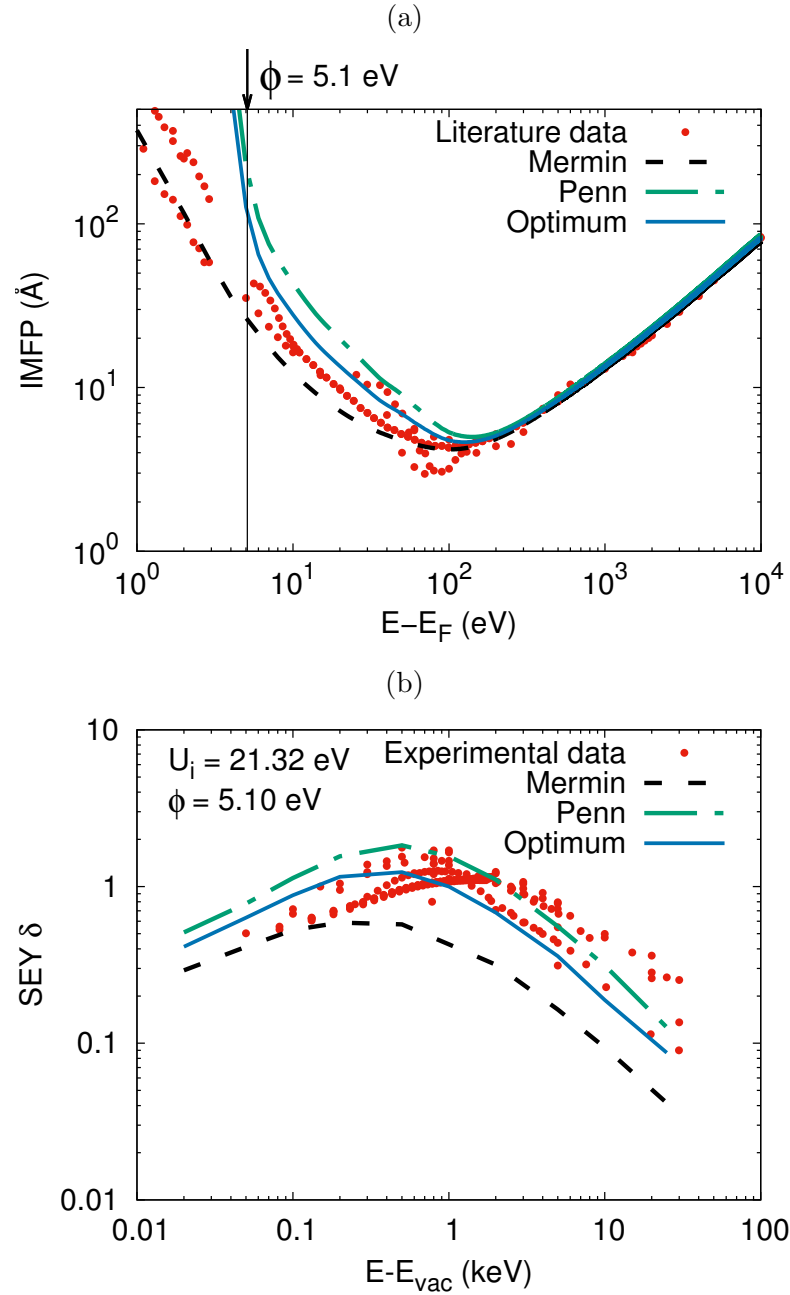
Figure 5.2: (a) Comparison of IMFPs obtained from the SEY analysis for Au (solid blue line) with IMFPs calculated using the Mermin dielectric function (dashed black line) and Penn algorithm (dashdotted green line). Red points represent the collection of literature data [134, 135, 136, 42, 18, 137, 47]. (b) Comparison of results of the MC calculation for SEYs using IMFP data from Fig. 5.2A (represented by solid lines) with experimental data [39, 104, 105] for normal electron incidence and emission into the entire hemisphere above the sample.

shown in Fig. 5.2A. The upper panel corresponds to the IMFP data calculated using Mermin dielectric function and the lower panel corresponds to the data calculated by Penn algorithm [133]. The penetration of incident electrons into the solid is seen to be deeper for higher incident energies due to the increasing of the IMFP (Fig. 5.2A). However, the main difference is the fact that at all incident energies (50, 500 and 5000 eV) the number of outgoing electrons is also very different for the two assumed low energy dependencies of the IMFP: for higher IMFP values a higher fraction of electrons within the cascade is indeed emitted from the surface. Therefore, even the high energy SEY data contain the information on the low energy IMFP.
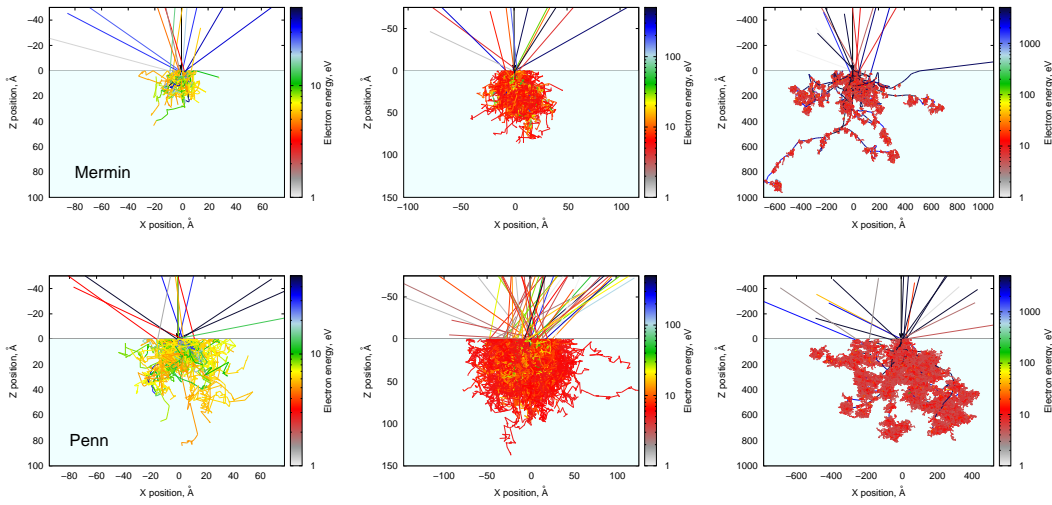

Figure 5.3: Electron trajectories with generation of secondaries corresponding to IMFP values based on the Mermin dielectric function (upper row) and Penn algorithm [133] (lower row) for Au. Note the differences in the scale for different incident energies.

In the present work, MC calculations were performed using different energy dependencies of the IMFP values below 100 eV ranging between the two extreme cases shown in Fig. 5.2A and determining those IMFP values which give the minimum least squares deviation of the simulated SEY curves with experimental data available in the literature. An MC code has been developed to simulate electron scattering processes in solids, including the production of the secondary electron cascade, based on a commonly employed algorithm [17, 40, 41]. This common model describes the secondary electron emission process implying three steps: primary electron transport in the solid, production of a secondary electron, transport and escape over the surface potential barrier of the produced secondary electron. In Section 3.2 this Monte Carlo algorithm is described in

more detail. Sections 2.3 and 2.4 describe the production of secondary electrons and the escape over the surface potential barrier, respectively. Subsection 5.1.1 contains the information on the input parameters needed for the MC simulation of the SEY. In section 5.1.2 results of comparisons of the simulated SEY data with available experimental literature data [39] are given as well as a comparison with individual extensive data sets produced by Bronstein [104] and Zadrazil [105]. First results of this work are published in Ref. [38]. The MC model has been implemented using the BRUCE software developed within the SIMDALEE2 (Sources, Interaction with Matter, Detection and Analysis of Low Energy Electrons) Marie-Curie Initial Training Network. The computational results presented have been achieved using the Vienna Scientific Cluster (VSC).

5.1.1 Input data for the MC simulation

In the present work, elastic and inelastic scattering processes are assumed to be independent [17]. Although this assumption is questionable in principle for low energy electrons, it is expected to not significantly affect the SEY. For the MC calculation data are needed for the elastic and inelastic mean free paths, the DECS, the DIIMFP, the inner potential U_i and the work function ϕ. The DECS data have been generated with the ELSEPA code [53]. Individual contributions from bulk and surface excitations were determined on the basis of the position- and direction dependent DIIMFP calculated employing the surface-excitation model introduced by Li [51] (Eq. 2.19). According to the Li formalism, an electron with certain energy has a probability for surface excitations depending on its position (inside the solid or in vacuum) and the direction of motion.

To calculate IMFP values using the Penn algorithm we used software provided by the authors of Ref. [133]. For this calculation, as well as for calculation of the DIIMFP, optical constants from Refs. [28, 27] were used employing linear response theory. Experimental data for U_i were used for all materials for which such values are available whereas for other materials U_i values were calculated according to an empirical formula proposed by Ross and Stobbs [50]. Besides values for the IMFP the inner potential U_i also is not accurately known or at least there is a big discrepancy in the literature. Fortunately, as explained further below, the value of U_i does not critically influence the determination of the IMFP. Values used for the work function ϕ were taken from Ref. [140].

It is important first to consider the differences between the two sets of used IMFP data. In both cases IMFP values were calculated following the well-known relationship within the first Born approximation Eq. 2.42. The energy loss function $\text{Im}\left[-1/\epsilon\left(\omega, q\right)\right]$ in the entire

(ω, q) plane was determined on the basis of the Mermin dielectric function $\epsilon_M(\omega, q)$ and the Penn algorithm. In the former approach, the energy loss function in the optical limit $\text{Im}\left[-1/\epsilon(\omega, q \approx 0)\right]$ [28, 27] was fitted in terms of Drude-Lindhard oscillators (Eq. 2.9). In the optical limit $q \approx 0$ the Mermin ELF coincides with the Drude-Lindhard ELF while it becomes broader for larger values of q due to the plasmon damping included into the Mermin model (Eq. 2.13) [54]. Since it is more convenient to perform the fitting of the optical ELF as a sum of Drude-Lindhard oscillators, the latter approach was used:

$$\text{Im}\left[\frac{-1}{\epsilon(\omega, q \approx 0)}\right]_{exp} = \sum_i A_i \frac{\omega \gamma_i \omega_i^2(q=0)}{\left(\omega^2 - \omega_i^2(q=0)\right)^2 + \omega^2 \gamma_i^2} \tag{5.1}$$

with A_i related to the density of electrons with the binding energy ω_i [54]. The oscillator parameters are chosen to reproduce the main features in the optical ELF and to satisfy the perfect screening sum rule. The fitting parameters for the 17 materials investigated in this work can be found in Ref. [38]. In the case of Si the parameters were taken from Ref. [141]. The ELF fitted at $q \approx 0$ was then extended to all values of q through the 'built-in' dispersion within the Mermin dielectric function, therefore no dispersion relation was needed.

The IMFP was then calculated using the Mermin ELF with the Drude-Lindhard oscillators obtained for $q = 0$ using Eq. 2.5. Fig. 5.4 shows the results of the fitting of the model ELF to experimental optical data [28, 27] for Cu, Ag, and Au in the optical limit.

The Penn algorithm is based on a modification of the statistical approximation [42] developed by Lindhard and can be employed within the Full Penn Algorithm (FPA) and the simple Penn algorithm or Single-Pole Approximation (SPA) [142, 143, 144]. The SPA approach implying a quadratic dispersion relation to extend the experimental optical ELF to all values of q is referred to as the simplified SPA or SSPA. The presented approach assumes the validity of the Born approximation, neglects the vertex correction, self-consistency, and exchange and correlation. It should also be mentioned that the present theory is expected to be reliable only for energies >100 eV. Although the authors of [133] recommend not to use this algorithm for energies below 100 eV, it was used in the present work just in order to have large sample values for the IMFP at low energies.

The main difference in the two presented approaches is the description of plasmon damping. The inclusion of plasmon damping into the model dielectric function and an accurate description of the ELF at low energy losses are known to have a significant influence on the low energy IMFP [145, 54]. Since a low energy electron can no longer
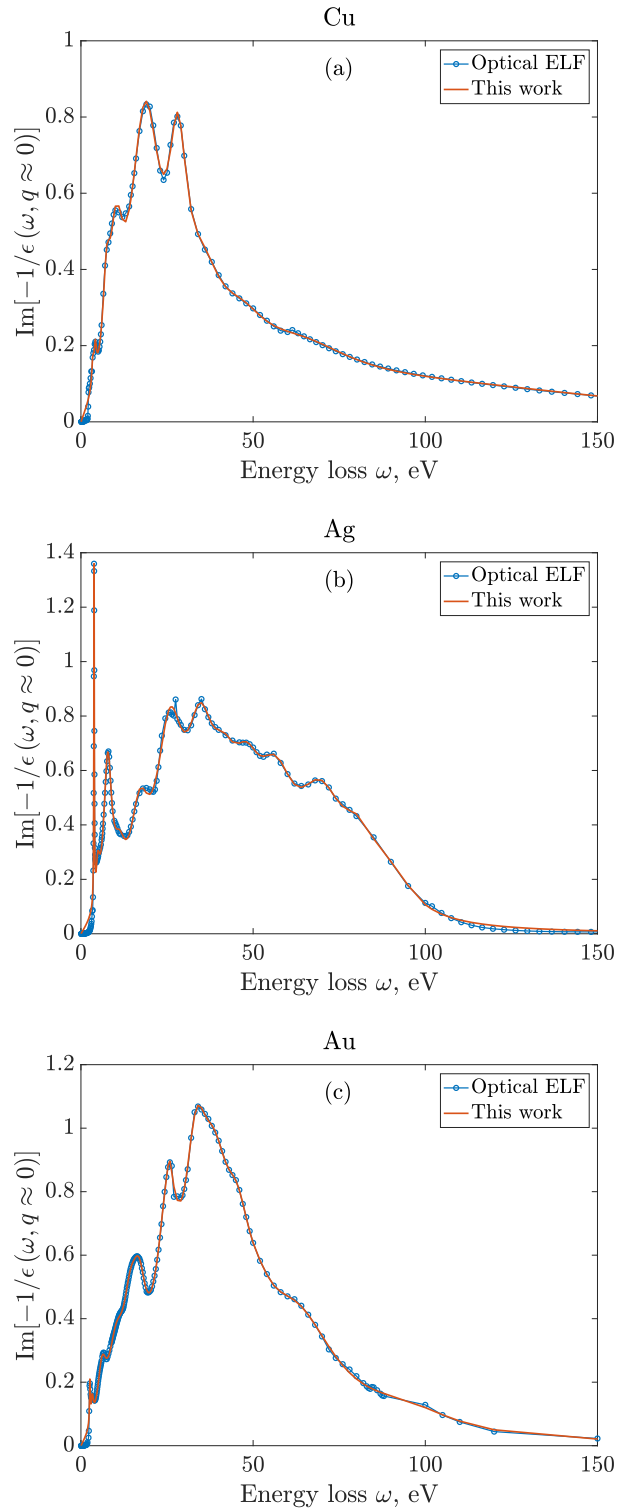
Figure 5.4: The Mermin energy loss function in the optical limit $q \approx 0$ of: (a) Cu; (b) Ag; (c) Au. The blue circles represent the experimental optical ELF taken from [28, 27].
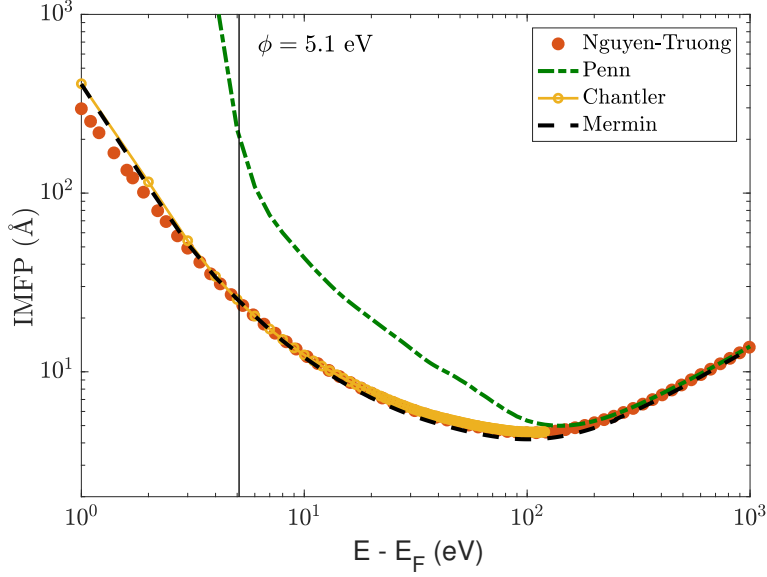
Figure 5.5: Comparison of the IMFP for Au calculated using: the Penn algorithm (dot-dashed green
curve), the Chantler algorithm [145] (yellow points), and the Mermin dielectric function (dashed black
curve). Red points represent results of the IMFP calculation from Ref.[146].

excite a plasmon, the IMFP increases with decreasing incident energy. However, for Penn
IMFP values this increase is observed to be faster than in the case of the Mermin IMFP.
In the Lindhard approach, which is used in the Penn algorithm, plasmon excitations are
supposed to be undamped below the critical value of the momentum transfer. Whereas
the Mermin approach implies an increase of plasmon broadening at any q, which makes
the ELF peaks broader not only away from $q = 0$ but also at small values of q, giving
a contribution to the DIIMFP intensity at low energy losses which is absent in Penn's
theory. Therefore, the increased intensity of the DIIMFP at low energies causes the
reduction of the IMFP values (Eq. 2.5).

There are other ways to determine the momentum-dependent ELF. Chantler and co-
authors used DFT concurrently with developments in many-pole dielectric theory [145].
Nguyen-Truong used the Mermin dielectric function to include damping in the ELF within
the Penn algorithm [146]. The advantage of this method is that it does not demand any
fitting parameters but only the knowledge of the optical dielectric function. Comparison
of the IMFP values for Au calculated in this work using the Mermin dielectric function
with the IMFP data obtained by Chantler and Nguyen-Truong is shown in Fig. 5.5. All
three data sets are seen to be similar demonstrating that the ELF accurately calculated
in the entire (ω, q) plane from the first principles yields the IMFP values in a good

agreement with those calculated in more specific ways.

5.1.2 Obtained results

Determination of IMFPs was performed for the following materials: Be, Al, Si, Ti, V, Fe,
Ni, Cu, Ge, Nb, Mo, Pd, Ag, Ta, W, Pt, Au by varying the energy dependence of the
IMFP at low energies (< 100 eV) between two extreme values according to the following
expression:

$$\lambda_\eta = \lambda_{Mermin} + 0.1 \cdot (\eta - 1) \left(\lambda_{Penn} - \lambda_{Mermin}\right) \tag{5.2}$$

where the number η ranges from 1 for Mermin IMFP to 11 for Penn IMFP. Then the SEY
calculated using each of the IMFP values from Eq. 5.2 were compared with different data
sets of SEY values from the literature. These data sets comprise: (a) collected literature
data [39, 104, 105]; (b) Bronstein data [104]; (c) Zadrazil data [105]. Those IMFP values
that give the best χ^2 fit of SEY values with experimental results are considered to be
the most reliable ones. The χ^2 optimisation finds those model parameters that minimize
the sum of quadratic residues between experimental and theoretical values.

Figs. 5.6–5.11 show results of the IMFP determination from the SEY analysis using the
presented algorithm for Ag, W, Al, Cu, Fe, and Pt. Each set of figures contains the upper
panel with comparison of the IMFP values obtained from the SEY analysis (solid blue
line) with the IMFP calculated using the Mermin dielectric function (dashed black line)
and Penn algorithm (dashdotted green line), and literature data. The three lower panels
show comparisons of SEY values corresponding to the three IMFP data sets mentioned
above with: (b) collected literature data [39, 104, 105]; (c) Bronstein data [104]; (d)
Zadrazil data [105]. The collected literature data [39, 104, 105] in Figs. 5.6–5.11 (c,d)
are shown as grey data points in order to highlight the chosen data set (red points) for
the SEY comparison and to demonstrate its position with respect to all experimental
data. The optimum values of η for 17 investigated materials are tabulated in Table 5.1.
There is a monotonic relation between η and the IMFP on one hand, and η and the SEY
on the other hand. Thus, lower values of η correspond to lower SEY values and lower
IMFP values at low energies. Note that the results in Table 5.1 are obtained in the case
when surface excitations were not considered in the MC model.

The SEY is typically characterized in terms of the maximum SE yield δ_m at the corre-
sponding energy E_m. Different values of δ_m and E_m are observed during the inspection
of different SEY data sets for such materials as Al and Cu (Figs. 5.8 and 5.9). The reason

Table 5.1: Physical quantities used in the SEY calculation and optimum IMFP numbers η.

	Z	ϕ (eV)	U_i (eV)	η^a	η^b	η^c
Be	4	4.98	7.8	4	1	-
Al	13	4.28	12.0	2	1	2
Si	14	4.85	12.1	1	1	1
Ti	22	4.33	16.62	2	2	5
V	23	4.3	20.13	4	-	3
Fe	26	4.5	20.93	10	7	8
Ni	28	5.15	20.14	5	5	5
Cu	29	4.65	18.5	6	4	3
Ge	32	5.0	15.6	3	5	6
Nb	41	4.3	22.1	3	2	2
Mo	42	4.6	22.66	2	2	2
Pd	46	5.12	22.37	5	5	-
Ag	47	4.26	17.11	1	1	1
Ta	73	4.25	27.58	3	2	2
W	74	4.55	23.4	1	1	1
Pt	78	5.65	30.14	9	9	8
Au	79	5.1	21.32	6	7	7

[a] Collected SEY data [39, 104, 105].
[b] Bronstein SEY data [104].
[c] Zadrazil SEY data [105].

for this spread in the experimental SEY data is likely due to the fact that these materials oxidize easily. Even a slight oxidation of a sample leads to a significant rise of the SEY. Since SEs are mainly emitted from the very surface region the SEY measurements, in particular at low energies, require strictly controlled vacuum conditions and, consequently, the purity of the sample surface. Bronstein and Fraiman [104] carried out particularly careful in-situ SEY measurements in the former Soviet Union. The authors used different methods to obtain clean surfaces such as annealing at high temperatures during the measurements (refractory metals), evaporation of the investigated material in vacuum, electron, and ion sputtering and had a good control of vacuum conditions during their measurements. The value of η in Table 5.1 for this data set is considerably lower than for other data sets and the energy dependence of the SEY is in a good agreement with the MC results. The fact that the IMFP increases with the increased thickness of the oxidized layer on top of the sample and that Bronstein SEY data correspond to the lowest IMFP values points to a good cleanliness of samples during the measurements,

which were documented in a very careful way. Therefore, we conclude that this set of SEY data is more reliable than the total collection of SEY data. Another extensive set of SEY measurements, selected for separate consideration, was carried out by Zadrazil and co-authors in Ultra High Vacuum (UHV) conditions with samples of a high purity (99.99% or better) as reported in [147, 105]. The SEY values from these two data sets are believed to be the most reliable since they are always lower than other measurements, which might indicate bad vacuum conditions or a contamination of the samples in the case of other data.

As can be seen from Table 5.1 for most materials the value of η is close to those which corresponds to the IMFP values calculated using the Mermin dielectric function ($\eta = 1$). Figs. 5.8, 5.6, and 5.7 show the situation when η is equal or close to 1 for Al, Ag, and W. The opposite situation when η value is close to 11, which corresponds to the Penn IMFP, is shown in Figs. 5.10, 5.11 for Fe and Pt. The case of an intermediate η value between 1 and 11 is demonstrated as an example for Cu in Fig. 5.9. Here, and also in the case of Mo (not shown), IMFP values predicted by XAFS measurements [46] are much lower than the Mermin IMFPs, which seems to be contradicting all available IMFP data including the results of this work. As seen from the upper panels of Figs. 5.8–5.7 there is always at least an order of magnitude difference between Mermin and Penn IMFP values at the vacuum level in all cases with the exception for Fe, which is very important for quantitative understanding of the secondary electron emission process. It is also seen that most of the IMFP data found in the literature tend to be close to the Mermin IMFPs, which is in a reasonable agreement with the results obtained in this work. Note that most of the literature data for the IMFP shown in the upper panels of Figs. 5.6–5.11 are theoretical data, since it is a quite challenging task to determine IMFP values at low incident energies using any experimental technique. However, the present work demonstrates an approach to do so using experimental SEY curves.
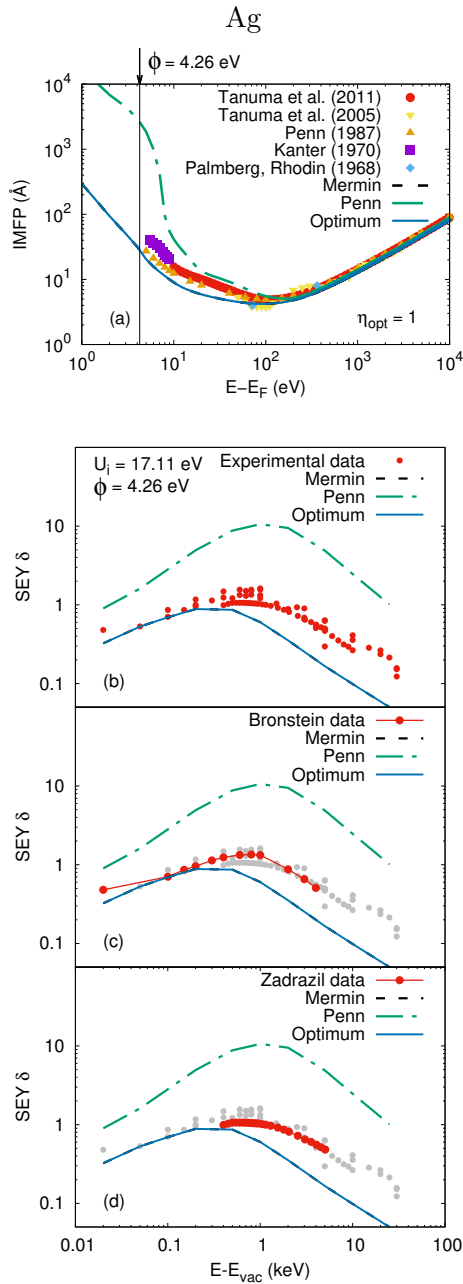
Figure 5.6: (a) Comparison of the IMFP for Ag obtained from the SEY analysis (solid blue line) with the IMFP calculated using the Mermin dielectric function (dashed black line) and Penn algorithm (dashdotted green line), and literature data [148, 135, 42, 18, 47]. Comparison of SEYs for Ag calculated using IMFP values shown in Fig. 5.8A by lines with: (b) all literature data [39, 105]; (c) Bronstein data [104]; (d) Zadrazil data [105].
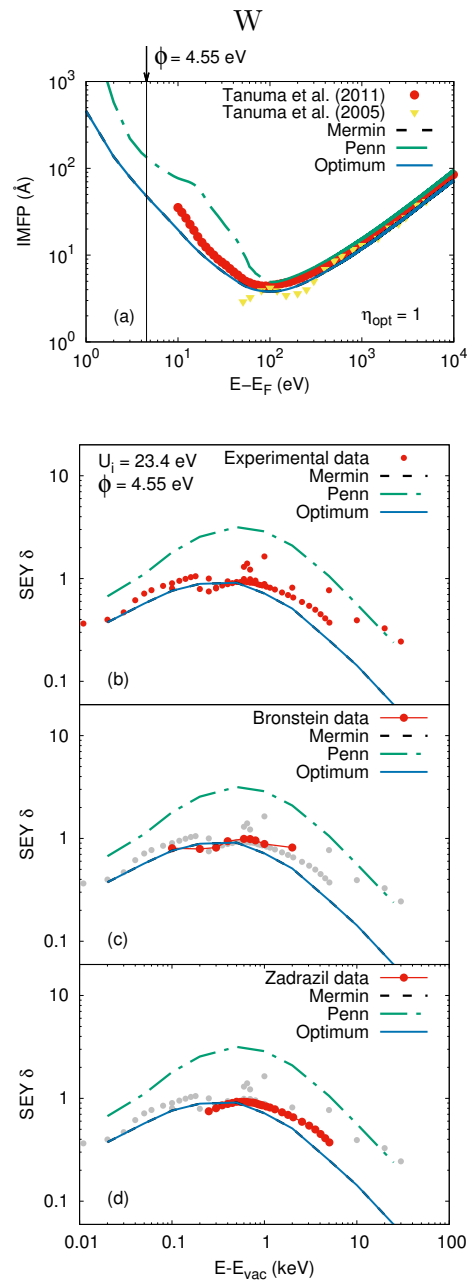
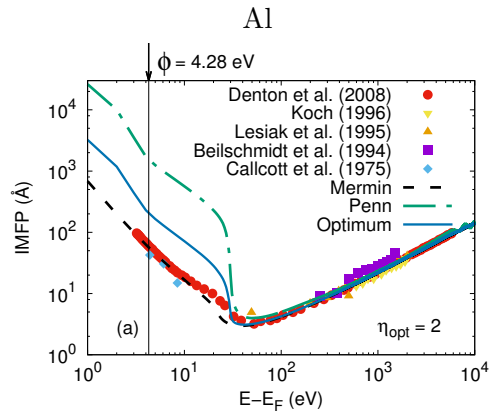**Figure 5.7:** The same as Fig. 5.6 but for W. Literature data from Fig. 5.7A are taken from [18, 47].
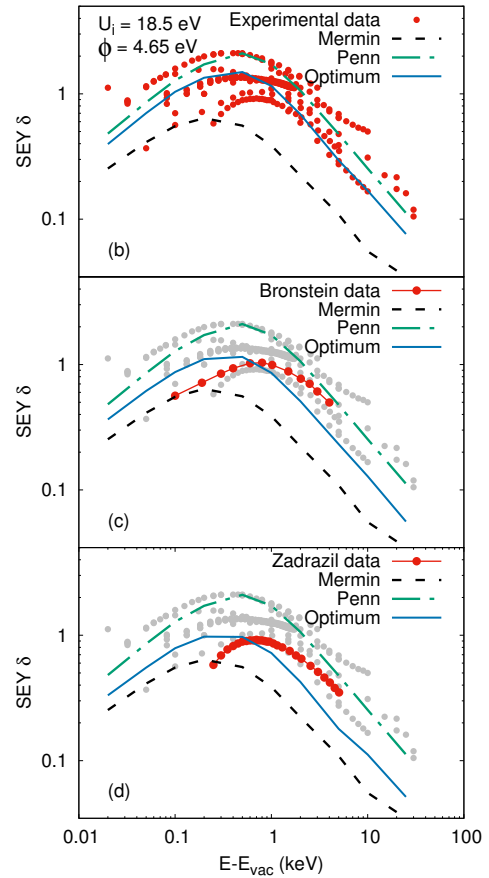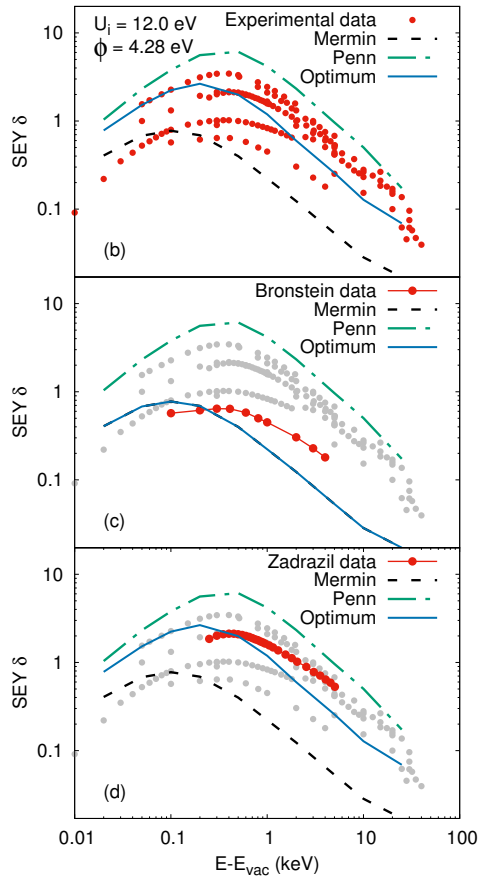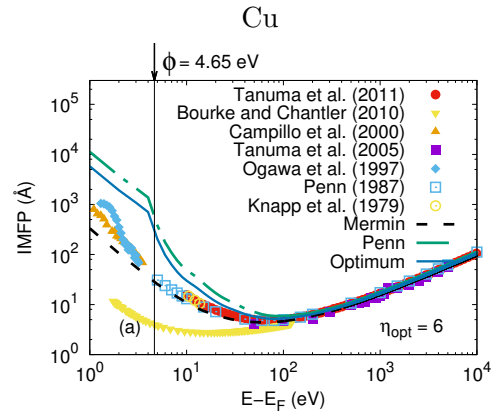
Figure 5.8: The same as Fig. 5.6 but for Al.
Literature data from Fig. 5.8A are taken from
[149, 150, 86, 151].

Figure 5.9: The same as Fig. 5.6 but for Cu.
Literature data from Fig. 5.9A are taken from
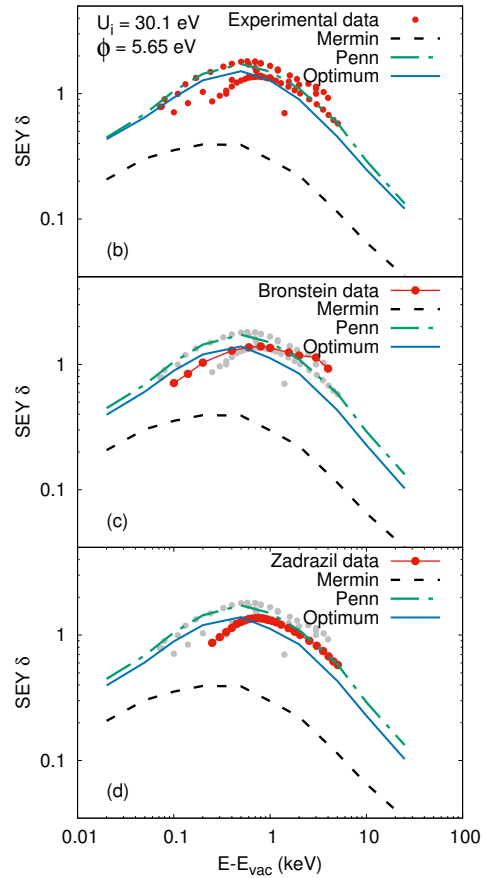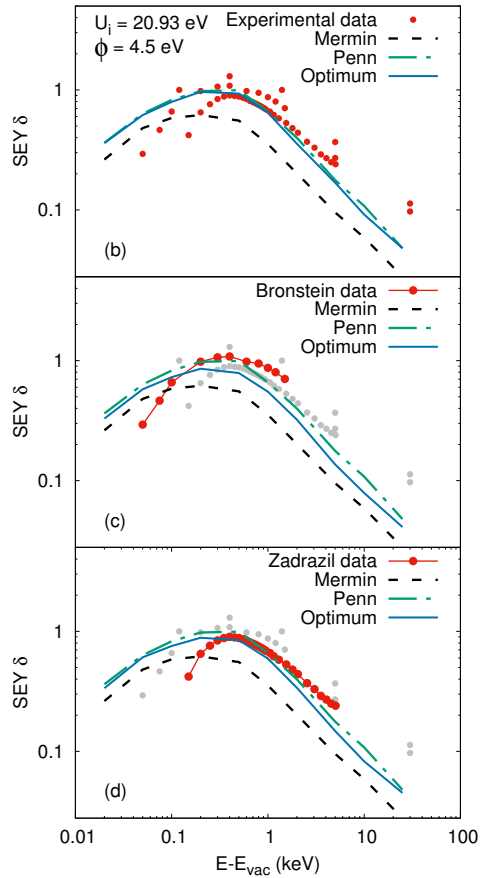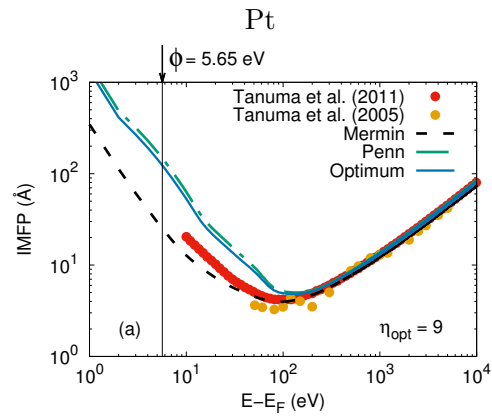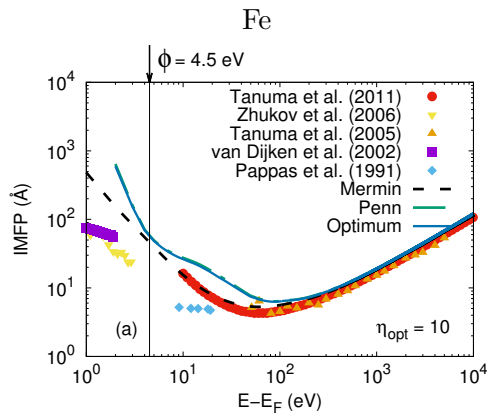[43, 42, 44, 18, 45, 46, 47].

Figure 5.10: The same as Fig. 5.6 but for Fe. Literature data from Fig. 5.10A are taken from [152, 153, 18, 137, 47, 154].

Figure 5.11: The same as Fig. 5.6 but for Pt. Literature data from Fig. 5.11A are taken from [18, 47].

Table 5.2: Optimum IMFP numbers η after including surface excitations into the MC model.

	Z	Without surface η^{a}	With surface η^{a}
Al	13	2	2
Ti	22	2	2
V	23	4	2
Fe	26	10	3
Ni	28	5	4
Cu	29	6	5
Mo	42	2	2
Pd	46	5	5
Ag	47	1	2
Ta	73	3	3
W	74	1	1
Pt	78	9	9
Au	79	6	6

[a] Collected SEY data [39, 104, 105].

In the case of transition metals, such as Fe and Pt, the obtained optimum η values are large compared with most of the investigated materials (see Table 5.1). In Ref. [147] the energy E_m corresponding to the maximum SE yield δ_m was shown to increase across each of the transition metal series. This dependence was explained by the concurrent increase of the IMFP with the number of electrons in the d band. However, since the authors did not use energy dependent IMFPs but only one IMFP value to describe the electron escape, the above statement does not explain the high η values. IMFP values close to the ones predicted by the Penn model are already large and do not limit the emission of the secondary electron cascade from the surface. It shows that the behavior of the SEY curves of the transition metals cannot be quantitatively explained by an appropriate choice of the low energy IMFP only. This means that further development of the SE emission model in the case of transition metals is needed with a detailed consideration of the electronic structure of these materials.

Accounting for surface excitations is also one of the possible improvements of the MC model which is known to have an important impact on the SE yield [70]. Table 5.2 demonstrates the comparison of the η^a values from Table 5.1 and those obtained when surface excitations were accounted for in the MC model for 13 materials for which surface
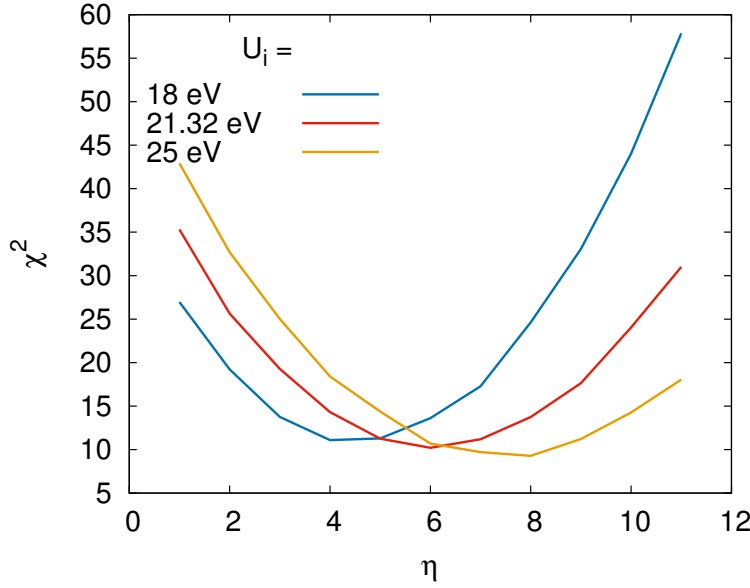
Figure 5.12: χ^2 test results for different U_i values in Au.

scattering data were available. In Table 5.2 η values are shown which were obtained from
the comparison of the calculated SEY data with collected literature data [39, 104, 105].
Accounting for surface excitations is seen to not considerably change the values of η
for most materials except the case of Fe. A seen from Table 5.2 after including surface
excitations into the MC model the value of η in the case of Fe decreased from 10 to 3.
Whereas in the case of Pt this value remained the same.

Finally, another important point concerning the presented approach needs to be discussed,
namely the fact that the SEY not only depends on the IMFP at low energies which is not
well known but also on the value of the inner potential U_i, which is also not well known.
For this reason, the influence of the value of U_i on the outcome of our study has been
investigated. Fig. 5.12 shows the results of the χ^2 fit for three different U_i values for Au.
It demonstrates that the error introduced by the uncertainty of the inner potential makes
an influence of plus or minus 1 in average on the resulting value of η. A similar result
was found for all materials investigated in the present study. Therefore the optimum
value of the energy dependent IMFP (characterized by the value of η as explained before)
does not depend critically on the inner potential.

5.1.3 Summary and conclusions

Determination of the IMFP at energies below 100 eV was performed by analyzing the
SEY in the incident energy range of 0.1 - 10 keV. A Monte Carlo model was employed to
simulate SEYs for two different energy dependencies of the IMFP at low energies (below
100 eV), calculated using the Mermin dielectric function [49] and the Penn algorithm
[42, 133]. Subsequent comparison of the simulated SEYs based on these IMFPs with the
experimental SEY data [39, 104, 105] give an estimate for the IMFP values at energies
below 100 eV. The optimum values of η (ranging from 1 for IMFP values based on the
Mermin dielectric function to 11 for IMFP values based on the Penn algorithm) for 17
investigated materials are presented in Table 5.1. The general conclusion that can be
drawn on the basis of Table 5.1 is that for most materials, with the exception of the
transition metals, the more realistic energy dependence of the IMFP at low energies is
given by the Mermin model. These optimum IMFP values were shown to be not critically
affected by the choice of the inner potential U_i.

The presented MC model has some deficiencies in that it does not consider the band
structure effect, a quantum-mechanical representation of the potential barrier, etc. The
main purpose of this work is to demonstrate the possibility of the presented approach to
analyse high energy SEYs and to reverse engineer the IMFP at low energies. Further
development of the MC model taking into account all possible considerations will allow
obtaining more reliable IMFPs at low energies.

5.2 Experimental determination of low energy IMFP using elastic peak electron spectroscopy (EPES)

Elastic peak electron spectroscopy is a widely used technique for the experimental deter-
mination of the IMFP [18]. IMFP values can be conveniently derived from measurements
of the elastic reflection coefficient since it is easily assessed experimentally and depends
sensitively on the IMFP [17]. The dependence of the elastic reflection coefficient η_{el} on
the IMFP can be explained by writing the following expression:

$$R_0 \equiv \eta_{el}\left(\lambda_{in}\right) = \int_0^\infty e^{-\frac{s}{\lambda_{in}}} K\left(s\right) ds \qquad (5.3)$$

where R_0 is the zero-order (elastic) partial intensity in the quasi-elastic limit, $K(s)$ is the path length distribution for the considered reflection geometry. Finding the value of λ_{in} that minimizes the residue between the experimentally measured and theoretically calculated (Eq. 5.3) reflection coefficient allows retrieving the IMFP. In the present work such a technique was employed to determine the values of the IMFP for Au at energies below 200 eV.

5.2.1 Experimental

In the laboratory of the Technical University in Vienna measurements of the elastic reflection coefficient were performed in the SE2ELCS (Secondary Electron- Electron Energy Loss Coincidence Spectroscopy) spectrometer on a polycrystalline gold sample. In SE2ELCS (illustrated in Fig. 5.13) the sample is irradiated with a continuous beam of electrons. Back reflected electrons can be detected with a Hemispherical Analyser (HMA), which is positioned in specular reflection with the electron gun at $60°$ with respect to the surface normal, and with a Time-Of-Flight (TOF) analyser, which has an enhanced energy resolution at low energies and a wide accepted solid angle of the order of $\pm 10°$ [3]. During measurements the TOF analyser records event flight times, while the energy observed by the HMA is scanned from the incident energy down to several eV. The energy resolution at the HMA is 2.5% of the pass energy, whereas in the TOF analyser the energy resolution depends on the kinetic energy of the detected electrons.

Before the EPES measurements, the surface of a gold sample was rinsed with ethyl alcohol followed by cleaning in an ultrasonic bath for 10 minutes to remove surface contamination. Then the cleanliness of the surface of the gold sample was verified by means of XPS. The measurements of elastic peaks were carried out consistently using the two analysers (TOF and HMA) in the incident energy range of 10 – 1600 eV.

5.2.2 Determination of IMFPs from elastic peak intensies

Elastic peaks in the energy spectra measured with the TOF and HMA analysers were fitted with a gaussian for each incident energy with subsequent calculation of the areas under these peaks. An example of the fitting is shown in Fig. 5.14 for the spectra measured at 50 eV incident energy with the TOF (Fig. 5.14A) and the HMA (Fig. 5.14B) analysers. Values of the reflection coefficient were determined by dividing the areas under
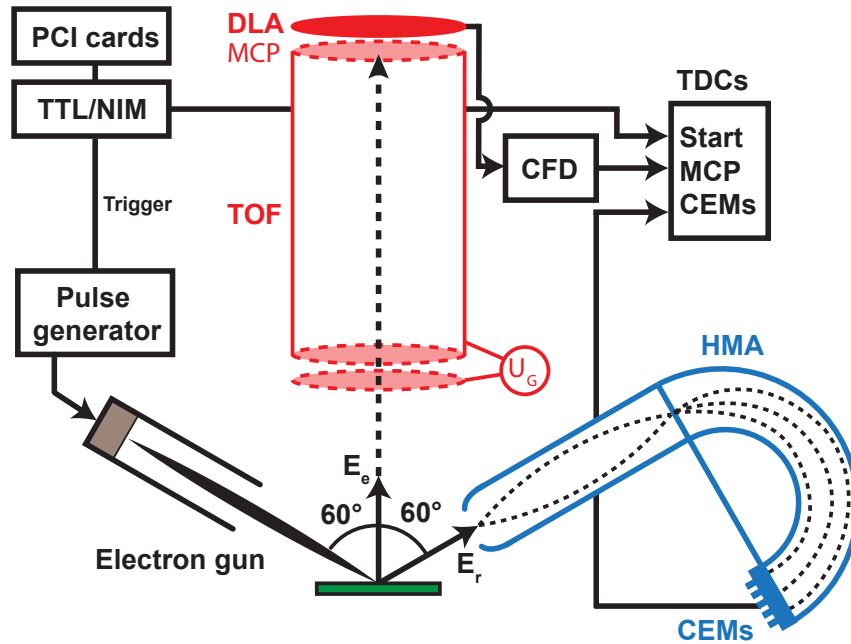
Figure 5.13: Schematic view of the SE2ELCS spectrometer. The angle of the incidence of the electron beam encloses 60° with respect to the surface normal of the sample. The HMA, equipped with 5 channeltrons, is in specular reflection and detects the reflected electrons, while the TOF-analyser is placed along the surface normal and the emitted electrons are detected with a detector consisting of Multi Channel Plates (MCP) and a Delay Line Anode (DLA).

elastic peaks on the primary current measured at each incident energy before the EPES measurements.

Theoretical calculations of the elastic reflection coefficient were performed using the Monte Carlo simulation. Using the path length distribution calculated in the quasi-elastic regime by means of the MC simulation the reflection coefficient η_{el} was then obtained using Eq. 5.3. In Eq. 5.3 the calculation of the PLD $K(s)$ and the zero-order partial intensity R_0 require the knowledge of the differential elastic scattering cross sections for the scattering angles and energies used in the EPES experiments. Fig. 5.15 shows the energy dependence of the differential elastic scattering cross section for Au. Black dashed lines shown in Fig. 5.15 refer to the scattering angles corresponding to those in the experimental arrangement with the TOF ($\psi = 120°$) and the HMA ($\psi = 60°$) analysers. A cut along these lines allows predicting the energy dependence of the reflection coefficient for the experimental geometries with the scattering angles $\psi = 120°$ and $\psi = 60°$. In Fig. 5.16 the resulting energy dependence of the experimental reflection
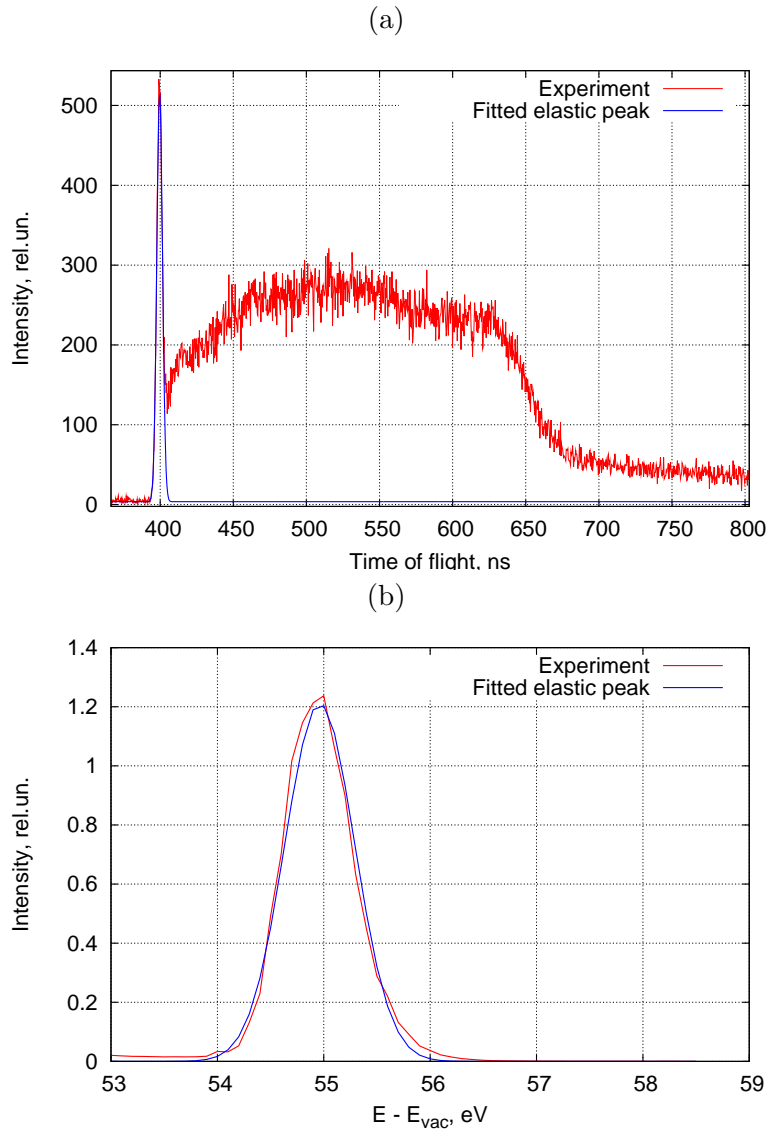
(a)

(b)

Figure 5.14: Fitting of elastic peaks in: (a) the TOF spectrum, and (b) the REELS spectrum for $E_0 = 50$ eV.

coefficient acquired by means of the TOF (Fig. 5.16A) and the HMA (Fig. 5.16B) is compared with theoretical calculations using the MC simulation. The experimental data were normalized to the MC results at the incident energy of 800 eV where the IMFP is assumed to be accurately known. Indeed, a similarity between the energy dependence of the reflection coefficient and the DECS as a function of the incident energy for both scattering angles can be clearly observed from Fig. 5.16.
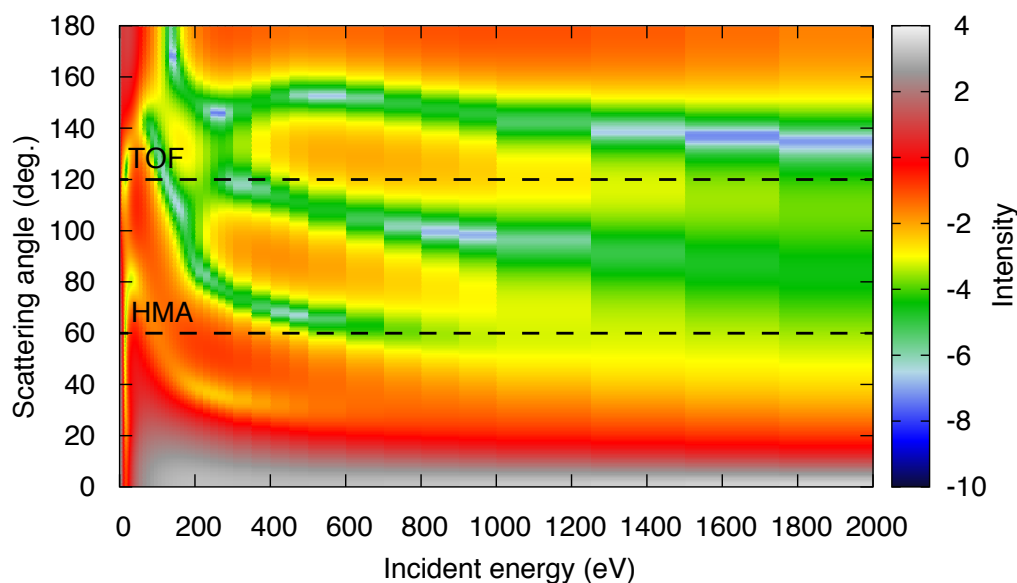
Figure 5.15: The energy dependence of the differential elastic scattering cross section of Au as a function of the polar scattering angle. Note that the intensity is shown in the logarithmic scale.

In order to derive the IMFP values from the measured elastic reflection coefficient the latter quantity was calculated by means of the MC simulation for each incident energy by varying IMFP values in a certain range. This range was determined by taking the reference value from those calculated using the Penn algorithm and multiplying it by 2 to get the upper limit and dividing by 2 to get the lower limit. The obtained dependence of the reflection coefficient on the IMFP was fitted with a polynomial. The experimental IMFP value is then determined from the approximating polynomial by using the experimental value for the reflection coefficient as shown in Fig. 5.17. Fig. 5.18 shows the comparison of the resulting IMFP values (blue data points) derived from the measurements of the elastic reflection coefficient using the TOF (Fig. 5.18A) and the HMA (Fig. 5.18B) with theoretical calculations using the Mermin dielectric function [49] and the Penn algorithm [42]. In the case of the TOF analyser (Fig. 5.18A) a good agreement between the experimental and theoretical IMFP values is observed for energies above 500 eV whereas at lower energies the experimental results do not follow an expected behavior demonstrating too low values of the IMFP. In the case of the HMA analyser an opposite takes place where the experimental IMFP values are seen to be closer to the Penn data in the energy range of 30-500 eV. At energies above 500 eV the experimental IMFP values are seen to decrease with the incident energy increasing whereas at energies below 30 eV these data are observed to be much higher than those for the Penn algorithm.
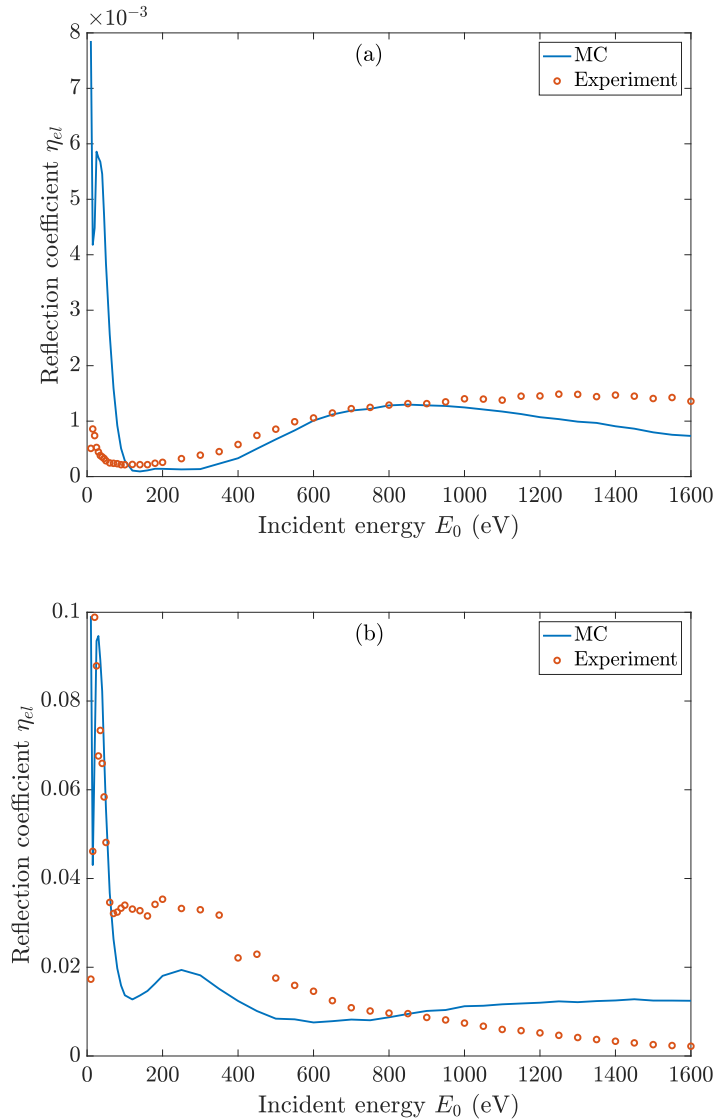
Figure 5.16: Red data points: the energy dependence of the reflection coefficient for Au measured using: (a) the TOF analyser, and (b) the HMA analyser. Blue solid curves: results of the Monte Carlo simulation. The experimental data were normalized to the MC results at the incident energy of 800 eV.

A general conclusion that can be drawn is that the IMFP values derived from the measurements of elastic peak intensities do not seem to be reasonable at low incident energies (below 200 eV). There are several reasons to explain this. First of all, it is very challenging to perform an experiment at such low energies. The presence of electric or magnetic fields, charging can have tremendous influence for the trajectories and energies of the electrons and therefore have to be accounted for, which is complicated and not

always possible due to hardware limitations. Furthermore, the extracted values depend on the reliability of the theoretical model, describing the elastic backscattering from the solid. Since the theoretical approach used in this work has been established for the processes at medium energies (above 500 eV), it might be inaccurate or not work at all at low energies, thus retrieving meaningless results of the IMFP.
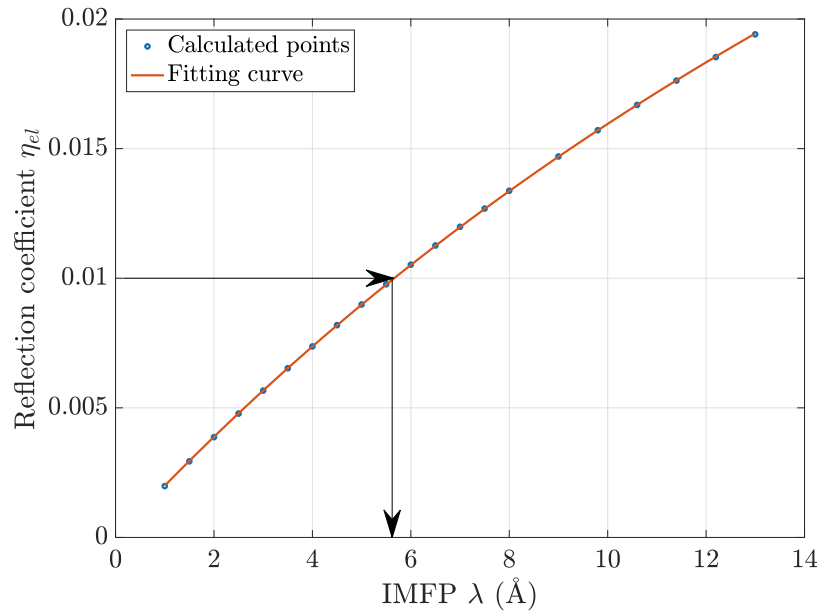

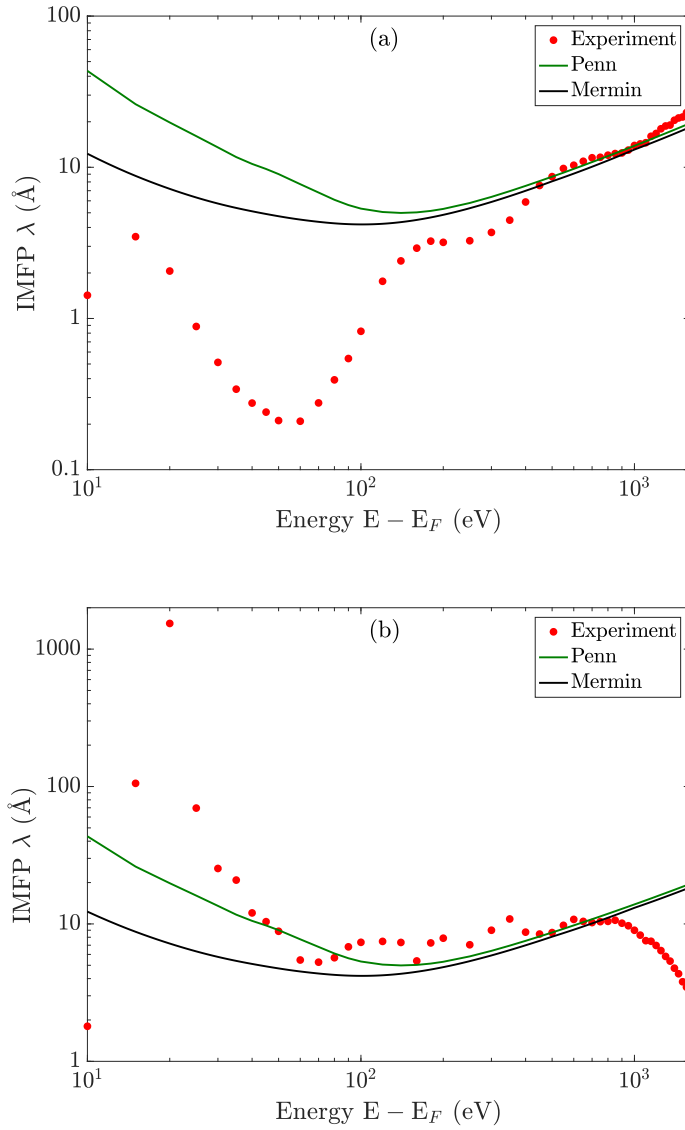**Figure 5.17:** Fitting curve for the IMFP extraction.

Figure 5.18: IMFP values derived from the EPES measurements using: (a) the TOF analyser, and (b) the HMA analyser. Comparison of obtained results on the IMFP with theoretical data calculated on the basis of the Mermin dielectric function (green solid line) and the Penn SSPA algorithm (red solid line).

Chapter 6

Summary and conclusions

In this work, the transport of electrons with medium $(200 - 5000 \text{ eV})$ and low (below 100 eV) kinetic energies in solids was considered. Two approaches were employed to find a solution to the transport equation namely the Invariant Imbedding Method (IIM) and the Monte Carlo (MC) simulation. The IIM was employed to consider the electron transport at medium energies and was demonstrated to be a powerful technique for the interpretation of electron energy loss spectra and the study of material properties from these data. This approach enables to solve the boundary problem for the transport equation by means of the Numerical Solution (NS) of the system of nonlinear equations for the transmission, reflection, and photoelectron flux density functions known as the Ambartsumian–Chandrasekhar (AC) equations. This NS is based on the discrete ordinate formalism and relies on a transformation of the AC equations to the algebraic Ricatti and Lyapunov equations, which are solved by using the backward differential formula. Besides, this numerical technique is very efficient with respect to performance. For instance, it takes about a second to reproduce a Reflection Electron Energy Loss (REELS) spectrum with the initial electron energy of several keV on an Intel Xeon CPU E5-1620 3.60 GHz. This fact allows the use of the IIM for the retrieval of the Differential Inverse Inelastic Mean Free Path (DIIMFP) from a REELS spectrum. Such a procedure described in Section 4.1 represents a fitting algorithm consisting of the finding the oscillator parameters for the Energy Loss Function (ELF) which minimize the residue between calculated REELS spectra and experimental data.

In the present work, the fitting algorithm using the IIM was employed to investigate the evolution of X-ray Photoelectron spectra (XPS) at the thermal reduction of Graphene

Oxide (GO) [155, 122]. It has been shown that photoelectron spectra can provide a great amount of information about processes that take place during the annealing of GO samples. As long as a sufficient amount of oxygen is present in the samples (at annealing temperatures below 150°C), the π plasmon cannot be identified in the spectrum. The heat treatment of the GO samples at the annealing temperature range of $170 - 200$°C causes the percolation transition, at which the conductivity of the material increases by 5 orders of magnitude accompanied by increasing intensity of the π plasmon, therefore, demonstrating a correlation between the latter quantities.

Another application of the IIM approach concerns the possibility of detection and interpretation of hydrogen isotopes in solids. An extended survey was conducted on beryllium samples implanted with different doses of deuterium ions employing two analytical techniques comprising Elastic Peak Electron Spectroscopy (EPES) and REELS [25]. The possibility of quantitative analysis of hydrogen isotopes by means of the combination of these techniques was demonstrated.

The MC approach was employed to consider the electron transport at low energies in order to investigate the phenomenon of Secondary Electron Emission (SEE) from solid surfaces. For this purpose, an MC code has been developed on the basis of the so-called three-step model implying the following steps: (1) transport of a primary electron in a solid, (2) generation of a secondary electron, and (3) transport and escape over the surface potential barrier of the produced SE. This MC model was employed to determine the electron Inelastic Mean Free Path (IMFP) at low incident energies (below 100 eV) by means of analysis of Secondary Electrons Yields (SEY) measured in the incident energy range of 0.1 - 10 keV. This was performed by varying the energy dependence of the IMFP at low energies (below 100 eV) during the MC simulation of the SEY between two extremes, calculated on the basis of the Mermin dielectric function and the Penn algorithm within the simplified single-pole approximation (SSPA) [38]. Those IMFP values that gave the best χ^2 fit of the simulated SEY values with experimental results were considered as the most reliable. The MC model was employed with and without accounting for surface excitations. The described algorithm was employed for the investigation of Al, Ti, V, Fe, Ni, Cu, Mo, Pd, Ag, Ta, W, Pt, and Au. For most materials the optimum IMFP values are found to be close to those calculated using the Mermin dielectric function. The inclusion of surface excitations did not make a great impact on the obtained results except in the case of Fe, where the optimum IMFP values became closer to the Mermin IMFPs instead of the Penn IMFPs as it was without considering surface effects. The possibility to get an estimation on the IMFP at energies

below 100 eV from analysis of SEYs measured at high energies provides an important guideline and allows to reverse engineer the IMFP at low energies. So far this approach was used only to investigate metals whereas the investigation of insulator materials is also of high importance.

An attempt to measure the IMFP at low energies (below 100 eV) by means of the EPES technique was also performed and is presented in Section 5.2. Unfortunately, this study did not yield meaningful results on the IMFP values at low energies demonstrating, on one hand, the difficulty of carrying out measurements at energies below 100 eV and on the other hand calling into question the reliability of the employed theoretical model at low energies.

Bibliography

[1] Terry L Alford, Leonard C Feldman, and James W Mayer. *Fundamentals of Nanoscale Film Analysis*. Springer US, Boston, MA, 2007.

[2] M.A. Gusarova, V.I. Kaminsky, L.V. Kravchuk, S.V. Kutsaev, M.V. Lalayan, N.P. Sobenin, and S.G. Tarasov. Multipacting simulation in accelerating RF structures. *Nucl. Instruments Methods Phys. Res. Sect. A Accel. Spectrometers, Detect. Assoc. Equip.*, 599(1):100–105, feb 2009.

[3] A. Bellissimo, G. M. Pierantozzi, A. Ruocco, G. Stefani, O. Yu. Ridzel, V. Astasauskas, W. S. M. Werner, and M. Taborelli. Secondary electron generation mechanisms in carbon allotropes at low impact electron energies. *J. Electron Spectros. Relat. Phenomena*, 2019. (in press).

[4] R. Cimino, I. R. Collins, M. A. Furman, M. Pivi, F. Ruggiero, G. Rumolo, and F. Zimmermann. Can Low-Energy Electrons Affect High-Energy Physics Accelerators? *Phys. Rev. Lett.*, 93(1):014801, jun 2004.

[5] Kazuhito Ohmi. Beam-Photoelectron Interactions in Positron Storage Rings. *Phys. Rev. Lett.*, 75(8):1526–1529, aug 1995.

[6] B Henrist, N Hilleret, M Jimenez, C Scheuerlein, M Taborelli, and G Vorlaufer. Secondary electron emission data for the simulation of electron cloud. In *Mini Work. Electron-Cloud Simulations Prot. Positron Beams*, Geneva, Switherland, 2002.

[7] Henry B. Garrett and Albert C. Whittlesey. *Guide to Mitigating Spacecraft Charging Effects*. John Wiley & Sons, Inc., Hoboken, NJ, USA, may 2012.

[8] G. Fubiani, H. P. L. de Esch, A. Simonin, and R. S. Hemsworth. Modeling of secondary emission processes in the negative ion based electrostatic accelerator of the International Thermonuclear Experimental Reactor. *Phys. Rev. Spec. Top. - Accel. Beams*, 11(1):014202, jan 2008.

[9] H Seiler. Secondary electron emission in the scanning electron microscope. *J. Appl. Phys.*, 54(11):R1–R18, nov 1983.

[10] J.J. Scholtz, D. Dijkkamp, and R.W.A. Schmitz. Secondary electron emission properties. *Philips J. Res.*, 50:375–389, 1996.

[11] A Shih, J Yater, C Hor, and R Abrams. Secondary electron emission studies. *Appl. Surf. Sci.*, 111:251–258, 1997.

[12] Joseph Ladislas Wiza. Microchannel plate detectors. *Nucl. Instruments Methods*, 162(1-3):587–601, jun 1979.

[13] D. F. Kyser, H. Niedrig, D. E. Newbury, and R. Shimizu. Electron beam interactions with solids for Microscopy, Microanalysis & Microlithography. In *1st Pfefferkorn Conf.* Scanning Electron Microscopy, Inc., 1982.

[14] Léon Sanche. Low-energy electron therapy. *Nat. Mater.*, 14(9):861–863, sep 2015.

[15] A. Bellissimo. *Multiparameter Analysis of Genesis and Evolution of Secondary Electrons produced in the Low Energy Regime.* PhD thesis, University of Roma Tre, 2019.

[16] B Lesiak, A Jablonski, Z Prussak, and P Mrozek. Experimental determination of the inelastic mean free path of electrons in solids. *Surf. Sci. Lett.*, 223(1-2):A583–A584, 1989.

[17] Wolfgang S. M. Werner. Electron transport in solids for quantitative surface analysis. *Surf. Interface Anal.*, 31(3):141–176, mar 2001.

[18] S. Tanuma, T. Shiratori, T. Kimura, K. Goto, S. Ichimura, and C. J. Powell. Experimental determination of electron inelastic mean free paths in 13 elemental solids in the 50 to 5000 eV energy range by elastic-peak electron spectroscopy. *Surf. Interface Anal.*, 37(11):833–845, nov 2005.

[19] A. Jablonski and J. Zemek. Angle-resolved elastic-peak electron spectroscopy: Solid-state effects. *Surf. Sci.*, 600(19):4464–4474, oct 2006.

[20] A Sulyok, G Gergely, M Menyhard, J Toth, D Varga, L Kover, Z Berenyi, B Lesiak, and A Kosinski. Recoil effect in carbon structures and polymers. *Vacuum*, 63(1-2):371–376, jul 2001.

[21] M Vos. Detection of hydrogen by electron Rutherford backscattering. *Ultramicroscopy*, 92(3-4):143–149, 2002.

[22] G.T. Orosz, G. Gergely, M. Menyhard, J. Tóth, D. Varga, B. Lesiak, and A. Jablonski. Hydrogen and surface excitation in electron spectra of polyethylene. *Surf. Sci.*, 566-568:544–548, sep 2004.

[23] I. A. Kostanovskiy, V. P. Afanas'ev, D. Naujoks, and M. Mayer. Hydrocarbon isotope detection by elastic peak electron spectroscopy. *J. Electron Spectros. Relat. Phenomena*, 202:22–25, 2015.

[24] V P Afanas'ev, A S Gryazev, D S Efremenko, P S Kaplya, and O Y Ridzel. Determination of atomic hydrogen in hydrocarbons by means of the reflected electron energy loss spectroscopy and the X-ray photoelectron spectroscopy. *J. Phys. Conf. Ser.*, 748:012005, 2016.

[25] V P Afanas'ev, A S Gryazev, P S Kaplya, M Köppen, O Yu Ridzel, N Yu Subbotin, and P Hansen. Investigation of Deuterium Implantation into Beryllium Sample by Electron Energy Loss Spectroscopy. *J. Phys. Conf. Ser.*, 891:012303, 2017.

[26] Wolfgang S. M. Werner, Kathrin Glantschnig, and Claudia Ambrosch-Draxl. Optical Constants and Inelastic Electron-Scattering Data for 17 Elemental Metals. *J. Phys. Chem. Ref. Data*, 38(4):1013–1092, dec 2009.

[27] B.L. Henke, E.M. Gullikson, and J.C. Davis. X-Ray Interactions: Photoabsorption, Scattering, Transmission, and Reflection at E = 50-30,000 eV, Z = 1-92. *At. Data Nucl. Data Tables*, 54(2):181–342, jul 1993.

[28] ED Palik. *Handbook of Optical Constants of Solids.* Academic Press, 1998.

[29] H. Kalbe, V. Astasauskas, P. Kuksa, A. Bellissimo, and W. S. M. Werner. Optical constants and electron inelastic mean free paths of organic insulators extracted from reflection electron energy loss spectra. *Surf. Interface Anal.*, 2019. (in press).

[30] R. H. Ritchie. Plasma Losses by Fast Electrons in Thin Films. *Phys. Rev.*, 106(5):874–881, 1957.

[31] V A Ambartsumian. A new method for computing light scattering in turbid media. *Izv. Acad. Sci. USSR, Ser. Geogr. Geophys. Sci.*, 3:97–103, 1942.

[32] S Chandrasekhar. *Radiative Transfer.* New York Dover, 1960.

[33] V.P. Afanas'ev. *Interaction of electron and light ion fluxes with layered heterogeneous targets.* PhD thesis, Moscow state university, 2003. (in Russian).

[34] Viktor P Afanas'ev, Olga Y. Golovina, Alexander S Gryazev, Dmitry S Efremenko, and Pavel S Kaplya. Photoelectron spectra of finite-thickness layers. *J. Vac. Sci. Technol. B, Nanotechnol. Microelectron. Mater. Process. Meas. Phenom.*, 33(3):03D101, may 2015.

[35] Victor P. Afanas'ev, Dmitry S. Efremenko, and Pavel S. Kaplya. Analytical and numerical methods for computing electron partial intensities in the case of multilayer systems. *J. Electron Spectros. Relat. Phenomena*, 210:16–29, 2016.

[36] P. S. Kaplya. *Creation of precise methods of the analysis of solids on the basis of the interpretation of electron spectroscopy data by means of the invariant imbedding method.* PhD thesis, Moscow state university, 2016. (in Russian).

[37] Viktor P. Afanas'ev, Alexander S Gryazev, Dmitry S Efremenko, and Pavel S Kaplya. Differential inverse inelastic mean free path and differential surface excitation

probability retrieval from electron energy loss spectra. *Vacuum*, 136:146–155, feb 2017.

[38] Olga Yu. Ridzel, Vytautas Astašauskas, and Wolfgang S.M. Werner. Low energy (1–100 eV) electron inelastic mean free path (IMFP) values determined from analysis of secondary electron yields (SEY) in the incident energy range of 0.1–10 keV. *J. Electron Spectros. Relat. Phenomena*, feb 2019. (in press).

[39] Yinghong Lin and David C. Joy. A new examination of secondary electron yield data. *Surf. Interface Anal.*, 37(11):895–900, 2005.

[40] Z. J. Ding, X. D. Tang, and R. Shimizu. Monte Carlo study of secondary electron emission. *J. Appl. Phys.*, 89(1):718–726, jan 2001.

[41] R Shimizu and Ding Ze-Jun. Monte Carlo modelling of electron-solid interactions. *Reports Prog. Phys.*, 55(4):487–531, apr 1992.

[42] David R. Penn. Electron mean-free-path calculations using a model dielectric function. *Phys. Rev. B*, 35(2):482–486, jan 1987.

[43] J. A. Knapp, F. J. Himpsel, and D. E. Eastman. Experimental energy band dispersions and lifetimes for valence and conduction bands of copper using angle-resolved photoemission. *Phys. Rev. B*, 19(10):4952–4964, may 1979.

[44] S. Ogawa, H. Nagano, and H. Petek. Hot-electron dynamics at Cu(100), Cu(110), and Cu(111) surfaces: Comparison of experiment with Fermi-liquid theory. *Phys. Rev. B*, 55(16):10869–10877, apr 1997.

[45] I. Campillo, A. Rubio, J. M. Pitarke, A. Goldmann, and P. M. Echenique. Hole Dynamics in Noble Metals. *Phys. Rev. Lett.*, 85(15):3241–3244, oct 2000.

[46] J. D. Bourke and C. T. Chantler. Measurements of Electron Inelastic Mean Free Paths in Materials. *Phys. Rev. Lett.*, 104(20):206601, may 2010.

[47] S. Tanuma, C. J. Powell, and D. R. Penn. Calculations of electron inelastic mean free paths. IX. Data for 41 elemental solids over the 50 eV to 30 keV range. *Surf. Interface Anal.*, 43(3):689–713, mar 2011.

[48] Hieu T Nguyen-Truong. Electron inelastic mean free path at energies below 100 eV. *J. Phys. Condens. Matter*, 29(21):215501, jun 2017.

[49] N. D. Mermin. Lindhard dielectric function in the relaxation-time approximation. *Phys. Rev. B*, 1(5):2362–2363, 1970.

[50] Rafal E Dunin-Borkowski, Martha R McCartney, and D J Smith. Electron Holography of Nanostructured Materials. In *Encycl. Nanosci. Nanotechnol.*, pages 41–99. American Scientific Publishers, 2004.

[51] Y. C. Li, Y. H. Tu, C. M. Kwei, and C. J. Tung. Influence of the direction of motion on the inelastic interaction between electrons and solid surfaces. *Surf. Sci.*, 589(1-3):67–76, 2005.

[52] Wolfgang S M Werner, Mihály Novák, Francesc Salvat–Pujol, Josef Zemek, and Petr Jiricek. Electron Supersurface Scattering On Polycrystalline Au. *Phys. Rev. Lett.*, 110(8):086110, feb 2013.

[53] Francesc Salvat, Aleksander Jablonski, and Cedric J. Powell. ELSEPA - Dirac partial-wave calculation of elastic scattering of electrons and positrons by atoms, positive ions and molecules. *Comput. Phys. Commun.*, 165(2):157–190, jan 2005.

[54] Maarten Vos and Pedro L. Grande. How the choice of model dielectric function affects the calculated observables. *Nucl. Instruments Methods Phys. Res. Sect. B Beam Interact. with Mater. Atoms*, 407:97–109, 2017.

[55] Enrico Fermi. The ionization loss of energy in gases and in condensed materials. *Phys. Rev.*, 57(6):485–493, mar 1940.

[56] H Nikjoo, S Uehara, and D Emfietzoglou. *Interaction of Radiation with Matter.* CRC press, 2012.

[57] J Lindhard. On the properites of a gas of charged particles. *Kgl. Danske Vidensk. Selsk. Mat-fys. Medd.*, 28:8, 1954.

[58] Maarten Vos and Pedro L. Grande. Extracting the dielectric function from high-energy REELS measurements. *Surf. Interface Anal.*, 49(9):809–821, 2017.

[59] J. P. Ganachaud and M. Cailler. A Monte-Carlo calculation of the secondary electron emission of normal metals. I. The model. *Surf. Sci.*, 83(2):498–518, 1979.

[60] A Akkerman, A Breskin, R Chechik, and A Gibrekhterman. *Ionization of Solids by Heavy Particles.* Plenum press, New York, 1993.

[61] C. J. Powell and J. B. Swan. Origin of the characteristic electron energy losses in aluminum. *Phys. Rev.*, 115(4):869–875, oct 1959.

[62] C. J. Powell and J. B. Swan. Origin of the Characteristic Electron Energy Losses in Magnesium. *Phys. Rev.*, 116(1):81–83, oct 1959.

[63] Wolfgang S.M. Werner, Werner Smekal, Christian Tomastik, and Herbert Störi. Surface excitation probability of medium energy electrons in metals and semiconductors. *Surf. Sci.*, 486(3):L461–L466, jul 2001.

[64] C. J. Tung, Y. F. Chen, C. M. Kwei, and T. L. Chou. Differential cross sections for plasmon excitations and reflected electron-energy-loss spectra. *Phys. Rev. B*, 49(23):16684–16693, 1994.

[65] Wolfgang S.M. Werner. Simple algorithm for quantitative analysis of reflection electron energy loss spectra (REELS). *Surf. Sci.*, 604(3-4):290–299, feb 2010.

[66] Wolfgang S.M. Werner. Surface and bulk plasmon coupling observed in reflection electron energy loss spectra. *Surf. Sci.*, 526(3):L159–L164, mar 2003.

[67] David Bote, Francesc Salvat, Aleksander Jablonski, and Cedric J. Powell. Cross sections for ionization of K, L and M shells of atoms by impact of electrons and positrons with energies up to 1 GeV: Analytical formulas. *At. Data Nucl. Data Tables*, 95(6):871–909, nov 2009.

[68] Michał Gryziński. Two-Particle Collisions. II. Coulomb Collisions in the Laboratory System of Coordinates. *Phys. Rev.*, 138(2A):A322–A335, apr 1965.

[69] E. Casnati, A. Tartari, and C. Baraldi. An empirical approach to K-shell ionisation cross section by electrons. *J. Phys. B At. Mol. Phys.*, 15(1):155–167, 1982.

[70] Wolfgang S. M. Werner, Francesc Salvat-Pujol, Alessandra Bellissimo, Rahila Khalid, Werner Smekal, Mihály Novák, Alessandro Ruocco, and Giovanni Stefani. Secondary-electron emission induced by in vacuo surface excitations near a polycrystalline Al surface. *Phys. Rev. B*, 88(20):201407, nov 2013.

[71] Vytautas Astašauskas, Alessandra Bellissimo, Pavel Kuksa, Christian Tomastik, Henryk Kalbe, and Wolfgang S.M. Werner. Optical and Electronic properties of amorphous Silicon Dioxide by single and double electron spectroscopy. *J. Electron Spectros. Relat. Phenomena*, feb 2019. (in press).

[72] Francesc Salvat-Pujol. *Secondary-electron emission from solids: Coincidence experiments and dielectric formalism*. PhD thesis, Technischen Universität Wien, 2012.

[73] C. Bouchard and J.D. Carette. The surface potential barrier in secondary emission from semiconductors. *Surf. Sci.*, 100(1):251–268, 1980.

[74] Claude Cohen-Tannoudji, Bernard Diu, and Frank Laloë. *Quantum Mechanics Vol. I*. New York : John Wiley & Sons, 1977.

[75] P. A. Doyle and P. S. Turner. Relativistic Hartree–Fock X-ray and electron scattering factors. *Acta Crystallogr. Sect. A*, 24(3):390–397, may 1968.

[76] D. Rez, P. Rez, and I. Grant. Dirac–Fock calculations of X-ray scattering factors and contributions to the mean inner potential for electron scattering. *Acta Crystallogr. Sect. A Found. Crystallogr.*, 50(4):481–497, jul 1994.

[77] F. M. Ross and W. M. Stobbs. A study of the initial stages of the oxidation of silicon using the Fresnel method. *Philos. Mag. A*, 63(1):1–36, jan 1991.

[78] Jing Li, M. R. McCartney, R. E. Dunin-Borkowski, and David J. Smith. Determination of mean inner potential of germanium using off-axis electron holography. *Acta Crystallogr. Sect. A Found. Crystallogr.*, 55(4):652–658, jul 1999.

[79] J.P. Ganachaud and A. Mokrani. Theoretical study of the secondary electron emission of insulating targets. *Surf. Sci.*, 334:329–341, 1995.

[80] Steven H. Simon. *The Oxford solid state basics (1st ed.)*. Oxford: Oxford University Press, 2013.

[81] E Schreiber. Attenuation and escape depths of low-energy electron emission. *J. Electron Spectros. Relat. Phenomena*, 119:35–47, 2001.

[82] J. Llacer and E. L. Garwin. Electron-phonon interaction in alkali halides. I. The transport of secondary electrons with energies between 0.25 and 7.5 eV. *J. Appl. Phys.*, 40(7):2766–2775, 1969.

[83] Luc Van Kessel. *Electron Blur in Photoresist for EUV Lithography*. PhD thesis, Radboud University Nijmegen, 2017.

[84] O D Chwolson. Grundzuge einer mathematischen Theorie der inneren Diffusion des Lichtes. *Bull. Acad. Imp. Sci.*, 33:221–256, 1889.

[85] Wolfgang S. M. Werner, Igor S. Tilinin, and Markus Hayek. Angular distribution of electrons reflected elastically from noncrystalline solid surfaces. *Phys. Rev. B*, 50(7):4819–4833, aug 1994.

[86] Wolfgang S. M. Werner and Markus Hayek. Influence of the elastic scattering cross-section on angle-resolved reflection electron energy loss spectra of polycrystalline Al, Ni, Pt and Au. *Surf. Interface Anal.*, 22(1-12):79–83, jul 1994.

[87] Wolfgang S M Werner. Partial intensity analysis (PIA) for quantitative electron spectroscopy. *Surf. Interface Anal.*, 23(11):737–752, 1995.

[88] Wolfgang S. M. Werner. Slowing down of medium-energy electrons in solids. *Phys. Rev. B*, 55(22):14925–14934, jun 1997.

[89] S. Borodyansky. Methods of electron spectra processing based on solving the transport equation of electron motion in a solid. *Surf. Interface Anal.*, 19(1-12):181–186, jun 1992.

[90] V.P. Afanas'ev, O.Yu. Golovina, and P.S. Kaplya. Quantitative Interpretation of Energy X-ray Photoemission Spectra. *J. Surf. Investig. X-ray, Synchrotron Neutron Tech.*, 9(2):331–335, 2015.

[91] K. N. Liou. Chapter 7 Applications of radiative transfer to remote sensing of the atmosphere. In *Int. Geophys.*, volume 84, pages 234–292. 1980.

[92] Roger F. Dashen. Theory of Electron Backscattering. *Phys. Rev.*, 134(4A):A1025–A1032, may 1964.

[93] Richard Bellman, Robert Kalaba, and G. Milton Wing. Invariant imbedding and mathematical physics. I. Particle processes. *J. Math. Phys.*, 1(4):280–308, 1960.

[94] Victor P Afanas'ev, Dmitry S Efremenko, and Alexander V Lubenchenko. On the application of the invariant embedding method and the radiative transfer equation

codes for surface state analysis. In *Light Scatt. Rev. 8 Radiat. Transf. Light Scatt.*, pages 363–423. Springer Berlin Heidelberg, Berlin, Heidelberg, 2013.

[95] M.B. Trzhaskovskaya, V.I. Nefedov, and V.G. Yarzhemsky. Photoelectron angular distribution parameters for elements Z=1 to Z=54 in the photoelectron energy range 100–5000 eV. *At. Data Nucl. Data Tables*, 77(1):97–159, jan 2001.

[96] V Hernández, J J Ibáñez, J Peinado, and E Arias. A GMRES-based BDF method for solving differential Riccati equations. *Appl. Math. Comput.*, 196(2):613–626, 2008.

[97] A Doicu and T Trautmann. Discrete-ordinate method with matrix exponential for a pseudo-spherical atmosphere: Scalar case. *J. Quant. Spectrosc. Radiat. Transf.*, 110(1-2):146–158, 2009.

[98] P. S. Kaplya and O. Yu. Ridzel. Electron and Photoelectron Spectroscopy Calculator ESCal github.com/Pazus/ESCal.

[99] Dmitry Efremenko, Adrian Doicu, Diego Loyola, and Thomas Trautmann. Acceleration techniques for the discrete ordinate method. *J. Quant. Spectrosc. Radiat. Transf.*, 114:73–81, 2013.

[100] Dmitry S. Efremenko, Diego G. Loyola, Adrian Doicu, and Robert J.D. Spurr. Multicore-CPU and GPU-accelerated radiative transfer models based on the discrete ordinate method. *Comput. Phys. Commun.*, 185(12):3079–3089, dec 2014.

[101] V.P. Afanas'ev, P.S. Kaplya, A.V. Lubenchenko, and O.I. Lubenchenko. Modern methods of transfer theory used for solution of signal identification problems of XPS. *Vacuum*, 105:96–101, jul 2014.

[102] F. Salvat-Pujol and W. S.M. Werner. Surface excitations in electron spectroscopy. Part I: Dielectric formalism and Monte Carlo algorithm. *Surf. Interface Anal.*, 45(5):873–894, 2013.

[103] W. A. Coleman. Mathematical Verification of a Certain Monte Carlo Sampling Technique and Applications of the Technique to Radiation Transport Problems. *Nucl. Sci. Eng.*, 32(1):76–81, apr 1968.

[104] I M Bronstein and B S Fraiman. *Secondary electron emission*. Nauka: Moskva, 1969. (in Russian).

[105] M. M. EL Gomati, C. G. H. Walker, A. M. D. Assa'd, and M. Zadražil. Theory Experiment Comparison of the Electron Backscattering Factor from Solids at Low Electron Energy (250–5,000 eV). *Scanning*, 30(1):2–15, jan 2008.

[106] Sylvan Rubin. Surface analysis by charged particle spectroscopy, 1959.

[107] T E Everhart. Simple Theory Concerning the Reflection of Electrons from Solids. *J. Appl. Phys.*, 31(8):1483–1490, aug 1960.

[108] Songfeng Pei and Hui-Ming Cheng. The reduction of graphene oxide. *Carbon N. Y.*, 50(9):3210–3228, aug 2012.

[109] G.I. Titelman, V. Gelman, S. Bron, R.L. Khalfin, Y. Cohen, and H. Bianco-Peled. Characteristics and microstructure of aqueous colloidal dispersions of graphite oxide. *Carbon N. Y.*, 43(3):641–649, 2005.

[110] Kuibo Yin, Haitao Li, Yidong Xia, Hengchang Bi, Jun Sun, Zhiguo Liu, and Litao Sun. Thermodynamic and Kinetic Analysis of Lowtemperature Thermal Reduction of Graphene Oxide. *Nano-Micro Lett.*, 3(1):51–55, mar 2011.

[111] Hae-Kyung Jeong, Yun Pyo Lee, Mei Hua Jin, Eun Sung Kim, Jung Jun Bae, and Young Hee Lee. Thermal stability of graphite oxide. *Chem. Phys. Lett.*, 470(4-6):255–258, mar 2009.

[112] Seung Hun. Thermal Reduction of Graphene Oxide. In *Phys. Appl. Graphene - Exp.*, chapter 5. InTech, 2011.

[113] Abhijit Ganguly, Surbhi Sharma, Pagona Papakonstantinou, and Jeremy Hamilton. Probing the thermal deoxygenation of graphene oxide using high-resolution in situ X-ray-based spectroscopies. *J. Phys. Chem. C*, 115(34):17009–17019, 2011.

[114] Nguyen Dien Kha Tu, Jaeyoo Choi, Chong Rae Park, and Heesuk Kim. Remarkable Conversion Between n- and p-Type Reduced Graphene Oxide on Varying the Thermal Annealing Temperature. *Chem. Mater.*, 27(21):7362–7369, nov 2015.

[115] Y.M. Shulga, V.M. Martynenko, V.E. Muradyan, S.A. Baskakov, V.A. Smirnov, and G.L. Gutsev. Gaseous products of thermo- and photo-reduction of graphite oxide. *Chem. Phys. Lett.*, 498(4-6):287–291, oct 2010.

[116] Young Joon Oh, Jung Joon Yoo, Yong Il Kim, Jae Kook Yoon, Ha Na Yoon, Jong-Huy Kim, and Seung Bin Park. Oxygen functional groups and electrochemical capacitive behavior of incompletely reduced graphene oxides as a thin-film electrode of supercapacitor. *Electrochim. Acta*, 116:118–128, jan 2014.

[117] William S Hummers and Richard E Offeman. Preparation of Graphitic Oxide. *J. Am. Chem. Soc.*, 80(6):1339, mar 1958.

[118] L. Stobinski, B. Lesiak, A. Malolepszy, M. Mazurkiewicz, B. Mierzwa, J. Zemek, P. Jiricek, and I. Bieloshapka. Graphene oxide and reduced graphene oxide studied by the XRD, TEM and electron spectroscopy methods. *J. Electron Spectros. Relat. Phenomena*, 195:145–154, aug 2014.

[119] Xingfa Gao, Joonkyung Jang, and Shigeru Nagase. Hydrazine and Thermal Reduction of Graphene Oxide: Reaction Mechanisms, Product Structures, and Reaction Design. *J. Phys. Chem. C*, 114(2):832–842, jan 2010.

141

[120] S Doniach and M Sunjic. Many-electron singularity in X-ray photoemission and X-ray line spectra from metals. *J. Phys. C Solid State Phys.*, 3(2):285–291, feb 1970.

[121] Adila Rani, Seungwoong Nam, Kyoung-Ah Oh, and Min Park. Electrical Conductivity of Chemically Reduced Graphene Powders under Compression. *Carbon Lett.*, 11(2):90–95, jun 2010.

[122] V P Afanas'ev, G S Bocharov, A S Gryazev, A V Eletskii, P S Kaplya, and O Y Ridzel. Reduced graphene oxide studied by X-ray photoelectron spectroscopy: evolution of plasmon mode. *J. Phys. Conf. Ser.*, 1121:012001, nov 2018.

[123] G. S. Bocharov and A. V. Eletskii. Percolation Transition Under Thermal Reduction of Graphene Oxide. *J. Struct. Chem.*, 59(4):806–814, jul 2018.

[124] D. M. Duffy. Modeling plasma facing materials for fusion power. *Mater. Today*, 12(11):38–44, 2009.

[125] M.I. Rusu, C. Pardanaud, Y. Ferro, G. Giacometti, C. Martin, Y. Addab, P. Roubin, M. Minissale, L. Ferri, F. Virot, M. Barrachin, C.P. Lungu, C. Porosnicu, P. Dinca, M. Lungu, M. Köppen, P. Hansen, and Ch Linsmeier. Preparing the future post-mortem analysis of beryllium-based JET and ITER samples by multi-wavelengths Raman spectroscopy on implanted Be, and co-deposited Be. *Nucl. Fusion*, 57(7):076035, jul 2017.

[126] D. Borodin, S. Brezinsek, J. Miettunen, M. Stamp, A. Kirschner, C. Björkas, M. Groth, S. Marsen, C. Silva, S. W. Lisgo, D. Matveev, M. Airila, and V. Philipps. Determination of Be sputtering yields from spectroscopic observations at the JET ITER-like wall based on three-dimensional ERO modelling. *Phys. Scr.*, T159, 2014.

[127] C. Pardanaud, M. I. Rusu, C. Martin, G. Giacometti, P. Roubin, Y. Ferro, A. Allouche, M. Oberkofler, M. Köppen, T. Dittmar, and Ch Linsmeier. Hydrogen retention in beryllium: concentration effect and nanocrystalline growth. *J. Phys. Condens. Matter*, 27(47):475401, dec 2015.

[128] Siegfried Hofmann. *Auger- and X-Ray Photoelectron Spectroscopy in Materials Science*, volume 49 of *Springer Series in Surface Sciences*. Springer Berlin Heidelberg, Berlin, Heidelberg, 2013.

[129] M. Vos and M. R. Went. Elastic electron scattering at high momentum transfer: A possible new analytic tool. *J. Electron Spectros. Relat. Phenomena*, 155(1-3):35–39, 2007.

[130] M.R. Went and M. Vos. Rutherford backscattering using electrons as projectiles: Underlying principles and possible applications. *Nucl. Instruments Methods Phys. Res. Sect. B Beam Interact. with Mater. Atoms*, 266(6):998–1011, 2008.

[131] Nenad Stojilovic. Why Can't We See Hydrogen in X-ray Photoelectron Spectroscopy? *J. Chem. Educ.*, 89(10):1331–1332, sep 2012.

[132] V. P. Afanas'ev, M. V. Afanas'ev, A. V. Lubenchenko, A. A. Batrakov, D. S. Efremenko, and M. Vos. Influence of multiple elastic scattering on the shape of the elastically scattered electron peak. *J. Electron Spectros. Relat. Phenomena*, 177(1):35–41, feb 2010.

[133] S. Tanuma, C. J. Powell, and D. R. Penn. Calculations of electorn inelastic mean free paths. II. Data for 27 elements over the 50-2000 eV range. *Surf. Interface Anal.*, 17(13):911–926, dec 1991.

[134] S.M. Sze, J.L. Moll, and T. Sugano. Range-energy relation of hot electrons in gold. *Solid. State. Electron.*, 7(7):509–523, jul 1964.

[135] H. Kanter. Slow-electron mean free paths in aluminum, silver, and gold. *Phys. Rev. B*, 1(2):522–536, jan 1970.

[136] I. Lindau, P. Pianetta, K.Y. Yu, and W.E. Spicer. Determination of the escape depth of photoemitted electrons in gold in the energy range 25–75 eV by use of synchrotron radiation. *J. Electron Spectros. Relat. Phenomena*, 8(5):487–491, jan 1976.

[137] V. P. Zhukov, E. V. Chulkov, and P. M. Echenique. Lifetimes and inelastic mean free path of low-energy excited electrons in Fe, Ni, Pt, and Au: Ab initio GW+T calculations. *Phys. Rev. B - Condens. Matter Mater. Phys.*, 73(12):125105, mar 2006.

[138] Cristian D. Denton, Isabel Abril, Rafael Garcia-Molina, Juan C. Moreno-Marín, and Santiago Heredia-Avalos. Influence of the description of the target energy-loss function on the energy loss of swift projectiles. *Surf. Interface Anal.*, 40(11):1481–1487, nov 2008.

[139] Jay D. Bourke and Christopher T. Chantler. Electron energy loss spectra and overestimation of inelastic mean free paths in many-pole models. *J. Phys. Chem. A*, 116(12):3202–3205, 2012.

[140] David R. Lide, editor. *CRC Handbook of Chemistry and Physics*. CRC press, 88 edition, 2008.

[141] M. Vos, P. L. Grande, and G. Marmitt. The influence of shallow core levels on the shape of REELS spectra. *J. Electron Spectros. Relat. Phenomena*, 229:42–46, dec 2018.

[142] Hieu T. Nguyen-Truong. Energy-loss function including damping and prediction of plasmon lifetime. *J. Electron Spectros. Relat. Phenomena*, 193(October):79–85, mar 2014.

[143] Dimitris Emfietzoglou, Ioanna Kyriakou, Rafael Garcia-Molina, and Isabel Abril. Inelastic mean free path of low-energy electrons in condensed media: beyond the standard models. *Surf. Interface Anal.*, 49(1):4–10, 2017.

[144] H. Shinotsuka, B. Da, S. Tanuma, H. Yoshikawa, C. J. Powell, and D. R. Penn. Calculations of electron inelastic mean free paths. XI. Data for liquid water for energies from 50 eV to 30 keV. *Surf. Interface Anal.*, 49(4):238–252, apr 2017.

[145] C. T. Chantler and J. D. Bourke. Electron Inelastic Mean Free Path Theory and Density Functional Theory Resolving Discrepancies for Low-Energy Electrons in Copper. *J. Phys. Chem. A*, 118(5):909–914, 2014.

[146] Hieu T. Nguyen-Truong. Penn algorithm including damping for calculating the electron inelastic mean free path. *J. Phys. Chem. C*, 119(14):7883–7887, 2015.

[147] C. G.H. Walker, M. M. El-Gomati, A. M.D. Assa'd, and M. Zadražil. The secondary electron emission yield for 24 solid elements excited by primary electrons in the range 250-5000 ev: A theory/experiment comparison. *Scanning*, 30(5):365–380, 2008.

[148] P. W. Palmberg and T. N. Rhodin. Auger Electron Spectroscopy of fcc Metal Surfaces. *J. Appl. Phys.*, 39(5):2425–2432, apr 1968.

[149] A Koch. *Automatische Oberflachenmodellierung starrer dreidimensionaler Objekte aus stereoskopischen Rundum-Ansichten*. PhD thesis, Eberhard-Karls-Universität, 1996.

[150] T. A. Callcott and E. T. Arakawa. Volume and surface photoemission processes from plasmon resonance fields. *Phys. Rev. B*, 11(8):2750–2758, apr 1975.

[151] B Lesiak, A Jablonski, L Zommer, A Kosinski, G Gergely, A Konkol, A Sulyok, Cs S Daroczi, and P Nagy. 6th European Conference on Applications of Surface and Interface Analysis: ECASIA95. Montreaux, 1995.

[152] D. Pappas, K.-P. Kämper, B. Miller, H. Hopster, D. Fowler, C. Brundle, A. Luntz, and Z.-X. Shen. Spin-dependent electron attenuation by transmission through thin ferromagnetic films. *Phys. Rev. Lett.*, 66(4):504–507, jan 1991.

[153] Sebastiaan van Dijken, Xin Jiang, and Stuart S. P. Parkin. Spin-dependent hot electron transport in Ni81Fe19 and Co84Fe16 films on GaAs(001). *Phys. Rev. B*, 66(9):094417, sep 2002.

[154] R. Zdyb, T. O. Menteş, A. Locatelli, M. A. Niño, and E. Bauer. Inelastic mean free path from reflectivity of slow electrons. *Phys. Rev. B*, 87(7):075436, feb 2013.

[155] Viktor P. Afanas'ev, Grigorii S. Bocharov, Alexander V. Eletskii, Olga Yu. Ridzel, Pavel S. Kaplya, and Martin Köppen. Evolution of photoelectron spectra at thermal reduction of graphene oxide. *J. Vac. Sci. Technol. B, Nanotechnol. Microelectron. Mater. Process. Meas. Phenom.*, 35(4):041804, jul 2017.